Atom-light interaction in nano-structured alkali-metal vapour cells

THOMAS FRANK CUTLER

Atom-light interaction in nano-structured alkali-metal vapour cells

CUTLER, THOMAS,FRANK

Atom-light interaction in nano-structured alkali-metal vapour cells

Thomas Frank Cutler

A thesis presented for the degree of
Doctor of Philosophy

Quantum Light and Matter
Department of Physics
Durham University
United Kingdom
September 2022

Atom-light interaction in nano-structured alkali-metal vapour cells

Thomas Frank Cutler

Abstract

We present an experimental and theoretical study into the behaviour of thermal atoms confined to bespoke micro- and nano-structured vapour cells. We detail advancements to our cell platform, and use our cells to study a number of physical effects at novel lengthscales. We study light-induced atomic desorption (LIAD) for localised liberation of wall-adsorbed atoms into the vapour phase, and demonstrate density increases of up to 5× in a micron-scale region. We also find that non-resonant laser light can create high density condensed regions of rubidium on the cell walls. We demonstrate two-colour excitation and fluorescence spectroscopy in a nano-cell, and use this scheme to measure the density distribution of atoms confined to a $1 \times 1\,\mu m$ channel. We measure an exponential decay with distance into the channel, with a lengthscale of $4.0(11)\,\mu m$. Finally, we study the response of confined vapours to resonant nanosecond laser pulses. We measure the decay time of the fluorescence activity from single-colour excitation to the $5P_{3/2}$ to be much less than the natural lifetime, which we conclude to be due to atomic time of flight. We also perform pulsed excitation to the $5D_{5/2}$ state using a two-colour scheme in various geometries, and produce a Monte Carlo wavefunction simulation to model this. We conclude that, in this case involving the longer lived $5D_{5/2}$ state, velocity selectivity and time of flight both impact the measured timescale, and use our simulations to extract the contributing velocity classes. Due to the selectivity imposed by our cells, we measure a decay timescale of $38.71(13)\,ns$ in a $1\,\mu m$ cell, despite the mean atomic time of flight being only approx. 3 ns. We discuss the implications of our results in the context of both fundamental physics and technological applications throughout.

Supervisors: Prof. C. Stuart Adams and Prof. Ifan G. Hughes

Acknowledgements

Firstly, I would like to thank my supervisors: Prof. C. Stuart Adams and Prof. Ifan G. Hughes. To Stuart for his endless list of exciting new ideas and keenness to discuss and investigate interesting new physics problems, and to Ifan for his constant support and wealth of experience and knowledge in our field. As well as my supervisors, I must thank Dr. Dani Pizzey firstly for her wealth of experimental know-how, but mainly for always being there to have a healthy rant about physics and life in general!

Secondly, I would like to thank the whole QLM research group and Durham Physics as a whole. I could not have asked for a better and more supportive community within which to complete my PhD. A special mention must go to fAtMol for making Wednesday afternoons a little bit less painful, to footMol for allowing me to exercise off Wednesday's cake, and to Friday seminars for facilitating stimulating discussions on many key physics problems. I hope QLM continues to be the social and welcoming group that it has been during my time here.

Thirdly I would like to thank all my friends within QLM and further afield, including those I met through the great Durham University Hillwalking Society. There are too many names to list individually, but thank you all for supporting me and keeping me jolly throughout this journey. I couldn't have done it without you!

Finally, I would like to show my immense gratitude to my parents, who have always acted to support and encourage me throughout life in general and particularly during my PhD. Thank you for always being there and helping me through everything, despite not understanding what I do with atoms and lasers all day!

Contents

Declaration

The work in this thesis is based on research carried out in the Quantum Light and Matter group, Department of Physics, University of Durham, England. No part of this thesis has been submitted elsewhere for any other degree or qualification, and it is the sole work of the author unless referenced to the contrary in the text.

Some of the work presented in this thesis has been published in journals - the relevant publications are listed below.

Publications arising from this work

[1] T. F. Cutler, W. J. Hamlyn, J. Renger, K. A. Whittaker, D. Pizzey, I. G. Hughes, V. Sandoghdar, and C. S. Adams. Nanostructured alkali-metal vapor cells. *Phys. Rev. Applied*, 14:034054, Sep 2020.

Related publications

[2] S. Ribeiro, T. F. Cutler, C. S. Adams, and S. A. Gardiner. Collective effects in the photon statistics of thermal atomic ensembles. *Phys. Rev. A*, 104:013719, Jul 2021.

List of Figures

Chapter 1

Introduction

Atomic physics has long been a driver of improvements in our knowledge of fundamental physics concepts, as well as of technological enhancements. Thermal vapour experiments account for a significant proportion of this research, and have shown promise for applications including optical filtering [3–5], optical memories and storage [6, 7], magnetometry and sensing [8], laser stabilisation [9, 10], and as sources of single photons [11]. Recently, thermal vapours have facilitated technological advancements in fields as diverse as terahertz detection [12] and medical sensing [13]. Some recent works have focused on interfacing and combining atomic systems with other features such as plasmonic structures [14] or photonic structures [15], towards the development of novel technology platforms. Moreover, miniaturisation of such thermal vapour platforms has opened the field to the development of portable and scalable atom-based devices [16,17]. Despite this breadth of research, there are still many open questions around the fundamental physics of atom-light interaction, stimulating much ongoing research [18].

Thermal vapour experiments have numerous advantages over cold atom experiments for the study of atomic physics. Chiefly, they require a much reduced number of lasers and optical components - the simplest of experiments can be done with a single laser, a single vapour cell, a detector, and some calibration optics. This is in contrast to the laboratory-scale experiments including numerous laser systems and vacuum chambers for cold atom studies. However, thermal vapours also have drawbacks - most notably in terms of motional effects, which will be discussed throughout this thesis. Some work has been done towards mitigating the negative impacts of motional dephas-

ing [19,20], whilst thin cells are also a promising candidate for the mitigation of effects arising due to thermal atomic motion, as will be shown later in this work.

Thermal vapour experiments produce large amounts of data and thus modelling has long been of key importance. Due to this, there now exists considerable knowledge of the theoretical treatment and modelling of thermal vapour systems and their spectral responses [3, 21, 22], making them a convenient basis for many investigations. Despite this knowledge, there are still many open questions and new frontiers existing within the field. In this thesis we will perform novel thermal vapour experiments using bespoke micro- and nano-scale vapour cells. In the rest of this chapter, we will introduce the broader field within which our work lies, and discuss the motivations and inspirations we have taken from this.

1.1 Motivation

The work in this thesis using thermal vapour cells with micro- and nano-scale confinement lies within a broad field of atomic physics interests, from the fundamental knowledge of the interaction of light and atoms, to the applied areas of atom-based technologies and devices. Our work is influenced by this vast field and where its future research interests lie. In the following sections we will discuss both of these areas in more detail, to contextualise and motivate our own studies.

1.1.1 Fundamental physics investigations

Single atoms are generally regarded as perfect quantum systems with wide-ranging applications, and considerable research has been devoted to trapping, isolating, and probing single atom or single dipole systems [23–27]. For experiments using thermal vapours however, very little work has focused on reaching low atom numbers. This is owing to the restrictive nature of the thermal atom system, notably including undesirable motional effects (such as transit time broadening) and the limitations on interaction times that are achievable. This is in addition to the complete inability to reach such low atom number regimes in conventional vapour cells - due to constraints on accessible number densities and interaction volumes. Two exceptions to this have

been using thermal Rydberg ensembles and related work using atomic beams. For atomic beams, anti-bunching has been observed by using a low atomic current so as to only interact with one or two atoms at one time [28]. For thermal Rydberg ensembles, the addition of the Rydberg blockade allowed for promising initial developments towards single-photon sources in micron-scale (the order of magnitude of the Rydberg blockade radius) cells [11]. However, for Rydberg atoms the often-stated benefit of long-range interactions can also lead to issues such as unwanted interactions with cell walls and other complex structures one might hope to interface atoms with, especially when working towards miniaturised atom-based devices.

At the other extreme end of the atom-number scale, the probing of high densities of atoms allows for the study of collective atomic behaviour. To probe such effects, it is desirable to enter a regime where the average distance between adjacent atoms is less than the excitation wavelength, characterised by a number density (n) such that $n \gg k^3$ (where $k = 2\pi/\lambda$ and λ is the excitation wavelength) [29–31]. At such densities, dipole-dipole interactions between atoms become significant, and the medium must be treated as an ensemble rather than individual emitters. Non-linear effects such as non-classical scattering [32], the dipole blockade [33], and the collective Lamb shift [29, 34] become significant in this regime. There has been some effort to manufacture vapour cells which can withstand the high temperature operation required to facilitate the high atomic densities necessary for observing collective behaviour, however this can prove difficult [35].

For standard experiments with alkali-metal atoms the excitation wavelength is generally less than 1 µm. Thus, at the atomic densities required to reach this regime, the absorption of resonant laser light by the medium quickly becomes 100%, even for modest path lengths. Furthermore, re-absorption and re-scattering of emitted photons becomes increasingly common. This limits the ability to perform measurements on high density ensembles in conventionally-sized thermal vapour cells. Thin cells can mitigate these problems, as will be discussed below. It has even been suggested that atomic behaviour is altered in the presence of tight confinement, with line-shifts and broadenings being observed with varying cavity lengths [36], and this is another motivation to perform studies in such confined regimes.

As illustrated in Fig. 1.1, rubidium vapour (which will be our alkali-metal atom of choice throughout this thesis) has a favourable number density curve

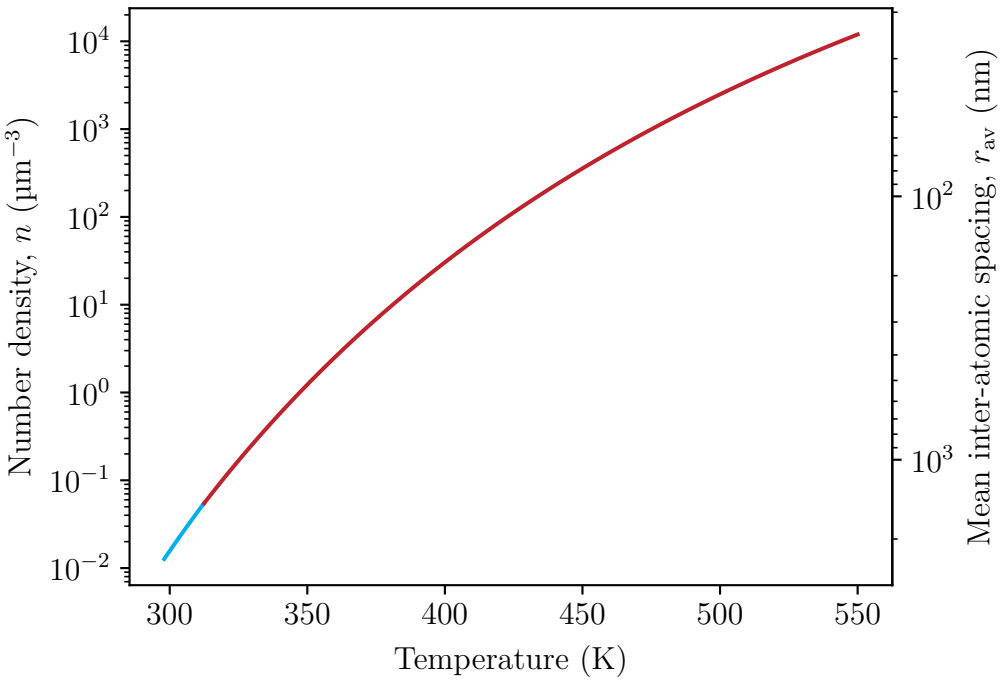

Figure 1.1: The variation of rubidium number density, n, (plotted here in cubic microns) with temperature. Values were calculated using vapour pressure equations valid in a conventional vapour cell (i.e. for an equilibriated steady-state system), obtained from [38]. A secondary axis (right) shows the corresponding mean inter-atomic spacing, calculated using $r_{\mathrm{av}} = 5/9\, n^{-1/3}$. Note that rubidium is a solid below 312 K (blue line), and liquid above this (red line).

for our work, which is emphasised when plotted on the scale of cubic microns. A modest temperature variation of 150 K facilitates the exploration of four orders of magnitude in atomic density, beginning with of order one atom on average per cubic micron at 350 K, up to one thousand at 500 K. These are temperatures that lie within easy reach for standard laboratory equipment and thermal vapour cell experiments. The plot also shows the variation in density in terms of the mean inter-atomic spacing on the secondary axis, which illustrates that one can access regimes where the spacing is smaller than the excitation and emission wavelength (which is 780 nm for the majority of this work) as well as where it is much larger. This suggests that by simply varying temperature we can move smoothly between regimes where collective behaviour is important and where it is negligible [37].

Interrogation of atoms on the scale of single cubic microns is not within

easy reach for standard thermal vapours experiments. Our nano-cells, however, are designed with such experiments in mind. The thin (0.5 mm) front panel allows for the use of high-NA optics to produce small interrogation and collection spot sizes at the location of the vapour which can be of the order of 1 µm (for example, a NA= 0.7 aperture is used to probe atoms within structures with sizes of less than 1 µm later in this work). In terms of confinement, dimensions of less than 1 µm are within easy reach using our etching methods [1]. Combining both confinement and tight-focusing, an interaction volume of order one cubic micron is now easily achievable. Thus our nano-cells open up novel regimes for the study of fundamental physics in thermal vapours, facilitating the small volumes necessary for the pursuit of low atom numbers and single atom behaviour, and also the short path lengths required to probe high density vapours without excessive absorption and re-scattering. The high-NA focusing can also be used to achieve high intensities of excitation laser light and thus high Rabi frequencies, and our thin cells mean that these excitation regions are uniform across our cell thickness (for which it is necessary that the cell thickness is less than the Rayleigh range). All of this demonstrates the breadth of possibility facilitated by bespoke micro- and nano-scale vapour cells.

In thin cells the interaction of atoms with the cell walls becomes important. There is much interest in the behaviour of emitters close to surfaces [39–43]. Systems on reduced lengthscales, where all atoms reside close to surfaces, have been crucial for a number of recent fundamental physics investigations, including into collective atomic behaviour [36, 44], atom-surface van der Waals interactions [45–47], and the cooperative Lamb shift [29, 34]. These areas are of interest not only from a fundamental physics standpoint, but also when considering technological applications and miniaturised devices (where atoms close to surfaces become increasingly common), as will be discussed in the following section.

1.1.2 Miniaturised atom-based devices and technologies

Miniaturisation of atom-based platforms to the on-chip scale has been a key area of development in recent years, towards the goal of scalable devices [48–55]. With the advent of vertical-cavity surface-emitting lasers (VCSELs)

and other miniaturised technologies [17], it is becoming increasingly possible to manufacture fully integrated and portable devices. Vapour cells are also becoming increasingly miniaturised, and the rise of micro-electromechanical system (MEMS) cells has also allowed for more compact setups [56]. But with miniaturisation comes new challenges; firstly in engineering ever smaller devices, and secondly in understanding the underlying physics that needs to be harnessed to realise such devices. For example, some applications require miniaturised vapour cells [16, 53, 57–60], and within such cells atoms are increasingly subject to atom-wall interactions and transit time effects. Thus it is paramount for the community as a whole and for the future development of atom-based devices that the fundamental physics of atom-light interaction at ever-reducing lengthscales is studied and understood. The work presented in this thesis aims to add to the body of knowledge in both the areas of atom-light interaction at reduced lengthscales and of methodologies for the fabrication and characterisation of nano-scale features useful for miniaturised devices.

There has been increasing interest in recent years in coupling guided light modes confined to waveguide structures with thermal vapours. For example, in [61], a 50 nm slot waveguide structure is used and interfaced with a dense thermal cloud of atoms. In another work, thermal atoms within micrometric distances of the surface of a nano-fibre have been interfaced with guided light modes [62]. Further experiments have filled hollowcore fibres with thermal atomic vapours, which then interact with the guided light mode within. Such experiments have suggested potential applications in quantum optics [63]. However, these experiments are limited by long fibre loading times due to diffusion timescales in these small volumes [64]. There has also been recent interest in confinement of atoms to cavities [36]. In all of these instances, atoms are within microns or nanometres of surfaces, and thus the physics of such systems must be well understood when developing technological applications.

Magnetometry has also been a large area of research interest in recent times, with thermal vapours proving a promising candidate for compact and high-sensitivity devices [8, 65]. There is increasing need for compact and portable magnetometers, for example for medical applications [66], including for monitoring human heart [67–69] and brain [70] activity. One study even uses this technology to monitor heart activity in animals [71]. As well as

these potential applications, magnetometry on micrometre lengthscales has begun to be studied, with thin cells proving a promising candidate for high spatial resolution magnetic field mapping [72, 73].

Other suggested applications of thin cells include the imaging of knotted vortex light beams through interaction with a thin vapour - such vortex features can have a spatial extent of order microns [74], and thus imaging which can select only this portion of the beam is required. As well as this, thin cells have been posed as a possible source for narrow-band fluorescence photons (due to the velocity selective nature of thin cells which will be discussed in detail later in this work), and in this thesis preliminary fluorescence measurements will be presented.

1.2 Thesis structure

In this chapter we have discussed the motivation for our investigations and the landscape of other studies and technologies within which our work lies. We will follow this in chapter 2 with a treatment of the basic theoretical principles of atom-light interaction which underpin the work throughout this thesis.

In chapter 3 we will discuss our fabrication techniques for producing cells with internal confinement dimensions of the order of hundreds of nanometres ('nano-cells'), as well as the characterisation of such cells, details about their operation, and advancements that have been made to their design and capabilities throughout the course of this work. These cells form the platform for all experiments described in the rest of this thesis.

In chapter 4, we investigate the application of the light induced atomic desorption (LIAD) effect to thin cells, for controlled on-demand increase of optical density in regions on the micron-scale. We also observe a competing effect which we term LICo (light induced condensation), whereby areas of condensed atoms can be induced on the cell walls using laser light. We discuss the two effects and their potential applications.

In chapter 5, we move on to applying various spectroscopy techniques to thermal rubidium vapours within our nano-cells. We discuss the benefits and drawbacks of a number of fluorescence-based schemes, and measure the lineshapes produced by each. Specifically, we will discuss two-colour excitation of rubidium atoms to the $5D_{5/2}$ state in both co- and counter-propagating beam

geometries, and apply the former to study the behaviour and distribution of atoms confined to a $1\,\mu m \times 1\,\mu m$ channel.

In chapter 6, we investigate the temporal dynamics of excitation and emission processes of atoms confined to micro- and nano-cells by employing nanosecond resonant laser pulses. This allows us to study in more detail the underlying fundamental physics, and make inferences around the velocity selection induced by micro- and nano-scale confinement. We study pulsed excitation experimentally in both one- and two-colour schemes, and develop a theoretical Monte Carlo wavefunction model for the excitation and emission dynamics. We discuss and compare the atomic behaviour in regions of the cell between $2\,\mu m$ and $500\,nm$ in thickness and channels as small as $0.8 \times 0.5\,\mu m$. We also experimentally measure the photon statistics of the emitted light in the single-colour scheme.

Chapter 2

Atom-light theory

In this chapter we will establish some of the key theoretical concepts that underpin the work presented in the rest of this thesis. We will begin with a general description of the calculation of atomic structure and the interaction between atoms and light fields. We will then move on to discussing specific physics relevant for atoms confined to thin cells, including spectral line broadening and narrowing mechanisms due to atomic times of flight and atom-wall interactions. We will define terminology used throughout the rest of this thesis, as well as link the theoretical concepts with experimentally-measurable quantities.

2.1 Atomic structure

The alkali metals can be described as hydrogen-like atoms, having a single electron in their outer shell. The energy level structure of such atoms is well understood, and the basis of this understanding will be explained in this section. Similar derivations can be found in any respectable quantum mechanics textbook.

Quantum mechanically, we can describe a system by its Hamiltonian, $\hat{H}$, and wavefunction ψ in the well known time-independent Schrödinger equation

$$\hat{H}\left|\psi\right\rangle = E\left|\psi\right\rangle, \tag{2.1}$$

where E is the energy of the state. For our system, the Hamiltonian has a

general form

$$\hat{H} = \frac{\hat{p}^2}{2m} + V(r), \tag{2.2}$$

where the two terms describe the kinetic and potential energy of the electron respectively. Solving this equation yields stationary states of the form

$$E_n = \frac{-Z^2}{2n^2} E_h, \tag{2.3}$$

where Z is the atomic number, n is an integer, and E_h is the atomic energy unit. This is given by

$$E_h = m_\mathrm{e}\left(\frac{e^2}{4\pi\epsilon_0\hbar}\right)^2, \tag{2.4}$$

with m_e the electron mass, e the elementary charge, and ϵ_0 the permittivity of free space. As such, we have a series of discrete energy states which depend on n, which is thus a quantum number describing the gross structure of the electronic energy levels. This is often termed the principal quantum number.

We have defined n above, however there are further corrections which give rise to further quantum numbers which we use to describe our energy states. A detailed derivation can be found in any good quantum mechanics textbook, but we will describe them and their origins briefly here so as to define the notation and terminology used throughout this work. The azimuthal quantum number L can take any integer value, and denotes the orbital angular momentum of the electron, with $L = 0, 1, 2, 3$ denoting orbitals commonly referred to as S, P, D, F. The electron also has a spin angular momentum S, and the coupling of these angular momenta gives the total angular momentum quantum number $J = L + S$. This gives rise to atomic fine structure. Furthermore, we must consider the atomic nuclear spin I, which couples to the total angular momentum to give the quantum number $F = I + J$. The levels described by this quantum number are the hyperfine structure of the atom. Each F level also has $2F + 1$ magnetic (Zeeman) sub-levels (which are degenerate when no magnetic field is present). These are conventionally labelled with the m_F quantum number and have integer values that satisfy $-F \leq m_F \leq F$.

Throughout this thesis we will use rubidium as our atomic vapour of choice. Rubidium has two naturally-occurring isotopes, ^{85}Rb and ^{87}Rb. Their ground states are the $5\mathrm{S}_{1/2}$ states, where we have introduced the nL_J term symbol notation that will be used throughout this work. This is a simplifica-

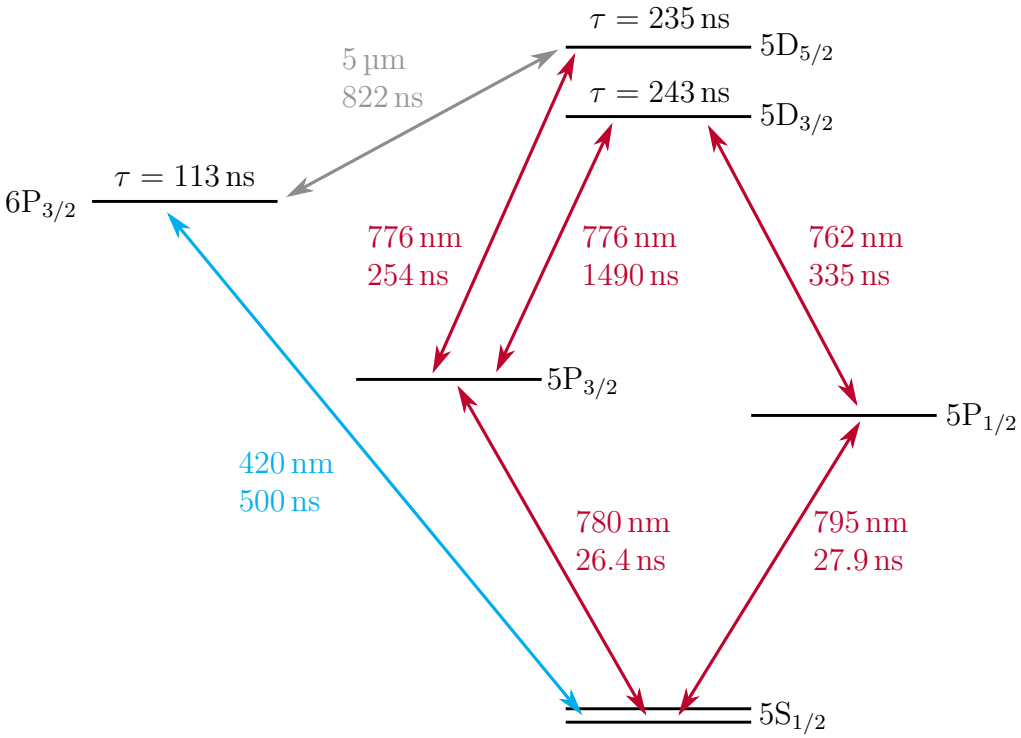

Figure 2.1: Diagram showing some key rubidium energy levels of interest in this work, with lifetimes of states (τ) and the wavelengths and lifetimes associated with individual transitions. Lifetimes were obtained from [75]. Each energy level also has associated hyperfine structure, which is only indicated for clarity for the $5S_{1/2}$ ground state.

tion of the conventional term symbol notation ($n^{2S+1}L_J$), where S is the spin. For this work the spin is dropped as it is the same for all states. Each ground state has two associated F hyperfine levels (the values of which are generally listed after the term symbol, e.g. $5S_{1/2}$ $F = 0$). Accounting for all of the above, we can map out the energy levels of our rubidium atoms. Shown in Fig. 2.1 are some commonly probed energy levels, with the hyperfine structure within each level other than the ground state omitted for clarity. Also shown are associated state lifetimes. In this thesis we will mainly focus on the excitation pathway involving the $5P_{3/2}$ and $5D_{5/2}$ states. However, the numerous different experimentally-accessible excitation and emission pathways afforded by the complex energy level structure has allowed for a wide breadth of previous research.

2.2 Atom-light interaction

Electromagnetic fields (such as laser light) can be used to change the state of our atomic system. Generally we use the semi-classical approach to treat the theory of such interactions, whereby we consider the atom quantum mechanically but the radiation as a classical field. The total Hamiltonian of the system is then

$$H = H_0 + H_{\text{int}}(t), \tag{2.5}$$

where H_0 is the atomic Hamiltonian and H_{int} is the Hamiltonian describing the interaction between the atom and the field. For a two-level atom the atomic Hamiltonian can be written

$$H_0 = \begin{pmatrix} E_1 & 0 \\ 0 & E_2 \end{pmatrix}, \tag{2.6}$$

where E_i are the energies of the states.

Treating the radiation field classically, and making the dipole approximation, we have $\mathbf{E} = E_0 \mathbf{e} \cos \omega t$, where ω is the frequency and E_0 the amplitude. This interacts with the atom via the dipole operator μ, and defining the Rabi frequency

$$\Omega(t) = \frac{\langle 1 | \, \mu E_0 \, | 2 \rangle}{\hbar} = \frac{E_0 \mathbf{d}_{21}}{\hbar}, \tag{2.7}$$

with $\mathbf{d}_{21}$ the dipole matrix element between states 1 and 2, we find the total system Hamiltonian

$$H = \frac{\hbar}{2} \begin{pmatrix} E_1 & \hbar\Omega(t) \cos \omega t \\ \hbar\Omega(t) \cos \omega t & E_2 \end{pmatrix}. \tag{2.8}$$

The Rabi frequency, as defined above, quantifies the strength of the atom-light coupling. Rabi frequencies quoted throughout this work will be defined in this way. The dipole matrix elements ($\mathbf{d}_{21}$) for common transitions in rubidium are well known [75]. For more complex situations requiring more than two levels (e.g. interaction with a pulse with bandwidth larger than the hyperfine splitting of the excited state), we will take the approach of averaging the different dipole matrix element contributions for the various transitions involved [21]. For an incident light field not on resonance, the atom-light

coupling strength is quantified by the generalised Rabi frequency, defined as

$$\tilde{\Omega} = \sqrt{|\Omega|^2 + \Delta^2}, \tag{2.9}$$

where we have introduced the concept of the (angular) detuning, Δ. This is defined as $\Delta = \omega - \omega_0$, where ω is the frequency and ω_0 the resonant transition frequency. Note that in experiments it is $\Delta/2\pi$ (which we will term the linear detuning) which is generally measured, and thus this will be quoted throughout the rest of this thesis.

Taking equation 2.8, we can further simplify the maths by making a unitary transformation and transforming into a frame which rotates with the frequency of the driving field. We then make the rotating wave approximation by neglecting the rapid oscillation terms. We will not show the full maths here, but the result is that for our two-level system we can write the Hamiltonian as

$$H = \frac{\hbar}{2}\begin{pmatrix} 0 & \Omega \\ \Omega & -2\Delta \end{pmatrix}. \tag{2.10}$$

We can extend our two-level atom picture shown in equation 2.2 to an N-state system defined by an $N \times N$ Hamiltonian involving the detunings from each state and the Rabi frequencies for each transition.

The above treatment, however, only describes the coherent evolution of the system. For the work in this thesis, we must also consider the incoherent part, i.e. spontaneous emission. For this we must introduce the density matrix, defined as

$$\rho = |\psi\rangle \langle\psi| . \tag{2.11}$$

The diagonal elements of the density matrix describe the population of the state in question, whilst off-diagonal elements describe the coherence between states. To describe the coherent time evolution of the density matrix we use the Liouville equation

$$i\hbar\frac{d\rho}{dt} = [\hat{H}, \rho], \tag{2.12}$$

where $[\hat{H}, \hat{\rho}]$ is the commutator between the Hamiltonian and the density matrix. To add in the incoherent evolution we add a second term to give the Lindblad Master equation [76, 77]

$$i\hbar\frac{d\rho}{dt} = [\hat{H}(t), \rho(t)] + i\hbar\sum_n \frac{1}{2}[2\hat{C}_n\rho(t)\hat{C}_n^\dagger - \rho(t)\hat{C}_n^\dagger\hat{C}_n - \hat{C}_n^\dagger\hat{C}_n\rho(t)]. \tag{2.13}$$

The additional term incorporates the collapse operators $\hat{C}_n$. These operators have units of $s^{-1/2}$, and after a quantum jump the system collapses into an eigenstate of $\hat{C}_n$. For example, for the collapse from state $2 \rightarrow 1$, we would have

$$\hat{C}_{21} = \sqrt{\Gamma_{21}} \left|2\right\rangle \left\langle 1\right|, \tag{2.14}$$

where Γ_{21} is the line-width for the transition. By summing the contribution of all possible collapse operators we can model the incoherent part of the evolution of the system.

By solving the Master equation we can find the temporal dynamics of a system with a given starting wavefunction and collapse operators. This is especially important for studying the physics of atoms confined to small volumes or interacting with small laser spots, as the time which the atoms spend interacting with the light field is short and thus a steady state solution for the ensemble may not be reached. Thus conventional modelling employed for centimeter-scale vapour cells and millimeter-sized laser beams (where the steady-state solution for ρ is sought) is often not valid in the regimes studied in this thesis.

2.2.1 Spectral line-shapes and widths

When performing spectroscopy, spectral lines have a line-shape and finite width about the discrete energy level value due to a number of effects. Most fundamentally, the finite lifetime of the excited states induces a Lorentzian line-shape, which can be understood through the Fourier transform of the finite lifetime into the frequency domain. This line-shape has the form

$$L(\Delta) = \frac{1}{2\pi} \frac{\Gamma}{\Delta^2 + \Gamma^2/4}, \tag{2.15}$$

where Γ is the decay rate of the state (and also the FWHM of the line-shape). As an example, the most commonly used state in this thesis - the rubidium $5P_{3/2}$ state - has $\Gamma \sim 2\pi \cdot 6\,\mathrm{MHz}$.

In a thermal vapour, atomic motion also further broadens spectral lines. Each atom experiences a different transition frequency due to the Doppler effect, where the effective detuning experienced by each atom becomes $\Delta + kv$, with v the atomic velocity. As each atom experiences a different effective detuning, any models must incorporate the velocity distribution of the thermal

atomic ensemble. This distribution leads to Doppler broadening, which is Gaussian in nature. Accounting for both the Doppler broadening and the natural Lorentzian line-shape gives a Voigt profile [21], which is the convolution of a Gaussian and a Lorentzian line-shape. For a room temperature rubidium vapour, the FWHM of the Doppler-broadened line-shape is of the order 0.5 GHz. This means the hyperfine structure of the excited states cannot be resolved with conventional spectroscopy setups (e.g. the splitting of the $5P_{3/2}$ hyperfine states is of order 100 MHz).

Spectroscopy is a commonly used experimental method of probing an atomic ensemble. By comparison with careful modelling, the features of a spectrum can yield information about the ensemble, including the velocity distribution. The simplest of experiments using rubidium record transmission or fluorescence on the D1 or D2 lines (795 nm and 780 nm respectively). Rigorous models based on the treatment above already exist for such spectra (at least in the weak probe regime, where effects such as optical pumping are negligible [21]) [3, 22]. However, more complex experiments involve higher levels, for example four wave mixing employing the 5D states (see Fig. 2.1). Spectroscopy done when using two lasers to excite atoms to the $5D_{5/2}$ state is presented in chapter 5.

2.3 Thin cell physics

There are extra theoretical considerations for thermal vapours confined to thin cells as compared to those in conventional cells. In this section we will outline these considerations and their effect on the behaviour of the atomic ensemble and its resulting spectral response. These concepts will be referred back to throughout this thesis and are key to understanding the fundamental physics underlying our experimental results.

2.3.1 Atom-wall interaction

In a sufficiently thin cell, a significant proportion of atoms reside close to the cell walls. For atom-surface van der Waals interactions (whose strength decays with distance r from the walls as $1/r^3$ [78]), a significant contribution to spectral features is observed for confinement of a few hundred nanometres or less. The C_3 coefficient of proportionality characterising the van der Waals

atom-wall interaction has already been measured in thin cells, for atoms of various alkali metals which reside within tens of nanometres of cell walls [46, 47, 79].

Similarly, the adsorption and desorption dynamics between the atoms and the cell walls are notable in the thin cell regime. In the steady-state, the rates of the two processes must be equal, and parameters such as the dwell time of atoms on the cell wall become important. For thin cells, the time of flight of atoms before a wall collision is generally short (down to a few nanoseconds on average for a 1 µm cell), and thus these processes can have impact on measurements. Vapour density is not allowed sufficient time to equilibriate across the cell due to the slow atomic diffusion dynamics, which are due to frequent atom-wall collisions and associated dwell times in a thin cell. Thus localised vapour density is influenced by the local population of wall-adsorbed atoms and their dynamics. There is still much to learn about the processes which underpin these atom-wall effects in thin cells, and how they influence related phenomena such as LIAD (which will be discussed in detail in chapter 4).

2.3.2 Velocity distribution and confinement

The velocity distribution of atoms in a thermal ensemble is a key consideration in experiments with thermal vapours. As discussed in section 2.2.1, in a conventional centimeter- or millimeter-sized cell, atoms with a non-zero velocity parallel to the laser beam contribute to spectroscopic signals away from resonance due to the Doppler effect. This leads to Doppler-broadened spectral features, which can be GHz wide [3].

There is much interest in suppressing the motional dephasing of an atomic ensemble which occurs due to this velocity distribution [19, 20]. The effects of the broad velocity distribution in a thermal vapour can also be suppressed using thin cells. For this kind of experiment, a probe laser would be positioned perpendicular to the walls of the thin cell (i.e. along the axis of the confinement). Atoms with higher velocities parallel to the laser beam (and thus greater Doppler shift) collide with the cell walls more quickly than their slower counterparts, leading to a reduction in their interaction time and thus their relative spectroscopic contribution. This is a variant of Dicke narrowing, an effect first proposed in 1953 [80] to explain the narrowing of Doppler-

broadened spectral lines through collisional processes, and first observed in the optical regime almost half a century later (using cells with thicknesses ranging from 10 µm to 1 mm) [81]. Through this effect, a narrower subset of the thermal velocity distribution contributes proportionally more to measurements, and thus sub-Doppler features can be achieved without the addition of the extra laser beams that would be necessary to achieve similar results in conventional vapour cells [21].

The short interaction time also means that atoms are unlikely to spend enough time in the beam to reach a steady state (as they would for experiments on conventional lengthscales), and thus we cannot rely on, for example, the conventional steady-state solutions to the optical Bloch equations to describe the atomic populations in each state. As such, for simulations in this thesis we adopt a Monte Carlo wavefunction (also known as quantum jump) approach to model the behaviour of our atomic ensemble.

Monte Carlo methods generally rely on random sampling of a probability distribution to obtain numerical results. For our specific case, we will calculate the evolution of individual atoms sampled from an ensemble with a distribution of velocities and positions within our thin cell. By using this method we can compute the overall evolution of the ensemble by averaging over calculations done for individual atoms. Each atom is propagated through a series of discrete time-steps modelling the temporal state dynamics including coherent and incoherent processes. Both the coherent evolution and incoherent evolution is modelled by solving the Lindblad master equation (as discussed in section 2.2) for each time step. The motional state of each atom is modelled classically. The methodology is described in greater detail in appendix B, and can be easily adopted using QuTiP [77]. QuTiP is an open-source and optimised python package which provides convenient functions for performing numerical simulations of quantum mechanical systems, including Lindblad and Monte Carlo solvers. More information can be found in the QuTiP documentation.

As an illustrative example, we have modelled the relative fluorescence activity contributions from different atomic velocity classes for two cases: the case of a transmitted laser beam perpendicular to the walls of a thin cell; and the case of a total internal reflection fluorescence (TIRF) excitation scheme in the same cell. The difference between the two schemes is illustrated schematically in Fig. 2.2. A TIRF scheme induces an evanescent field (which

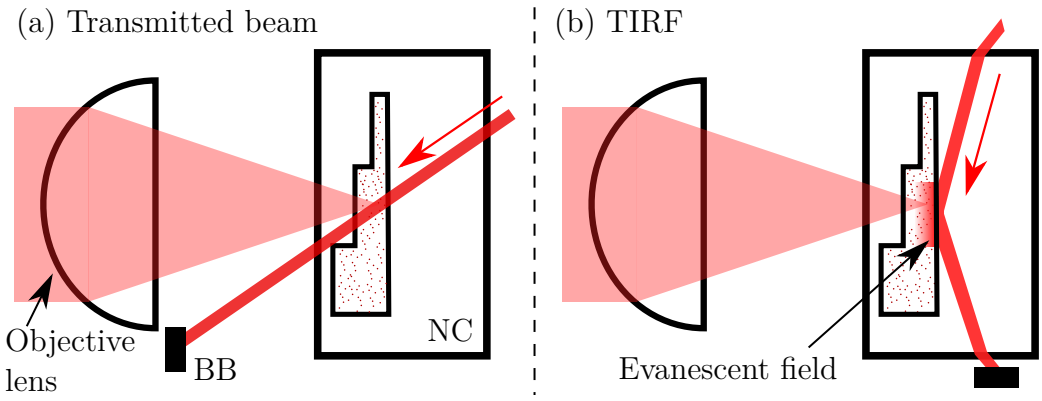

Figure 2.2: Schematic diagrams of two excitation schemes used in this work (not to scale). **(a)** The off-axis transmitted beam scheme, whereby a laser beam is transmitted through the vapour region at an angle, and fluorescence is collected via an objective lens. **(b)** The TIRF case, where the excitation laser is instead totally internally reflected at the back face of the vapour region, generating an evanescent field (which decays exponentially from the surface with of order 100 nm 1/e extent). Atoms in the evanescent field can be excited and their fluorescence is collected as in (a). In both cases the exiting laser beam is blocked using a beam block (BB). The nano-cell is denoted as NC.

can be of order 100 nm in extent) in the vapour region, which interacts with the atoms. This gives even greater positional selectivity than the thin cell itself. Previous studies in thin cells have discussed and studied the TIRF method in more detail [1, 82]. For the simulations, we initialised 10^4 atoms, each with a random x, y, z coordinate distributed across a 1 µm cell thickness and a velocity chosen from the Maxwell-Boltzmann distribution. We subject them to excitation by a single resonant continuous wave (CW) laser beam until such time that they collide with a cell wall, which we take to mean that they de-excite non-radiatively. Note that, for the purposes of this simple illustrative simulation, we consider each atom to behave as a two-level system. However, it is possible (as will be done later in chapter 6) to extend this modelling to N-level systems.

The velocity distribution of the atoms which contribute to fluorescence activity is shown in Fig. 2.3, in purple for the case of an excitation laser beam at normal incidence to the cell walls. We see that there is a broad base, on top of which there is a much narrower class of velocities that contribute proportionally more to fluorescence activity. This is the origin of the empirical bi-modal velocity distribution which has been used in previous nano-cell

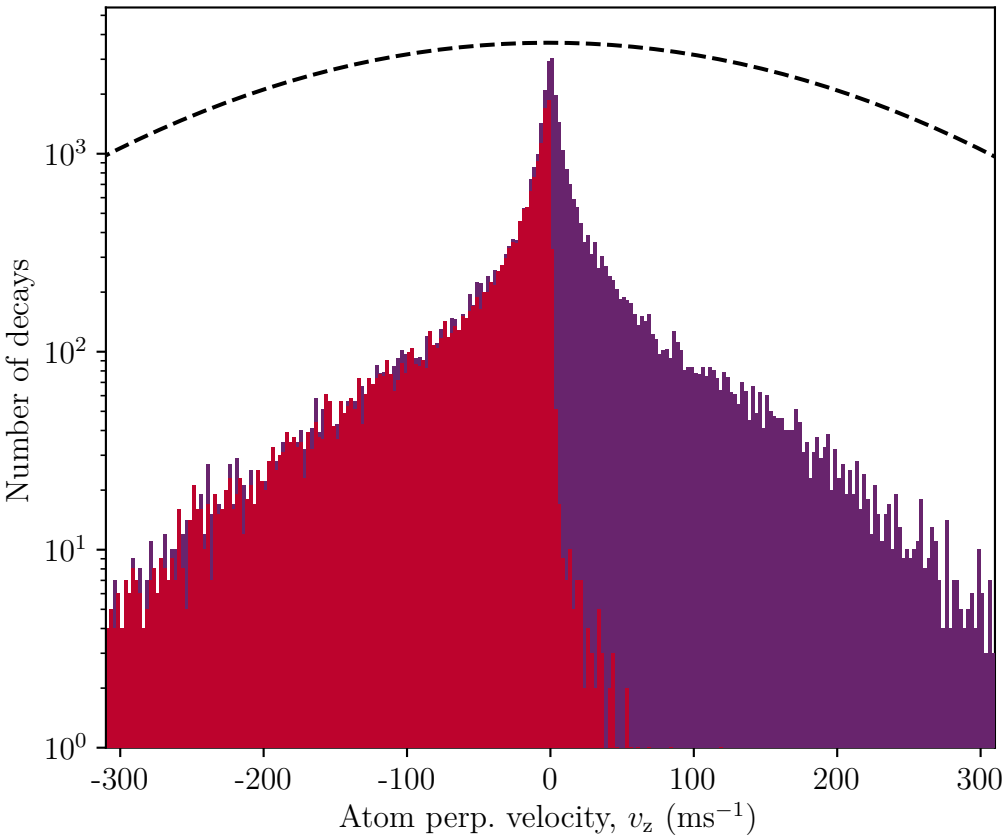

Figure 2.3: Velocity distribution of atoms that contribute to fluorescence activity in a 1 µm thin cell, for the cases of an excitation laser beam at normal incidence (purple), and evanescent excitation region with a characteristic decay length of 80 nm (red). The Monte Carlo quantum jump simulation was initialised with 10^5 atoms, and a 'new' atom was seeded when an atom collided with a wall. The excitation Rabi frequency was chosen to be 100 MHz and the laser light was resonant. The black dashed line indicates a typical Maxwell-Boltzmann atomic velocity distribution for comparison.

simulations, for example [37]. A section of the starting Maxwell-Boltzmann velocity distribution used in the simulation is also shown for comparison.

Furthermore, our nano-cell design geometry allows us to be even more velocity-selective, through the technique of TIRF. Our optically-polished outer cell faces allow for a laser beam to enter from the side of the cell at an angle and totally-internally reflect off the back of the nano-regions, imparting an evanescent field in the nano-region which can interact with the vapour atoms. The same simulation described above was run again but for an exponentially-decaying evanescent field with a realistic characteristic 1/e decay length of 80 nm. The result of this TIRF simulation is shown in red in Fig. 2.3. The

additional evanescent field constraint modifies the contributing atomic velocity distribution from being symmetric to one in which most atoms have a negative velocity component in the confinement direction.

It must be noted that evanescent excitation, whilst further narrowing the contributing velocity distribution, also induces increased transit time broadening (as will be discussed in section 2.3.3) and thus cannot be used to achieve increasingly narrow spectral features. However, being able to isolate specific velocity classes within a thermal atomic ensemble may pave the way towards increasingly controlled experiments with thermal vapours.

2.3.3 Transit time

When studying atoms confined to small volumes, the atomic time of flight before a collision with surfaces is an important consideration. As described in section 2.3.2, this time of flight leads to a selective enhancement of the contribution of atoms which are travelling slower in the direction perpendicular to the walls. But for increasingly thin cells or excitation regions, the short transit time across the cell induces broadening. The width of such broadening has the general form

$$\Gamma_{\text{tr}} = \frac{\alpha}{t_{\text{tr}}}, \tag{2.16}$$

where t_{tr} is transit time, and α is a dimensionless factor which depends on the geometry of the system [83]. For example, the relevant factor is $\alpha = 0.8$ for transit across a Gaussian laser beam (where the transit time is taken as $t_{\text{tr}} = 2w/v$, with v the atomic velocity and w the half width at half maximum of the Gaussian beam). We have measured this factor to be approximately $\alpha = 0.5$ for an exponentially-decaying evanescent excitation region in a thin cell [1]. Transit time broadening has also been characterised for atoms confined to the micron-scale in hollow-core fibres [84]. Transit time broadening leads to further deviation of the spectroscopic contributions of fast and slow atoms, as a faster ensemble will be broader due to the reduced transit time.

2.3.4 Collective behaviour

As is shown in Fig. 1.1, high densities of rubidium vapour atoms (up to the regime where the atomic spacing is less than $\lambda = 780\,\text{nm}$, and even $\lambda/2\pi$) can be achieved in a laboratory using moderate temperatures. Such high densities

may also be achievable through the process of LIAD, which will be discussed further in chapter 4. Such high densities in conventional cells would lead to high optical depths and thus be experimentally difficult to probe, however thin cells open up new opportunities to probe such high density ensembles. In fact, it is often advantageous to reach such high densities to mitigate the small atomic response observed from the small volume interrogated in a thin cell.

At such high densities, the behaviour of N dipoles cannot be obtained by simply summing the behaviour of a single dipole N times. This is due to collective behaviours, where the interaction between the dipoles modifies their response. This can be a disadvantage, giving rise to unwanted frequency shifts [85], as well as making theoretical modelling more complicated. However, the interaction between atoms can be controlled and used advantageously, generally by using ordered arrays of atoms [30, 86–88]. Collective behaviour is the origin of some commonly studied and exploited effects such as super- and sub-radiance [89–91]. One such collective effect that has previously been studied using thin cells is the collective Lamb shift [29, 34].

2.3.5 Other spectroscopic considerations

There are further line broadening mechanisms which will be relevant to spectra presented in this thesis. For thin cells, it is often convenient to use high laser powers to achieve fluorescence signals with high SNR (where in conventional cells much lower powers would be required). This means that power broadening of spectral line-shapes is often significant. Power broadening is an important consideration in the regime where the light intensity exceeds the saturation intensity of the medium, which can happen with powers as low as nanowatts for tightly-focused light modes of order of microns in extent. Power broadening has the form [92]

$$\Delta\omega \propto \Gamma\sqrt{1 + I/I_{\text{sat}}}, \tag{2.17}$$

where $\Delta\omega$ is the FWHM of the resonance, Γ the natural line-width, I the intensity and I_{sat} the saturation intensity. For example, the saturation intensity for ^{85}Rb $F = 3 \rightarrow F' = 4$ transition is $3.9\,\text{mW/cm}^2$. Power broadening, in combination with transit time broadening, has already been characterised for atoms confined to micron-scale hollow-core fibres [84].

As discussed previously in this chapter, high temperature operation is often advantageous when using thin cells. This leads to high atomic number densities, causing dipole-dipole interactions between atoms to become more significant. These interactions give rise to increased spectral line broadening in the form of self-broadening. The broadening observed is proportional to the atomic number density, and the proportionality coefficient for this effect has been both experimentally measured and theoretically calculated for a rubidium vapour [93]. The effect is generally incorporated in standard theoretical modelling [3].

2.4 Conclusion

In this chapter we have outlined the theoretical basis for much of the work discussed in this thesis. Whilst a full theoretical model for the response of atoms confined to a nano-cell incorporating wall interactions, optical pumping, and all of the above sources of broadening, is beyond the scope of this work, we will discuss our results throughout this thesis in the context of these considerations. Other theoretical works exist which treat the theory of confined vapours and their spectroscopy in more detail than is presented here. Theoretical treatment of the atom-light interaction including the transmitted and reflected modes in a thin cell, and including atom-surface interactions, is provided in [47]. An in-depth theoretical treatment of the eigenmodes of a thin vapour layer is also provided in [94].

Chapter 3

Thin cell fabrication and characterisation

3.1 Introduction

Fabrication of alkali-metal vapour cells with reduced lengthscales has been a rapidly evolving area of work in recent years. A multitude of methodologies for manufacturing cells now exist [95–97], spanning different substrates and design capabilities. Considerable continued research and development has focused on both miniaturisation of overall vapour cell footprints, as well as manufacturing increasingly small internal confinement dimensions. Cells on the millimetre-scale have been manufactured using various methodologies [56, 98–102], and the advent of cells on this scale enabled chip-scale atom-based technologies such as optical clocks [103] and magnetometers [16]. As well as this, millimetre cells have enabled the observation of physical effects such as coherent backscattering in the thermal vapour regime [7]. Cells with internal confinement on the micron scale have also been fabricated [104], and their potential for uses such as single photon sources has been demonstrated [11].

Nano-cell experimentation in Durham began with a fruitful collaboration with the National Academy of Sciences (NAS), Armenia, who fabricate wedge-shaped sapphire vapour cells with internal dimensions smoothly varying from microns to tens of nanometres [105, 106]. These cells are robust with operating lifetimes of the order of years, with operating temperatures up to 350 °C. Nano-cells with this design were used successfully at Durham and elsewhere to study a number of physical effects [29, 34, 45, 46, 107, 108]. Other

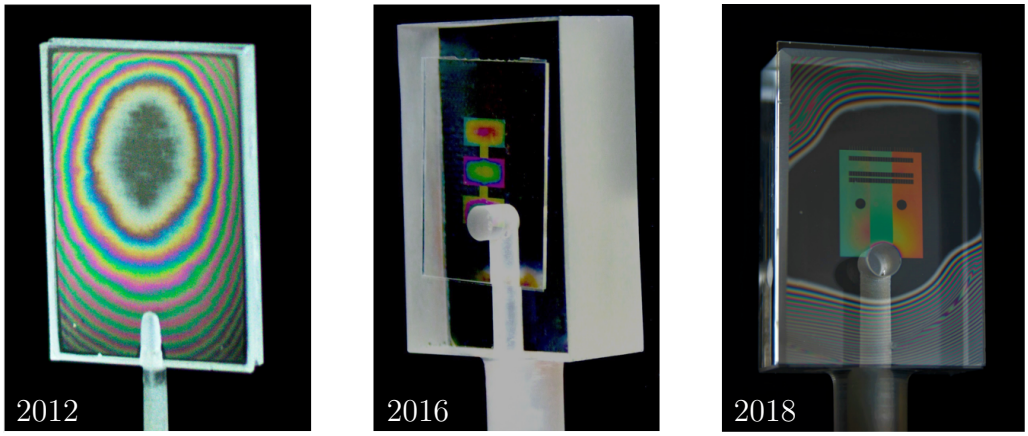

Figure 3.1: The evolution of nano-cell designs used in Durham. From left to right: the Armenian sapphire nano-cell, with wedge design; the first iteration of cells made in a collaboration between Durham and the Max Planck institute for the Science of Light (Durham-MPL), which feature a thin front panel and discrete thickness regions; and a more recent Durham-MPL cell, with discrete thickness regions, nano-structures, and all outer surfaces optically polished.

closely related cell fabrication work includes that of the Institute d'Optique (Paris, France), who have produced a methodology for fabricating similar 'super-polished' nano-cells [109], with low-roughness internal surfaces yielding potential benefits for the study of atom-surface interactions. Sub-micron cells have also been fabricated using a different methodology which includes etching and anodic bonding as outlined in [110], where the authors subsequently used these cells to demonstrate laser frequency stabilisation.

In Durham, extra customisability and versatility than that provided by the Armenian cells was desired for our next generation of experiments, and as such cell fabrication was brought in-house in a rewarding collaboration with the Max Planck Institute for the Science of Light (Erlangen, Germany). A timeline of nano-cells used in Durham, showing these Durham-MPL collaboration cells alongside an Armenian nano-cell, is shown in Fig. 3.1. The basic fabrication of our current generation cells follows the methodology outlined in reference [1]. The cells consist of three key parts: an optically polished glass block with a milled conduit, an etched 0.5 mm thick front panel, and an atom reservoir. The etched front panel is optical contact bonded to the block (optical contact bonding is a glue-free process bonding two smooth surfaces using only intermolecular forces [111]), before baking at 1000 °C for 6 hours at atmospheric pressure. The baking makes the bond permanent, and re-

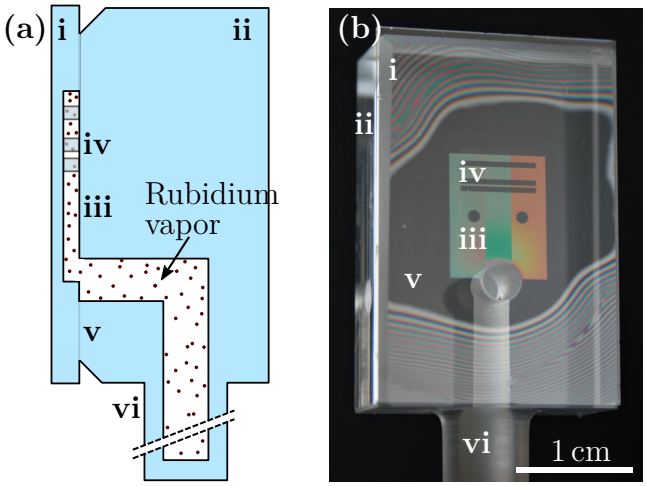

Figure 3.2: **(a)** Side cross-section schematic (not to scale) and **(b)** front-facing photograph of the nano-cell. The etched cover slide (i) is contacted onto the block (ii) such that the etched patterns form a nano-thickness region (iii) and nano-channels (iv) between the two glass pieces. An optical contact bond (v) surrounds the etched area to act as a vacuum seal. The rubidium reservoir below (vi) is attached to provide atomic vapor into the nano-structured region. This cell contains areas with confinement in both one and two dimensions. Two circular pillars are visible in (b), acting as spacers to reduce bowing. Newton's fringes are visible in the unbonded regions in (b), whilst interference gives distinct colours to the central confinement regions.

moves surface adsorbates. The cell is then evacuated to 10^{-6} mbar, and has a rubidium reservoir added through glass-blowing. A schematic of the key components of our cell is shown in Fig. 3.2, as well as a photograph showing these components in a finished cell. More detailed accounts of the fabrication process were presented in [82,108]. This generation of nano-cells has proven to be mechanically robust, with operating lifetimes of the order of years having been achieved.

Whilst our current generation of cells have a lower maximum operating temperature than the Armenian cells (due to the fused silica construction which reacts with rubidium at approximately 200 °C), they boast a number of key advantages when looking toward technological applications. Firstly, nano-structures can be etched into these cells in a highly customisable way, allowing the creation of near-arbitrary vapour confinement geometries. Secondly, the nano-region is close ($< 500\,\mu$m) to the front face of the cell, allowing for the use of conventional short working distance high numerical aperture (NA) optics. Such optics open up the opportunity for more uniform excitation (in

the direction of laser beam propagation) using high Rabi frequencies than is possible in conventional cells, as the thickness of our vapour layer can be less than the Rayleigh range of the tightly focused beam. For example, using a lens with NA = 0.7 (as will be used later in this thesis), Rabi frequencies of the order of gigahertz are achievable on the rubidium D2 transition, even for modest laser powers of order milliwatts. High NA optics also allow for localised interrogation of atoms confined to nano-scale structures. Thirdly, all the sides of the cell are optically polished, allowing for numerous possible input beam geometries (e.g. enabling total internal reflection fluorescence (TIRF) spectroscopy [1]). Fourthly, heating is integrated directly in the finished nano-cell through a compact indium-tin-oxide (ITO) patch, deposited onto external surfaces during cell manufacture (the deposition and operation of such heaters will be described in detail in section 3.4). Finally, it is worthy of note that the narrower 4 mm thick stem of the Armenian cells makes them much more fragile and prone to accidental breakage. Many of the benefits of our Durham-MPL nano-cells are demonstrated in [1], and will be put to use throughout this thesis. Some will be discussed further in this chapter.

Further enhancements to our base nano-cell design have been developed during the course of this work, and these are outlined in the following sections. Development towards smaller structures and confinement in more than two spatial dimensions will be demonstrated through the addition of nano-pocket arrays to our cells, with the long-term goal of studying thermal vapour nano-cell integrated photonic structures. We also detail more incremental advancements to the integrated heating of the cells, cell geometry and design, and the reduction of the overall experimental footprint.

We note that, as discussed previously, throughout this thesis nano-cells filled with rubidium vapour (at natural isotopic abundance) will be used. However, the cell fabrication discussed in this chapter is generally applicable to cells which could be filled with other alkali-metals (in fact we have filled some cells fabricated in the same way with caesium for future works). We also note that we do not add buffer gas to our cells. Buffer gas and other contaminants can cause shifts and broadening of the atomic spectra which are undesirable in some applications [112].

3.2 Etch quality and surface roughness

The patterning of micro- and nano-scale regions and structures within our cells is achieved through a combination of reactive ion etching and laser lithography. Exploiting the fact that the finished nano-cell acts as a low-finesse Fabry-Perot etalon, white light measurements have been used previously to characterise the variation of the confinement thickness on lengthscales of order 100 µm [1]. The resolution of this method was limited by the 100 µm spot size that was used, and thus only provides thickness measurements averaged over this extent. Some applications, for example measurements of the atom-surface interaction, likely require very smooth surfaces. Thus an understanding of surface roughness is desirable. In any case, it is useful to quantify the roughness of the etched surfaces, both to verify sufficient optical quality and to provide potentially useful insight for experiments involving atoms adsorbed to surfaces (e.g. light induced atomic desorption, as will be discussed later in chapter 4).

As such, we have used atomic force microscopy (AFM) to characterise the roughness of our etched substrates. An example is shown in Fig. 3.3, where AFM has been used to characterise a 5 µm square of a surface which was etched to a depth of 500 nm. The achieved RMS roughness, whilst not as exceptional as is provided by the super-polish method [109], is of good optical quality. The Gaussian distribution of points about the mean surface height plotted in (c) demonstrates that the surface is free from any significant variations (which may not be evident when simply quoting the RMS roughness). The figure also shows that defects of order 10 nm in extent may remain after etching. For the work in this thesis, we believe these do not cause significant issues. However, large enough defects can in principle be observed and avoided using high NA optics to image the cell and choose a 'clean' region to experiment in (hence the usefulness of etching multiple copies of each desired structure, as illustrated later in Fig. 3.4). They could also be removed by further etching or smoothing steps after the main etch. The surface quality may vary between etching runs, and as such it is important to characterise surfaces after etching in the way we have described in this section.

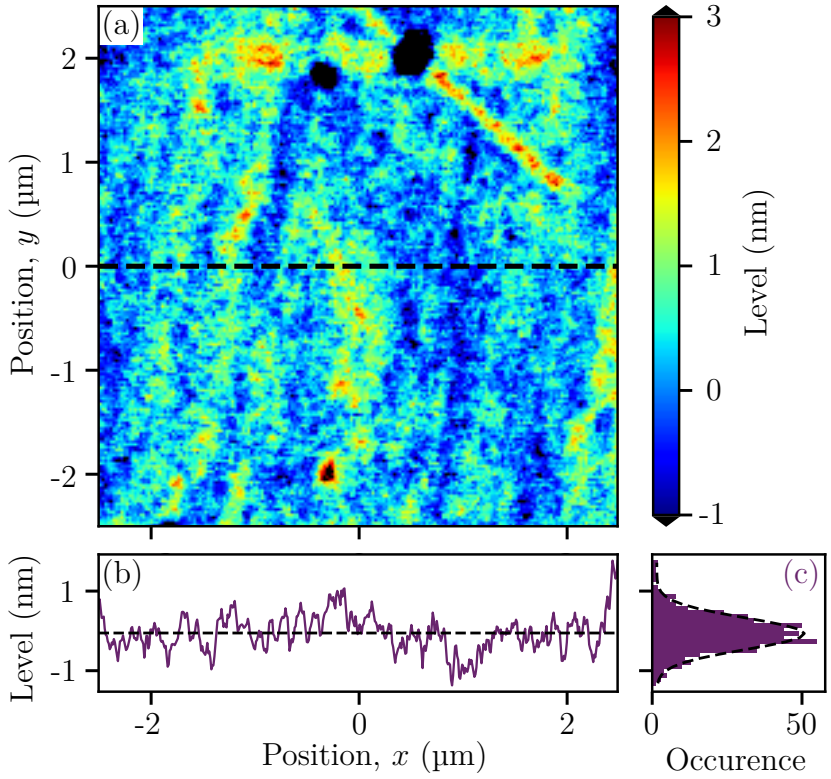

Figure 3.3: **(a)** Surface profile map produced using AFM showing the surface roughness of a fused silica substrate etched to a depth of 500 nm. This surface was prepared in the same way as the nano-cells used in this work. The measurement was performed on the etched front panel before any further cell manufacturing steps been performed. The RMS roughness for this sample was 0.7 nm. If the defect at the top of the image is excluded then this becomes 0.6 nm. For comparison, an un-etched surface of the same fused silica used (not shown) gave an RMS roughness of 0.43 nm. Note that the level 0 nm was chosen to be the average level across the surface map. **(b)** A horizontal cut showing the surface profile along the dashed line shown in (a). The average height is indicated (black dashed). **(c)** The distribution of points from (b) relative to the average surface height, with a Gaussian fit (black dashed).

3.3 Nano-pocket arrays

The collective behaviour of atomic systems has long been an area of much research interest [30, 113]. It has been theoretically shown that 1D chains of atoms and ordered 2D arrays will exhibit novel collective behaviours [87, 114], whilst some special cases with broken symmetries such as Kagome and Lieb lattices have been shown to enhance the collective response further [30, 86]. There has been some progress in the cold atom community towards observing

such effects [44,115]. Even in disordered systems, it has been shown that interesting collective behaviour can occur in certain density regimes [2,36,116,117]. Indeed, experimental studies have investigated one such collective effect - the cooperative Lamb shift - in a nano-cell previously [29]. We propose further development of the nano-cell platform towards an alternative approach to the observation of collective effects in semi-ordered systems. In this section we will outline the tests done towards patterning nano-scale 'pockets' or 'holes' into our vapour nano-cells, which thus pattern the distribution of the thermal atomic vapour within. Through this methodology we achieve an analogue to an array of atoms in a much simpler and cheaper experimental system than with cold atoms, with the caveat that motional effects will need to be accounted for.

To this end we have produced patterned substrates with numerous etched structures. A large section of one such patterned substrate is shown in Fig. 3.4(a), demonstrating the breadth of our design capability. A variety of channel structures (which will be probed later in this thesis in chapters 5 and 6) are shown in more detail in (b) (with design details (c) and (d)). The regular arrays of nano-pockets which we will focus on in this section are shown in (e)–(h). These holes were etched in a similar way to the channel structures described in [1]. We began by patterning a 300 nm ZEP 520a resist layer using a 100 keV electron beam, and then transferred the pattern to a 50 nm Cr layer by a chlorine-based reactive ion etch. We then used this Cr layer as a hard mask for a CHF_3-based etch to produce the final structures shown. As it was unclear what (if any) lattice site sizes and spacings would be optimal for such experiments, as well as to test the versatility of the etching process, a wide variety of combinations were etched into a single nano-cell design. We etched both conventional lattices (square, triangular) and their broken-symmetry counterparts (Lieb, Kagome), in the hope that comparison between atomic response in these two cases will verify the kinds of differences that have been theoretically predicted for periodic atomic arrays.

We found that holes with diameters down to less the 200 nm, lattice spacings of less than 200 nm, and depths of over 1.1 µm were readily achievable with our etching process. Examples of such holes are shown in more detail in Fig. 3.5(a), with their cross-sections shown in (b). The cross-sections are not uniform, which is thought to be due to a combination of mask erosion, material redeposition, and reactive ion depletion. For wider hole diameters

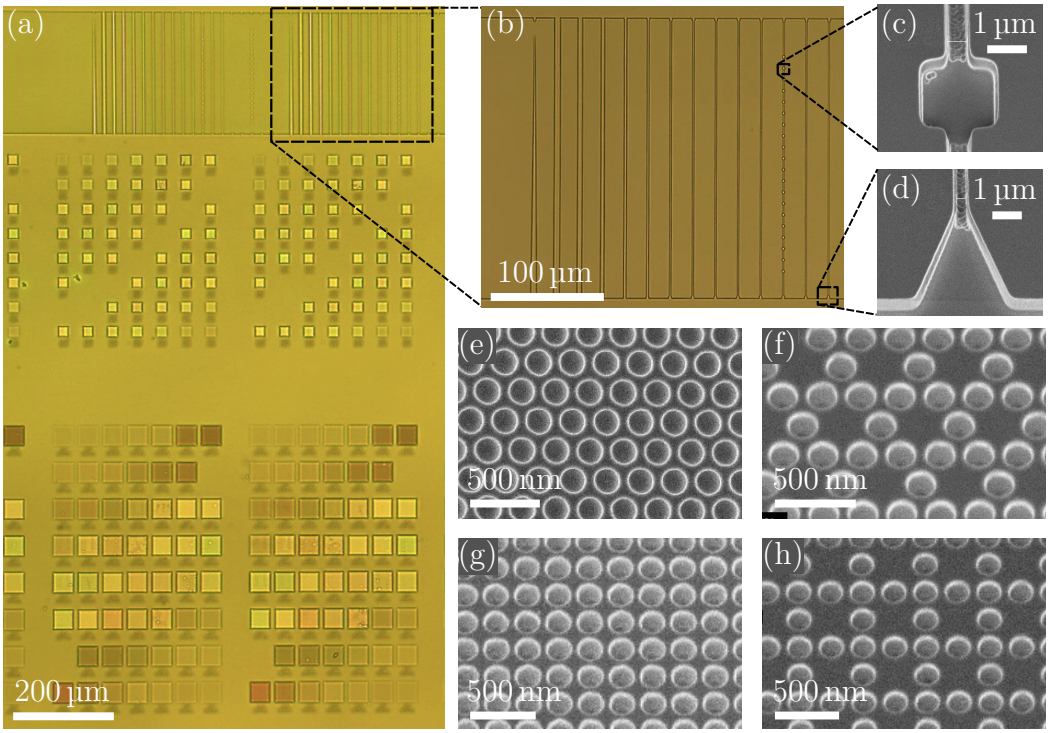

Figure 3.4: Series of images illustrating the variety of possible confinement regimes achievable in our nano-cells. **(a)** The macroscopic structure of part of the patterned region of our nano-cell. Here we see many different patterned confinement regions. At the top are nano-channels of widths 5 µm–400 nm. Repeated copies of these channels were etched to different depths, ranging from 250 nm to 2 µm, to give a variety of cross-sections. The channels are shown in more detail in **(b)**. This image shows the more complex confinement geometries it is possible to pattern, such as tapered channels (far left) or channels with nano-pockets along their length. One such pocket is shown in more detail in **(c)**. Narrower channels were also etched with a triangular entrance aperture, as shown in **(d)**. Below the channel regions in (a), we see arrays of square regions. These were etched on top of a thin '2D' region etched beforehand, such that atoms can enter and leave these sites from above. Each square contains a lattice of holes or 'nano-pockets', with varying size and lattice spacing. Examples are shown, with **(e)** triangular; **(f)** Kagome; **(g)** square; and **(h)** Lieb lattices. Note that the white scale bar in each of (e-h) denotes 500 nm.

we achieved even deeper etches than the 730 nm shown here. That we can pattern these small and regular structures on sub-wavelength lengthscales with such precision and integrate them into vapour cells is already a considerable achievement, and development and testing of these methodologies is a step towards producing versatile devices with many integrated optical ele-

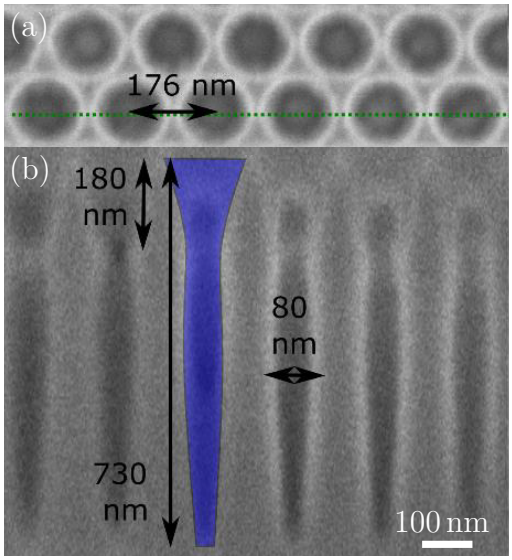

Figure 3.5: **(a)** SEM image of etched circular holes with 176 nm lattice spacing, in a triangular array. **(b)** Focused ion beam (FIB) cross section image showing side profile of holes (taken of a slice through the sample, along the green dashed line in (a)) showing their depth and variation in width. Before FIB imaging, carbon was deposited to avoid damage to the sample. A single hole is indicated in blue.

ments and confinement regions. Complex photonic crystal structures could in principle be patterned into our nano-cells, and thus atom-light interactions studied in their vicinity.

3.4 Cell heating and control of rubidium distribution

For our nano-cell platform to be a good candidate for use in atom-based devices, a good understanding and control of experimental parameters must be demonstrated. Of key importance in experiments with thermal vapours is the number density of atoms in the vapour phase. Generally, the vapour cell temperature is varied to achieve changes in vapour density, with rubidium giving favourable density changes of approximately an order of magnitude with every 20 °C change in temperature (see Fig. 1.1).

To this end, our nano-cells can be heated to achieve the same levels of variation achievable in bulk vapour cells (limited only by the temperature at which the rubidium begins reacting with the fused silica cell walls, at

around 200 °C). However, the kind of bulky ovens often used to heat vapour cells add considerable experimental footprint and block optical access significantly. This is not ideal for versatility or miniaturised devices, so we have implemented an alternative compact solution. Our cells have a square ITO layer deposited on the outer surface, which is used as a compact resistive heater. As ITO has a good transparency at our wavelengths of interest ($> 80\%$ at 780 nm [118]), this does not compromise our optical access significantly.

Generally, a 15 mm square patch of ITO was deposited onto the back surface of the cell block (to the right on the schematic shown in Fig. 3.2(a)), to a thickness of 400 nm. This deposition was done by sputtering using an Ar plasma, and annealed in air at 450 °C. The ITO was contacted on two sides by rectangular 15 mm × 4 mm regions made up of a Ti adhesion layer and an Au layer, which act as electrical contact pads. These are necessary to distribute current across the whole ITO layer. An example finished cell is with ITO and contact pads is shown later in Fig. 3.9, where the resulting integrated heater had a resistance of the order 50 Ω. Applying an electrical current across the contacts causes the ITO to dissipate power as heat, and the glass body of the cell (and thus also the nano-region) reaches an equilibrium steady-state temperature over a timescale of the order of minutes. Our chosen layer resistance gives a power dissipation which allows temperature regimes of interest ($20 - 200$ °C) to be readily achievable using standard laboratory power supply units. Our heater was tested experimentally to work at cell temperatures of at least 200 °C. Our tests were done with 10.5 mm thick cells, but as discussed later in section 3.7, thinner cells are achievable with our manufacturing process, which would speed up the equalibriation of the heating process. A further benefit of our heating solution is that the ITO could in future be near-arbitrarily patterned during deposition, which could prove useful for applications requiring non-uniform heating or optical access not impeded by the ITO layer at all.

We have two methods of applying a current to the ITO layer. Firstly, two wires can be simply connected to the contact pads using conductive silver epoxy. This is the least compromising solution in terms of optical access and experimental footprint, adding only a few millimetres to the overall size, and not enclosing any of the cell. However, we find silver epoxy is not a reliable long-term solution, as over many heat cycles (tested from room temperature

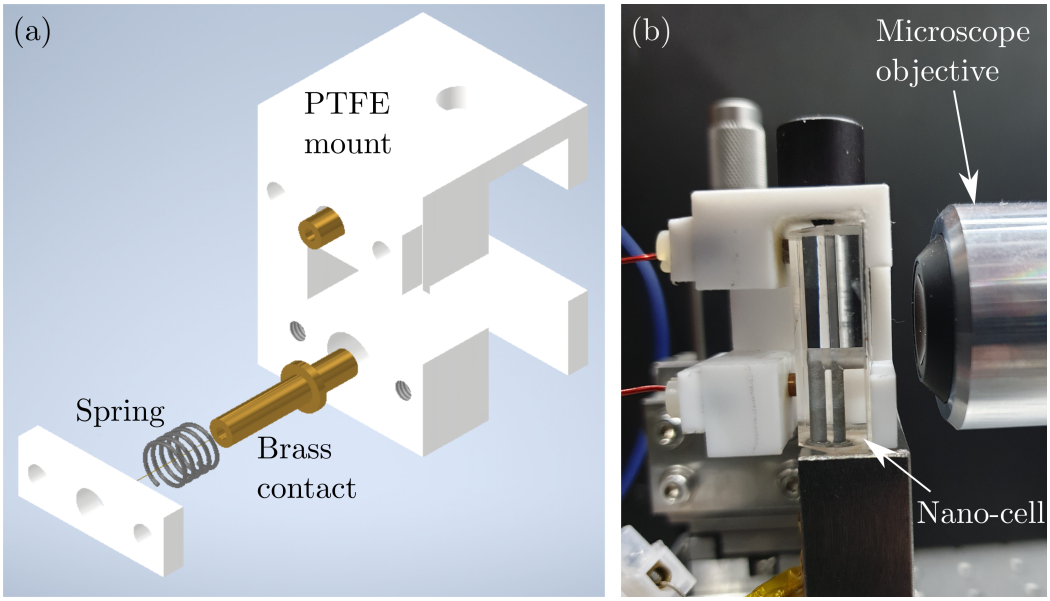

Figure 3.6: Images illustrating the 'press-contact' method of applying current to the ITO layer used for resistive heating of the nano-cell. **(a)** Exploded drawing from Autodesk Inventor, showing the PTFE mount, with brass pins and springs to hold them firmly against the cell. The outer PTFE plate was screwed to the mount to hold the sprung brass pin in place, and a wire was soldered onto the end of the brass pin. This solder is far enough from the heated cell so as to not be impacted by the heat. **(b)** Photograph of the mount in operation around a nano-cell, with features of interest labelled.

to 180 °C) the epoxy degrades and eventually becomes detached. We suspect that this arises due to mismatched thermal expansion coefficients of the different materials making up the contact, and would likely be much less of an issue for continuous operation at a single temperature rather than heat-cycling. An alternative solution developed during the course of this work is a mount with spring-loaded metal contacts, which press against the contact pads on the nano-cell. A schematic of the mount and a photograph of it in operation are shown in Fig. 3.6. The mount is made of PTFE (due to its high melting point and non-conductive nature), which sits a few millimetres thick around the cell. This press-contact solution does not suffer from degradation of contacts over time, and has demonstrated reliable operation under temperature cycling and for cell temperatures up to 200 °C. Experimental footprint and optical access are more compromised using this method than epoxied wire contacts, though less than a conventional cell oven.

The cell reservoir (which is the 'stem' below the cell body, shown at the

bottom of the images in Fig. 3.1) is generally also heated under normal experimental operation. This heating can be integrated in the same way as the cell block heater, through a sputtered patch of ITO with contact pads. However, as experiments are not performed in the reservoir region, optical access is not required. As well as this, the reservoir is generally kept cooler than the cell block. Thus a range of other compact heating solutions can also be used, for example commercially available flexible polyimide foil heaters. Care must be taken to maintain a temperature gradient between the nano-regions and the reservoir, for reasons which will be described in section 3.5. Even temperature gradients within the reservoir itself can change the rubidium distribution (for example, whether surface deposits reside in the base of the reservoir or in the conduit close to the nano-regions), which may itself impact the rubidium density in the nano-regions.

Whilst bulk heating of vapour cells is often the easiest method of controlling vapour number density to implement, other more fast and localised methods have been suggested. Notably, light-activated dispensers [119], gold nanoparticles [120], and light induced atomic desorption (LIAD) [121,122]. In fact, we will present a study of the LIAD effect in our nano-cells in chapter 4. We will also present investigations into the feasibility of adding nanoparticles during our cell manufacture process in section 3.6.

3.5 Rubidium depletion and flooding

Another important consideration for micro- and nano-scale vapour confinement is atomic diffusion timescales and the depletion of rubidium vapour from the confined regions over time. Depletion is not generally a problem in experiments with bulk vapour cells, where the cell and reservoir are heated to the same temperature and the whole system is in a steady state equilibrium between vapour-phase atoms and atoms adsorbed onto the cell walls. However, for the case of our nano-cell, the reservoir is generally kept approximately 30 °C cooler than the cell block and confined regions. This is to stop the confined regions spontaneously filling with liquid rubidium from the reservoir. This gradient, however, leads to a reduction of vapour number density in the micro- and nano-regions over time, with timescales generally of order weeks to months (believed to be dependent on diffusion timescales and operating temperatures used). As such, for micro- and nano-scale vapour

cells, we believe understanding 'local reservoirs' to be of critical importance.

The interaction of vapour atoms and cell walls have long been of interest [123–125]. There exists an equilibrium between rubidium atoms adsorbed to the cell walls and those in the vapour phase, and due to diffusion timescales we believe these surface deposits to have significant influence on the local vapour density in the micro- and nano-regions. Rather than a global equilibrium, we believe that there is a local equilibrium in a given location of the cell between the vapour and the adsorbed atoms on the nearby walls. We observe depletion of vapour phase atoms and surface deposits from our nano-regions over time, the latter of which is shown in Fig. 3.7. We therefore find it important to periodically 'flood' the confined regions with liquid rubidium, which we achieve by making the reservoir much hotter than the confined regions. The exact temperature gradient choice alters the timescale of the process, but to flood the cell over a period of minutes to hours we found that temperature differences of at least 50–100 °C were required.

Once flooded, we allow the liquid rubidium to deplete from the nano-regions by going back to our conventional temperature gradient, leaving surface deposits behind. When returning to a conventional temperature gradient (for example, nano-regions at 100 °C and reservoir 30 °C lower), we have observed standard timescales of 3-6 hours for a 2 µm thick cell region to evacuate sufficiently for experiments to be performed. However, timescales of up to 30 hours have been observed for the same process, suggesting there is more to be understood about its exact dynamics. Furthermore, the more confined regions have been observed to have longer evacuation times: a 500 nm region is some hours slower than the 2 µm region, whilst channel structures (even those of a few microns width) patterned within our cells take longer to evacuate than even the 500 nm 'slab' region. The narrowest of channels (down to 400 nm × 500 nm in size) have been observed to take a number of days of heating to evacuate visibly and sufficiently to perform experiments.

After the flooding process, the density of the atoms on the cell walls is replenished, and macroscopic deposits (each on lengthscales of order microns or tens of microns) are observed. This is illustrated in Fig. 3.7(a). Experiments can be performed on vapour in the clear regions in the vicinity of the deposits, and it is even possible to partially flood the cell and then perform experiments in the clear regions close to a visible condensed area of rubidium. Aggregates were observed to diffuse over time whilst the cell was being heated,

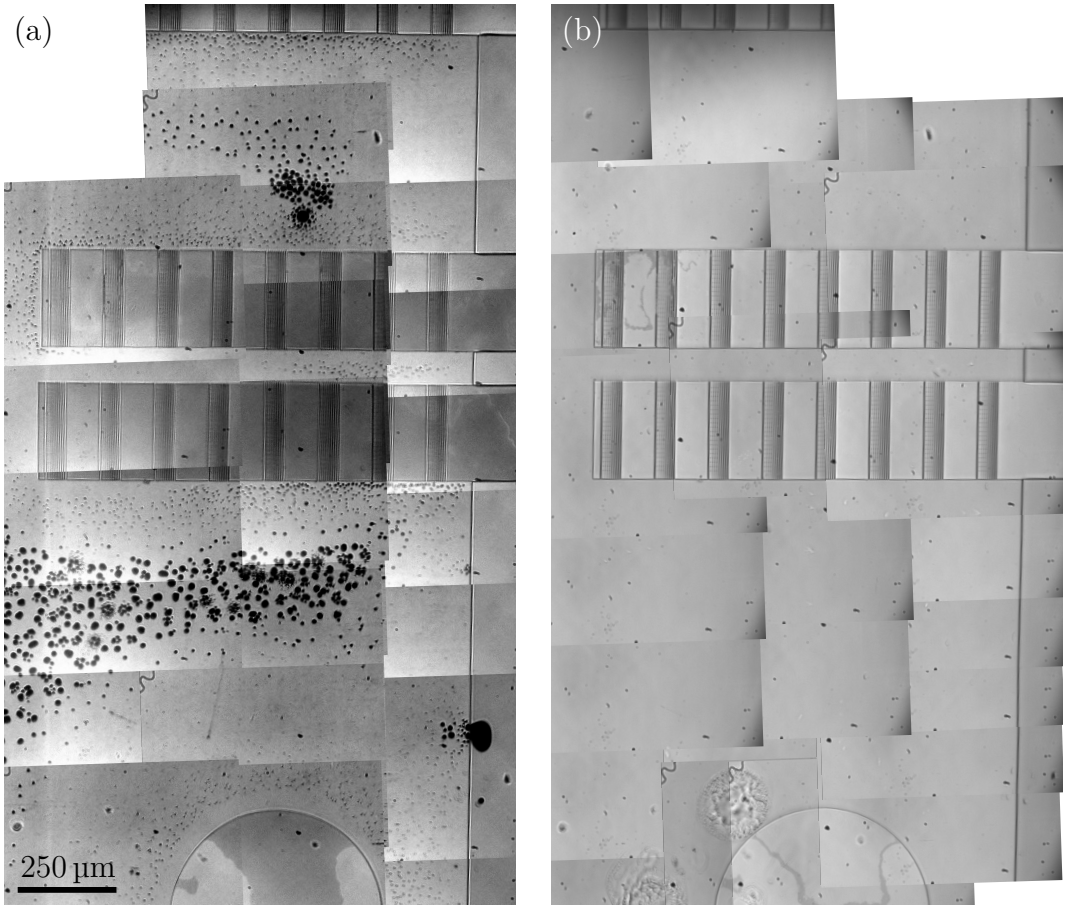

Figure 3.7: Composite white-backlit images showing the same 2 µm thickness region of the nano-cell at different times since flooding. The circle at the bottom is a 'spacer' - a pillar added to the design to reduce bowing during fabrication. The linear features in the top half of the images are sets of vapour channels of varying widths (400 nm – 5 µm). The line to the right of the image is the boundary between this 2 µm region and an adjacent 1 µm region. Image **(a)** was recorded after the regions were filled with liquid rubidium and then heated to 100 °C (to allow some of the rubidium surface coating to diffuse) for a few hours. Image **(b)** was recorded 21 days after (a), with the cell in operation (heated to approx. 100 °C) five days per week. There is a clear change in surface distribution between (a) and (b). Note that dust on the camera and optics causes the repeated dark features especially obvious in (b), and non-uniform illumination duplicated across each image causes the brightness gradients seen.

as illustrated by comparison between the two images in Fig. 3.7, where image (b) was taken 21 operational days after image (a). As such, we infer that thinner surface rubidium coatings (which are not directly observable through this white-backlight method) also likely diffuse in a similar manner. Under-

standing this surface coating depletion and replenishment effect may play a useful role in LIAD studies, which will be discussed further in chapter 4. As our cells facilitate high-NA imaging, it is even possible to record and observe the aggregation and diffusion of the rubidium deposits in real time, which may be useful for further understanding the processes.

As an illustrative experiment, we measured the fluorescence activity from a 1 µm region of one of our cells before and after flooding. This was done through resonant laser excitation at 780 nm in a TIRF scheme, with a power of 100 µW and a cell temperature of 100 °C. The history of this cell was as follows: the cell was heated once to 200 °C after manufacture for approximately one hour (for testing purposes), and after this initial testing the cell was then left for approximately one year unheated. The cell had never been flooded until this experiment. We found that the fluorescence activity on resonance after flooding was 10^5 times higher than before flooding. This is a considerable and somewhat unexpected increase, suggesting that diffusion timescales and surface distribution of rubidium are incredibly important to the density of atoms in the vapour phase. Despite the numerous studies using thin cells in recent years (referenced throughout this work), the number density of atoms within such cells and how this is related to surface reservoirs and diffusion behaviour has not, to the author's knowledge, been previously studied in any detail. It is possible that surface wetting and curing and diffusion of rubidium into the bulk of the fused silica plays a role in modifying the vapour density distribution (alongside the atomic diffusion timescales and temperature gradients).

3.6 Nanoparticles and internal surface coatings

As discussed in section 3.4, the atomic number density is an important parameter in vapour cell experiments. One proposed method for fast and localised control of atomic number density is based on the use of nanoparticles of e.g. gold or platinum. These particles can be heated using light, which causes condensed rubidium on their surfaces to desorb and enter the vapour phase. This process was demonstrated for gold nanoparticles in [120], whereby the effect was used to induce an approximately 16× increase in vapour density

over less than 20 ms. Thus these particles can act as fast and localised sources of vapour atoms. As well as this, interfacing atomic vapours with integrated plasmonic structures has been suggested as a candidate for all-optical devices and scalable logic gates [14]. Given the promising nature of such techniques, we have investigated the feasibility of including gold nanoparticles in our nano-cells, the results of which are detailed below. These results are another illustration of the versatility of our manufacturing methods, showing the promise of nano-cells as candidates for atom-based devices. It is possible that the small extent of these particles combined with our high-NA capabilities could facilitate localised vapour density control, whilst larger regular arrays of these particles could be used to stimulate a patterned vapour density variation across the cell.

We tested both platinum and gold as candidates for nanoparticles to be deposited in our thin cells, and the methodology by which these nanoparticles were deposited is as follows. The glass slide was etched in our conventional way to produce micro- and nano-regions, as described in [1]. After the etching process, a positive electron beam (e-beam) resist (200 nm ZEP520A) was added on top of the fused silica. A water solvable electrical discharge layer (AR 5090.02) was also applied in order to avoid charging during e-beam exposure. Samples were then coated with 3 nm Ti, and 60 nm of gold or platinum to achieve the required structures. Disks between 300 nm and 500 nm, as well as larger continuous metallic areas, were patterned in this way. The sample was then tempered at 900 °C for 6 hours, to simulate the bonding process which would usually be undertaken during cell manufacture. The results of this testing using gold are summarised in Fig. 3.8. We observed that after heating, the disks remained in their well-defined positions, as shown. However, any larger continuous layer regions became mobile and formed islands during the heating process. The same behaviour was observed with platinum disks and layer regions. We thus conclude that both platinum and gold disks of the sizes tested could be placed into our cells during the manufacturing process and survive the subsequent heating and filling stages of manufacture. Further testing needs to be done using these particles in a finished cell to quantify the vapour density control potential that their integration can bring.

In the same testing run as for the nanoparticles, an inner surface coating for our cells was also tested. As discussed in the introduction to this chapter, Armenian nano-cells constructed with sapphire windows could be heated to

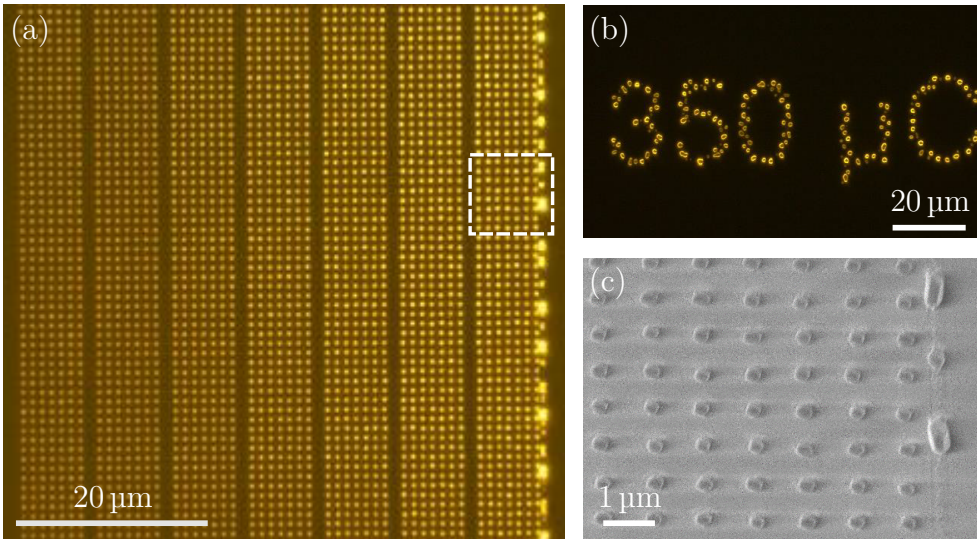

Figure 3.8: Images showing gold nanoparticles and structures that have been deposited onto a fused silica surface and baked for 6 h at 900 °C. **(a)** Microscopy image of a region containing gold disks of various sizes, arranged in seven columns and ranging in diameter from 290 nm (leftmost column) to 495 nm (rightmost column). The far right vertical line was patterned as a continuous layer of gold, but after baking this had migrated into larger particles as is shown. The dashed square is the region shown in more detail in (c). **(b)** Microscopy image of "350 µC", which was patterned as continuous lines on the cell, but (in the same way as the line in (a)) became mobile and formed islands during heating. **(c)** SEM image at 45° showing the region marked in (a), showing both nanoparticles and the continuous line (far right) which has migrated and formed larger particles.

much higher temperatures than our fused silica cells without the alkali metal atoms reacting with the cell surfaces. As such, adding an inner sapphire coating to our cells may allow for similar versatility. Furthermore, it has been suggested that there exists a repulsive van der Waals interaction for the Cs $6D_{3/2}$ state with sapphire surfaces [39, 43], through virtual emission at 12.15 µm which lies within the resonant polariton modes of sapphire. Thus, we tested the feasibility of adding aluminium oxide (AlOx, also referred to as sapphire) coatings to the internal surfaces of our cells. In addition to the nanoparticles as described above, a 25 nm AlOx layer was added to both the etched surface and the un-etched glass surface, such that when bonded both the front and back internal surfaces of the cell would be AlOx coated. This coating survived the deposition and heating process (900 °C for 6 hours), and thus we have demonstrated that this is also a feasible addition to future cells

made using our methodology.

3.7 Cell dimensions and window design

As demonstrated in [1,82], the versatility of optical access is an important and useful aspect of our cell design, for example for allowing the beam geometry required for the TIRF excitation scheme. However, for TIRF measurements at certain angles, in past experiments it became necessary to use a prism contacted to the side of the cell with index-matching oil. This adds to experimental complexity and bulkiness, and so an alternative solution was sought. In Fig. 3.9(a), we illustrate a revised cell design, whereby the back corners of the cell are chamfered at close to 45°, to allow for better optical access for TIRF incident angles of interest. This demonstrates the customisability of our cell design, and this cell is now in regular use for TIRF experiments.

The size of the whole cell is also a consideration for possible technological applications. The thickness of the glass block had not been a significant consideration in previous designs, aside from simplicity of manufacture, robustness, and ease of mounting. Thus our cells had previously been thicker overall than, for example, Armenian nano-cells (as can be seen in Fig. 3.1). However, during the course of this study, we tested an alternative cell design with a much thinner footprint. The glass block which forms the back part of the cell was reduced from 10 mm thick down to 4 mm, which also required a thinner elliptical reservoir connection. The finished glass block with reservoir inlet is shown in Fig. 3.9(b). In principle an even thinner block is possible, limited only by reservoir aperture milling and robustness. This could open up the option of high-NA optical access to the nano-regions at both the front and back faces of the cell.

Both of the design features described above optimise our nano-cell platform for different issues and experiments. In the future it may be that different variations on our nano-cell design will be needed for different applications, and here we have illustrated that this is readily achievable for two specific issues we encountered during this work.

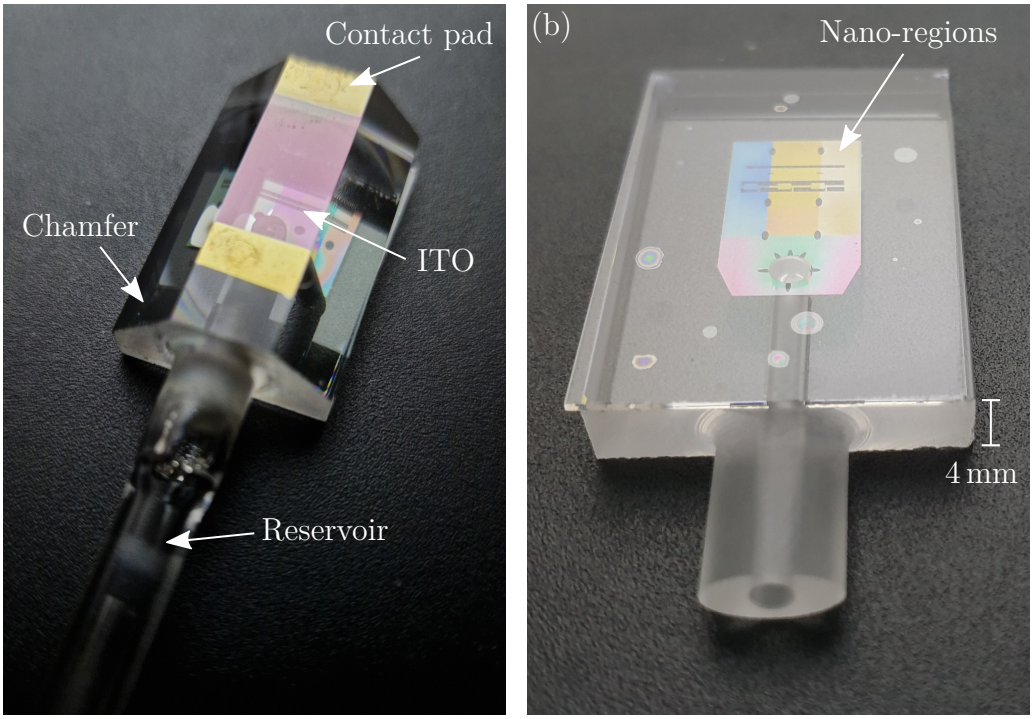

Figure 3.9: Photographs showing two nano-cell body design variants, under white light illumination. Various cell features are labelled on both images. **(a)** Back view of a cell with chamfered back corners, to allow for better optical access in the TIRF geometry. The chamfers, as for all sides, are optically polished. The two gold contact pads and the ITO region between them are clearly visible on the back face. **(b)** Front view of a cell with a 4 mm thick body, making for a total cell thickness of 4.5 mm including the etched front slide. This cell features an elliptical conduit onto which the reservoir was subsequently connected. The nano-regions are clearly visible, whilst the various coloured spots in the otherwise clear glass outside of this indicate unbonded regions (e.g. due to dust particles inhibiting bonding).

3.8 Conclusion

In this chapter, we have demonstrated the design capabilities of our current generation nano-cells, and investigated the limits of our manufacturing methods. During this work, we have developed new cells with confinement in the 'slab' geometry down to 250 nm, and 'channels' and 'pockets' down to less than 200 nm across - considerably smaller than previous iterations of our nano-cell design (whose smallest features were 500 nm). We have also characterised our cell features through quantifying the surface roughness of our etched surfaces for the first time. Furthermore, we have demonstrated de-

position of nanoparticles and surface coatings into our cells, which have been shown to survive the manufacturing process. The versatility and customisability of our nano-cell platform, demonstrated by the innovation presented in this chapter, provides huge potential for further additions and improvements.

We have tested the possibility of the integration of metallic nanoparticles into our nano-cell platform, and concluded that gold and platinum disks with diameters as low as 300 nm and thicknesses of 60 nm can be patterned into our nano-cells and survive cell manufacturing conditions. In terms of structuring, we have now demonstrated various features including channels, pockets, and metallic disks, which could all act to pattern the distribution of vapour within our cells. Further work is needed to identify the most interesting lengthscales and geometries for such patterning, but this development paves the way towards the creation of thermal vapour atomic metamaterials, whose properties and optical response are modified by the patterning of the vapour distribution by our cells. This could open up the study of novel physical systems in the thermal vapour regime.

We have also shown in this chapter that it is possible to reduce overall cell thickness from 10.5 mm to 4.5 mm, and that there is a viable compact heating solution for our cell in the form of ITO coating. These are first steps towards optimising our platform for applications involving miniaturised, scalable, and portable atom-based devices.

Overall, we have demonstrated the versatility and customisability of our nano-cells as a platform for fundamental physics studies and potential technological applications. As has already been demonstrated in this chapter, we envisage that further improvements and changes will be targeted to specific applications, and that the evolution of the platform will be in further diversification towards bespoke cells for specific purposes. It will also be interesting to continue to push the manufacturing limits in terms of etched and deposited structure sizes, surface roughness, and overall experimental footprint.

Chapter 4

Light induced atomic desorption and condensation on the micron scale

For experiments with thermal vapours, a key control parameter is atomic number density. Traditionally this is controlled through cell temperature, which can be related to the vapour pressure inside a standard vapour cell in a well understood manner [38]. However, this control is slow (requiring timescales of order minutes to hours for thermal equilibriation) and also not localised. Temperature-based control also has limitations, for example at higher temperatures alkali metals can react with cell substrates such as fused silica. Whilst there has been some effort to manufacture vapour cells which can withstand very high temperature operation (e.g. using other materials such as sapphire), this can prove difficult [35] and such cells often have short operating lifetimes of the order of only hours or days. Furthermore other desirable features, such as antirelaxation coatings, generally do not withstand high temperature operation [126].

It has been suggested the conventional relationship between density and temperature does not hold in systems with nano-scale confinement geometries [1] (due, for example, to atomic diffusion timescales). This is alongside the fact that miniaturisation of vapour cells has the consequence of reducing the optical path length, requiring ever higher temperatures to produce optical depths necessary for spectroscopy experiments. One proposed solution to the problem of low number density involves using light to heat nanoparticles de-

posited within a coated vapour cell [127], and in fact initial steps towards testing deposition of nanoparticles in our nano-cells are discussed in section 3.6. This achieves the desired localisation, but adds additional complexity to the cell manufacturing process. In this chapter we detail an alternative solution for vapour density control in our nano-cells, using light to liberate atoms from the fused silica cell surfaces.

4.1 Introduction

The method of light induced atomic desorption (LIAD), by comparison to conventional heating, has the potential to yield both much faster and much more localised atomic density control. The LIAD process was first reported in the 1990s [128, 129], and involves the use of non-resonant light to liberate adsorbed atoms from surfaces. It has been well documented for use in a wide range of applications: from improving the loading efficiency of magneto-optical traps [130, 131] - where it has helped enable compact portable applications [132] - to the creation of high optical depths in thermal vapour systems [133, 134]. Some empirical rate-equation modelling of LIAD dynamics has been done based on experiments in these various regimes [135–137], whilst other studies have shed light on the photon energy and power dependence of the LIAD effect [138]. Measurements have shown that LIAD is non-thermal and it is considered to be single-photon in origin [139], however there is much work still to be done to characterise the process and its underlying mechanisms. It has been suggested that the exact temporal dynamics of the LIAD process may depend on surface defects, impurities, and the preparation method of surfaces (and even that the LIAD response could be used to characterise surfaces) [140]. Studies have begun to shed light on the applicability of the effect with different materials, including porous glass [141], porous alumina [142], pyrex and quartz [143], and sapphire [139], as well as surfaces with coatings including paraffin [144, 145]. The study in reference [144] also documents the LIAD effect for different alkali atoms (Na, K, Rb, Cs), and finds considerable differences in the response for each.

LIAD studies in thermal vapours have in the past generally been confined to conventional centimeter-sized vapour cells, with more recent works having exploited the effect in microfabricated millimeter-sized cells [122] and in micron-scale hollowcore fibres [121]. The former study also shows how the

effect can have technological applications, by demonstrating its use both as part of an optical isolator setup and a laser locking setup. In more confined regimes such as micrometre-sized cells, the LIAD effect should give a favourable increase in vapour density, owing to the high ratio of wall area to vapour volume. Heating-free all-optical control of number density would have numerous experimental benefits, including fast and localised control for diffusion studies or for remote or compact applications where electrical currents from heaters may be problematic (or heaters may be difficult to incorporate and stabilise). One recent study demonstrated the LIAD effect in micrometre-sized vapour cells [31], and used the resulting transient high vapour density regimes (whereby $n \gg k^3$) to study dipole-dipole interactions through line broadenings and shifts. The only other known LIAD study in micron-scale thermal vapour cells was reported briefly in [82]. That study by Hamlyn used the technique of selective reflection to record the atomic activity dynamics upon subjecting a 1 µm thick cell to nanosecond pulses of 355 nm laser light. Their data has significant noise, and its dynamics are still poorly understood, so we seek to build upon this.

The interaction of atoms and surfaces is also an area of significant interest and ongoing study. The interaction of vapour atoms with cell walls is of great importance in thin cells, where wall collisions are common and a considerable fraction of the vapour atoms reside close to the cell walls at a given time, and thus our studies are intrinsically linked to atom-wall interactions. The impact of the wall distribution of adsorbed rubidium has already been discussed in section 3.4, whereby it was suggested that the amount of wall-adsorbed rubidium can vary considerably and impact the vapour-phase atomic density. Further parameters of interest include the dwell time of an atom on the cell wall [146], which will also impact the vapour distribution.

Overall, whilst significant efforts have been made to study the LIAD effect in a number of regimes, there are still many open questions about its exact dynamics, underlying mechanisms, regimes of applicability, and reproducibility. In this chapter, we will report on LIAD experiments done using our nano-structured rubidium vapour cell under illumination with non-resonant 450 nm laser light, with view to understanding the process in more detail through measurements of the atomic fluorescence activity dynamics.

As well as LIAD, we will report our observations of another effect found to occur in a similar atom-light interaction regime. This effect induces mac-

roscopic regions of condensed rubidium atoms on the inner surfaces of our nano-cell upon illumination with our 450 nm light. We term this second effect light induced condensation (LICo). To the author's knowledge, similar effects have received little attention in publications to date. A similar effect is presented in [147], whereby it is suggested that radiation can induce dipoles which cause the surface migration of adsorbed particles. It is also discussed in [141,148] that in porous glass light can induce a large decrease in transparency due to LIAD increasing the number of surface Rb nanoparticles. This is because atoms are detached from pore surfaces and recondense on the walls forming clusters. These clusters have considerable absorption plasmon bands in the infrared region. It has also been suggested that different substrates have different aggregation and diffusion dynamics for atoms adsorbed within the walls [143], and the understanding of these processes in various substrates is vital to controlling and harnessing this effect. In this chapter we will study the LICo effect on the microscopic scale within our fused silica thin cells, shedding light on a new regime in which this effect has been observed.

4.2 Methodology

In this work, we used a nano-structured alkali metal vapour cell, constructed in-house using the methodology explained in detail in [1] and further discussed in chapter 3. The cell was constructed of uncoated fused silica, and contained no buffer gas. Confinement regions with thicknesses of 500 nm, 1 µm, and 2 µm were produced during the etching step in the cell manufacturing process. Substrates prepared in this manner have an RMS roughness of order 0.7 nm, as shown in [1].

The basic experimental scheme used for observation of both LIAD and LICo effects is shown in Fig. 4.1, with a more detailed optical layout shown in appendix A.4. To study atoms in the vapour phase, a 780 nm laser beam, frequency-stabilised to be resonant with the ^{85}Rb D2 $5S_{1/2} \rightarrow 5P_{3/2}$ ($F = 3 \rightarrow F' = 4$) transition, was used. This beam was totally-internally reflected from the back face of the vapour region, producing an evanescent field in the nano-region which interacts with the vapour atoms. This methodology, known as total internal reflection fluorescence (TIRF), can be used to record atomic fluorescence activity in a way that is generally dark-field [1]. The fluorescence was collected by an objective lens and recorded using a photon counter. Before

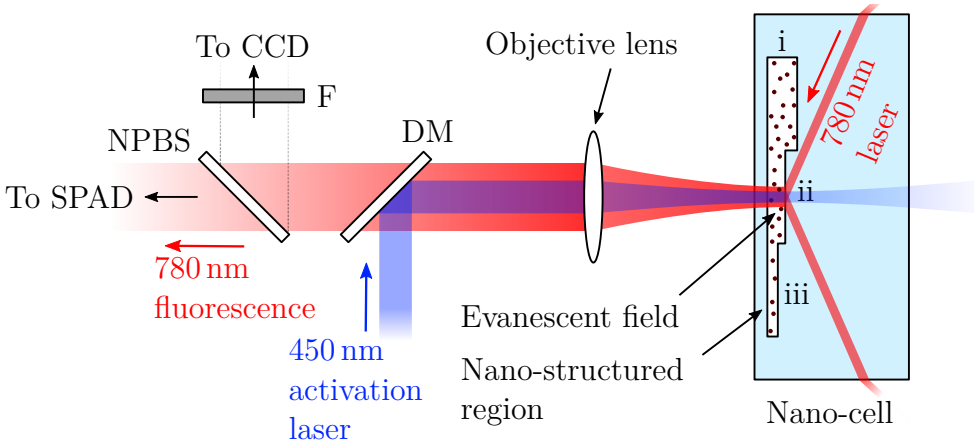

Figure 4.1: Experimental setup (not to scale) used for observing LIAD and LICo in a nano-cell (shown as a top-down schematic). A 780 nm excitation beam was totally-internally reflected at the glass-vapour interface, giving rise to an evanescent field in the vapour region which interacts with the rubidium vapour [1]. The atoms could be excited and subsequently fluoresce, and this light was collected by an objective lens (either a Mitutoyo MY100X-806 $f = 2$ mm plan apochromat microscope objective or a $f = 30$ mm singlet lens). Fluorescence was recorded using a single photon avalanche diode (SPAD). A non-resonant 450 nm activation laser was focused into the nano-structured region with the same objective. The nano-structured region comprised regions with thickness: (i) 2 µm, (ii) 1 µm, and (iii) 500 nm. For alignment and imaging, a broadband backlight was placed behind the cell (to the right on this schematic), such that transmitted light was incident on the CCD. Other components shown are: F - spectral filters; NPBS - non-polarising beamsplitter; DM - dichroic mirror.

experiments were performed, the laser was scanned around resonance to verify that detected light was of atomic origin and thus displayed characteristic resonance line-shapes, rather than being background or scattered laser light.

For both LIAD and LICo, a non-resonant 450 nm 'activation' laser was employed. This laser was an inexpensive Osram Opto PLTB 450B, with a maximum output power of 1.6 W. For our experiments we focused up to 500 mW of this power into our cell using the same objective lens used to collect fluorescence. The switching on of this laser incident on the cell caused the desorption and condensation effects studied in this work. After turning on the 450 nm laser, atomic fluorescence activity was used to study the dynamics of atoms in the vapour phase (i.e. those liberated from the walls by LIAD, as well as in the background vapour), as detailed above. However, for LICo it was atoms condensed onto the cell walls that were of interest. To study

such atoms, a broadband backlight was used to image the cell onto a CCD (after spectral filtering to extinguish any reflected 450 nm light). The areas of condensed rubidium blocked the backlight, creating a darker region. The recorded formation and dissipation dynamics of this region, as well as imaging of the cell beforehand, sets it apart from any other dark defects present within the cell or optical setup.

4.3 Results and discussion

4.3.1 Light induced atomic desorption

We will firstly probe the LIAD response in an incredibly localised manner, by studying the vapour response upon illumination with 450 nm laser light focused to a spot size of order 1 µm. The fluorescence activity dynamics under illumination for approximately 14 s in a 2 µm thickness region of the cell is shown in Fig. 4.2. Increases in the fluorescence activity recorded from the cell upon 450 nm illumination are a clear signature of an increase in vapour-phase atoms and thus LIAD. We observed complex temporal dynamics in the activity profile over the course of the illumination, beginning with a fast (3 ms) increase in activity to 6× the background level. We believe the speed of the increase was limited by the turn on time of our laser light. The considerable increase in vapour density is to be expected, given the favourable ratio of surface area to volume in a thin cell. However, there is a trade-off between this and the wall-to-wall time of flight, meaning that atoms liberated from the walls and travelling at thermal speeds can, on average, only contribute to fluorescence signals for a few nanoseconds before collision. As will be discussed in chapter 6, the excitation and fluorescence dynamics of atoms confined to a thin cell are complex, given that an average atom will not reach the conventional steady state in the short time before it collides with a wall. Thus we expect that the majority of atoms will not fluoresce (the natural lifetime of the state in question is 26 ns, much longer than the mean wall-to-wall time of flight), and so this 6× increase in fluorescence may under-represent the real increase in number of atoms.

Before discussing further dynamics, we will focus on the initial activity peak and study its dependencies. As shown in Fig. 4.3(a), the peak activity of the initial peak activity upon 450 nm illumination increased with increas-

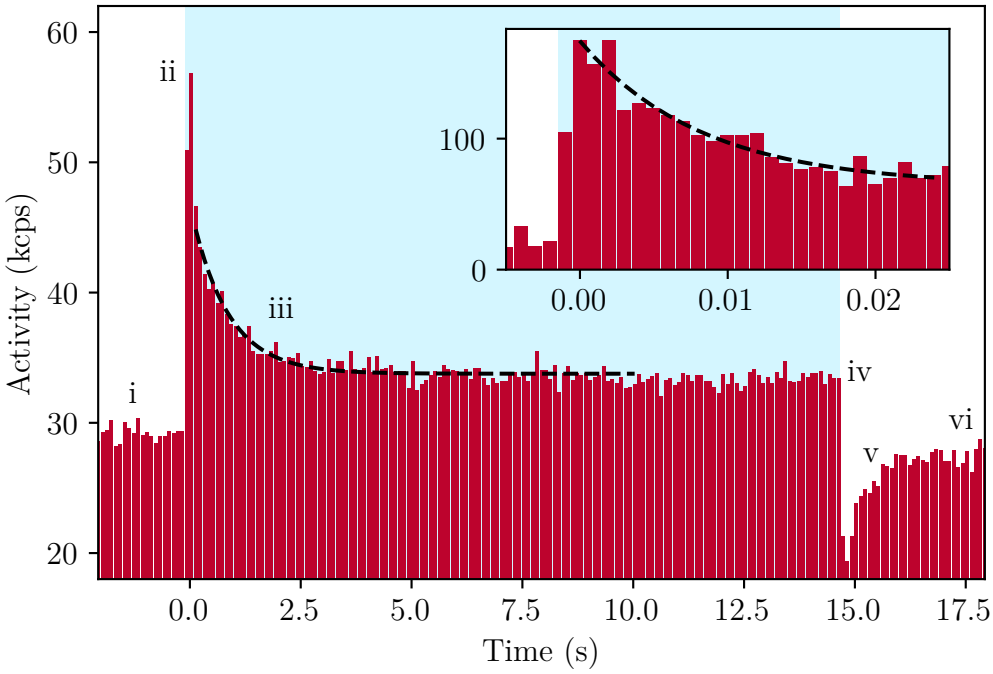

Figure 4.2: Fluorescence activity (red) from a 2 µm thick cell during a typical LIAD measurement sequence. The 780 nm excitation laser had a power of 200 µW and was stabilised on resonance with the rubidium D2 line. The 450 nm laser was focused into the nano-cell with an $f = 2$ mm microscope objective and had a power of 80 mW, and the cell was at a temperature of 100 °C. The experimental sequence was as follows: To begin, the 450 nm laser was off, giving the background atomic fluorescence activity level (i). The 450 nm laser was then switched on (ii), causing an increase in fluorescence activity up to 6× the background level, which occurred over 3 ms. This peak decayed (iii) to a new steady-state fluorescence. When this laser was turned off (iv), we observed a dip in fluorescence down to a factor of 2 lower than the background level. Blue shading indicates the period that the 450 nm laser was on. The dip then returned (v) back to the background level (vi). The decay after the initial peak was empirically fitted with two exponential functions (shown black dashed). A slow decay was fitted to the data with 100 ms bins (main plot) and a fast decay was fitted to the data with 1 ms bins (inset). A double-exponential fit was chosen as it is expected that multiple timescales will be present in the dynamics. Note that, due to the wider bins of the main plot averaging over the narrow peak, the peak activity appears higher in the inset. The fits yielded a fast decay with a 1/e timescale of 8.3(16) ms, and a slow decay with 830(50) ms.

ing 450 nm power in the range 10–500 mW. This appears to be linear after approximately 100 mW, which corroborates previous reports of linear intensity dependence [138]. Below about 100 mW, any activity spike was obscured

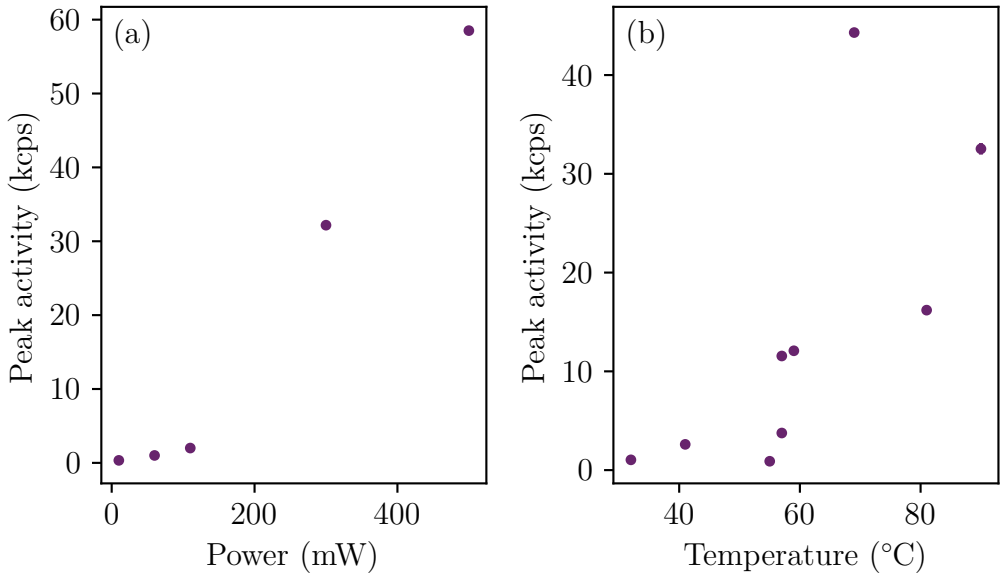

Figure 4.3: **(a)** Dependence of the initial LIAD fluorescence activity peak on the power of the 450 nm laser. Datasets were taken in the same way as in Fig. 4.2, in a 2 µm region of the cell at a temperature of 100 °C, with a 780 nm laser power of 200 µW, and a $f = 30$ mm objective lens to focus the 450 nm light into the cell. **(b)** Dependence of the LIAD fluorescence activity peak on cell temperature. Datasets were taken in the 1 µm region of the cell, with a 780 nm laser power of 800 µW and a 450 nm laser power of 170 mW, focused into the cell with an $f = 30$ mm objective lens. Note that the peak fluorescence activity is taken as the magnitude of the highest activity bin after the LIAD laser is turned on, and errorbars on these peak values (which were calculated from the Poissonian statistics of the photon counts) for both plots are too small to be seen.

by our detection noise. We also found that the peak activity had a temperature dependence, with little response observed below approximately 50 °C, as shown in Fig. 4.3(b). However, this dataset was taken in a 1 µm region of the cell, meaning that it was subject to noise due to LICo (which will be discussed in more detail the following section). This may explain the considerable stochastic variation observed in the datapoints (despite the errorbars on most datapoints being too small to be seen). However, we still consider the qualitative result that the LIAD response increases with temperature to be valid.

Referring back to Fig. 4.2, we observed that the transient peak observed initially decayed to a new higher steady-state fluorescence activity. We believe this is due to the newly shifted equilibrium between the rates of adsorption

onto- and desorption from the cell walls due to LIAD. We empirically fitted the sum of two exponentials to this decay, yielding a fast 8.3(16) ms and a slow 830(50) ms decay. The double-exponential fit was chosen as it is expected that multiple timescales influence the dynamics of the process, including vapour diffusion and adsorbate depletion from the cell walls. After the initial decay the new equilibrium activity was 17% higher than the background fluorescence rate, and we observed that this higher vapour density persisted for at least 10 s under continued 450 nm illumination without decaying appreciably. We postulate that the two decay rates are from two desorption processes, as has been discussed in [121]. In that study, the authors suggest that rubidium on the surfaces can either be in the form of a contiguous metallic layer, or of metallic clusters. It is suggested that the clusters are desorbed efficiently by the LIAD light through plasmon resonances and thus depleted quickly, and can then take hours to re-form. By contrast, the metallic layer is desorbed less efficiently and re-forms almost immediately [149]. Thus the continuous higher vapour density observed whilst the LIAD light is on (between (iii) and (iv) in Fig. 4.2) is likely a consequence of the continuous desorption and re-formation of the metallic layer, whilst the initial spike is the desorption of the clusters. The initial diffusion of vapour-phase atoms from the localised higher density region produced by the LIAD effect will also contribute to the transient dynamics before a new equilibrium is reached. A combination of the desorption of clusters and layer atoms, and vapour diffusion into and out of the region of interest must be considered to fully understand the LIAD dynamics we observe.

Upon ceasing 450 nm illumination, we observed a fluorescence activity dip down to half the background rate, which happened over a 10 ms timeframe. This is likely to have been limited by the turning off time of the 450 nm laser, which was of the order of milliseconds in our setup, but could be improved to hundreds of nanoseconds (e.g. through the addition of an AOM). We then observed a return to the background level with an exponential form, for which fitting yields a 1/e timescale of 520(60) ms. We propose that this is due to the shifting equilibrium between the adsorption and desorption rates of the cell walls between the cases of 450 nm illumination and no illumination. A higher rate of atoms are adsorbed than desorbed transiently due to the imbalance induced during illumination, and thus there is a period where the local density of atoms in the vapour phase dips below the equilibrium density, before

being repopulated by vapour diffusion from the surrounding cell. Finally the system returned to the pre-illumination equilibrium between vapour-phase atom density and wall-adsorbed atom density.

We can calculate a simple order of magnitude estimate for the number of atoms involved in the LIAD response. For this, we will begin with the example dataset in Fig. 4.2. Here the cell was held at a temperature of 100 °C, and the 450 nm laser had a power of 80 mW and was focused to a spot size of approximately 1 µm in a 2 µm thickness region. We collected 780 nm fluorescence light via the same objective lens and into a single-mode fibre to a photon counter. This setup gave a collection volume of approximately 10 μm^3. Using standard vapour pressure calculations, a temperature of 100 °C gives a mean number density of 6 μm^{-3}. This means approximately 60 atoms on average within our collection volume contributed to our background activity of 28 kcps. When the 450 nm laser was turned on, we observed an increase in activity which peaked at 175 kcps, approximately 6× higher. Thus we estimate that 6× the number of atoms contributed to this fluorescence activity, meaning that LIAD caused 300 atoms to contribute this extra fluorescence spike. However, our atoms only survive to be able contribute to fluorescence for on average a few nanoseconds (before leaving the collection volume or colliding with the cell walls), meaning most atoms do not fluoresce, as will be discussed further in chapter 6. Accounting for this gives a rate of liberation during the initial 3 ms spike of approximately $10^6\ s^{-1}$. Accounting for the area upon which the 450 nm laser was incident (including both back and front cell walls) yields a rate of $0.5 \times 10^6\ s^{-1} \mu m^{-2}$. However, this estimate has considerable uncertainty. Most significantly, we believe the vapour-phase number density in our thin cells does not fully obey the steady state vapour pressure solutions (see section 3.5), and thus our initial estimate of the background atom number may be incorrect.

We also note that, whilst LIAD results obtained were reproducible in the same location of the cell with the same experimental parameters, results varied with choice of location in the cell (within the same cell thickness region) and with cell history (e.g. time after flooding), suggesting that underlying distributions of wall-adsorbed atoms influence the effect in a way that we do not yet fully appreciate. For performing experiments, it is advantageous to be able to move around the cell and choose a location with a considerable LIAD response, but more work needs to be done to understand and improve

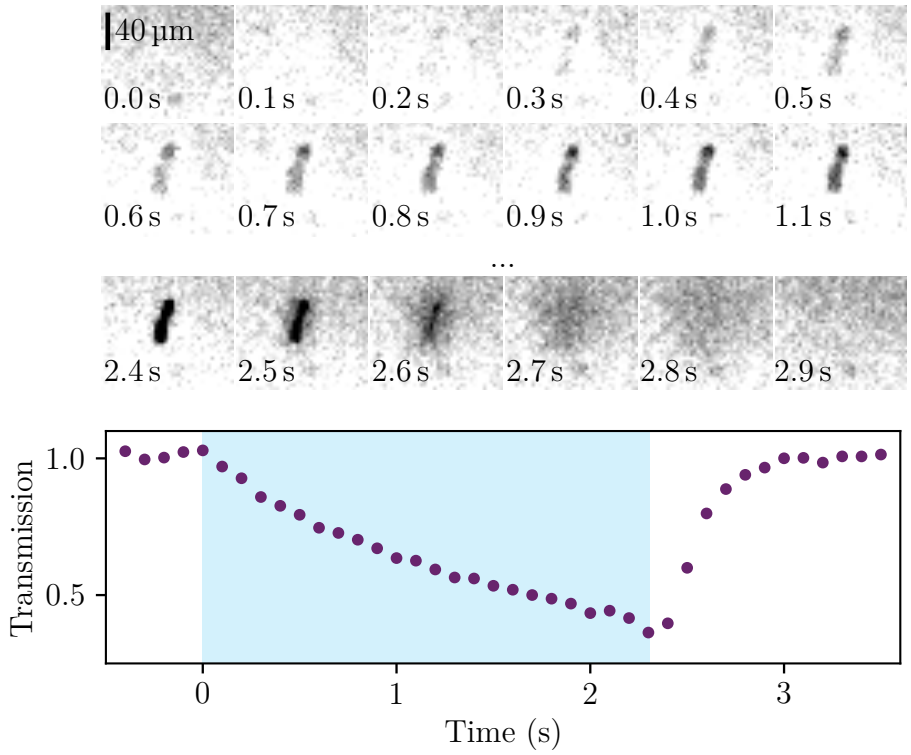

Figure 4.4: **Above:** Sequence of stills illustrating the time dynamics of the LICo effect. A broadband backlight was placed behind the nano-cell (to the right of the schematic in Fig. 4.1), and using a $f = 30\,\text{mm}$ lens the cell was imaged onto a CCD. For this dataset the 780 nm laser remained off, with only the 450 nm laser used (with a power of 30 mW, and focused into the cell using the same $f = 30\,\text{mm}$ lens). Images were taken in a region of the cell with 500 nm confinement, at a temperature of 100 °C. The 450 nm laser was switched on at 0 s, causing a dark region of condensed rubidium to steadily form. The laser was turned off at 2.3 s, after which the dark region dissipated over a much shorter timescale of order 0.5 s. The shape of the spot was due to the profile of the 450 nm laser beam used (which was not directly observed here as 450 nm light was removed by spectral filtering before imaging). **Below:** Graph quantifying the change in count rate on the CCD within the condensed dark region, relative to a control region outside of this region (to account for changes in background light levels). The blue shaded region indicates when the 450 nm laser was on.

the reproducibility of the response in our cells. Reproducibility is a problem in many other LIAD works, though is little discussed in the literature.

4.3.2 Light induced condensation

The effect we term LICo was observed under similar conditions to those required for LIAD, but on longer timescales. The white-light backlit images in Fig. 4.4 show the formation and subsequent diffusion of a condensed rubidium region, with the bottom graph quantifying the darkening of the region over time. The opacity increased approximately linearly over time whilst under 450 nm illumination, before decaying exponentially back to the background level as the dark region visibly diffused. Unlike LIAD, we found that the LICo effect could be clearly observed with the cell at room temperature as well as at 100 °C, suggesting a lack of strong temperature dependence. However we found that its magnitude varied based on the cell history, and was greatest after the thin regions of the cell had been flooded with rubidium. This is likely because the flooding replenishes the reservoirs of wall-adsorbed atoms which deplete over time.

In our experiments, LICo was observed in 500 nm and 1 µm thickness cell regions, but was not observed in a 2 µm thick cell. One possible explanation is that the effect may be dependent on surface roughness. We have measured the roughness of a standard etched 500 nm region in section 3.2, however during this work we did not characterise the deeper etches in the same way. Whilst we have not performed quantitative measurements, under inspection the 2 µm region is visibly rougher. it is possible that the roughness alters the wetting properties of the surface and thus changes the formation dynamics of clusters. Another possible explanation is that the effect is intrinsically linked to the more confined regimes. It has been suggested that in narrow pores LIAD liberates atoms from being adsorbed within surfaces only for them to form clusters on the surface [141], and perhaps it is true that in our more confined geometries the liberated atoms quickly collide with the walls and form clusters. By contrast, it is possible that in less confined geometries the atoms diffuse more effectively in the vapour phase away from the focal spot. By comparison with LICo, LIAD was observed in all three cell thickness regions listed, but experiments in the thinner two regions were hampered by the LICo condensed rubidium spot formation. This spot scattered laser light onto our detector causing considerable noise in our results. Hence we presented LIAD data from the 2 µm region in Fig. 4.2.

Having observed the LICo spots form with lengthscales of order 50 µm

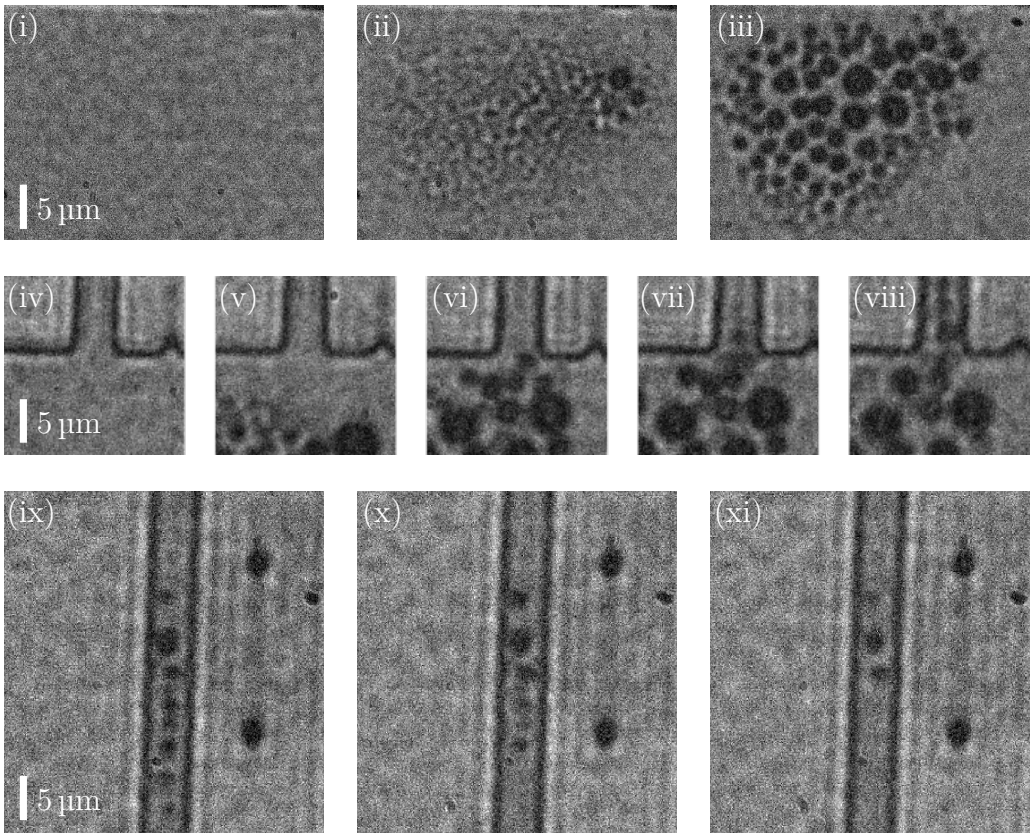

Figure 4.5: Sequences of stills illustrating the microscopic properties of the LICo effect and a potential application. The 450 nm laser had a power of 16 mW and was focused via a $f = 2$ mm focal length, NA = 0.7 plan apochromat objective lens into a region of the nano-cell with 500 nm confinement. Imaging was done using the same objective onto a CCD, with a broadband backlight (450 nm light was filtered out before the CCD). **Top:** LICo cluster formation images in the 'slab' 500 nm region: (i) before the 450 nm laser was turned on; (ii) after 2.4 s of 450 nm illumination; (iii) after 6.7 s of 450 nm illumination. **Middle:** Cluster movement images occurring after (iii). In the images the 'slab' 500 nm region is below, with a 5 µm × 500 nm channel above. Between (iv) and (viii) the focal spot of the 450 nm laser was translated upwards into the channel entrance, moving the clusters upwards and some finally into the channel. **Bottom:** Subsequent images after moving the droplets 100 µm along the channel. The laser was turned off at (ix), and the droplets were allowed to diffuse. Images (x) and (xi) are 2 s and 4 s after (ix), respectively. Note that the two dark spots to the right of the channel are other etched structures in the cell and not condensed rubidium.

(as shown in Fig. 4.4), it was decided that to understand more about the effect and its potential applications it would be useful to study the effect on the micron-scale. This meant moving to a high-NA illumination and imaging

setup, and results of this are shown in Fig. 4.5. In this figure we image the microscopic properties of the condensed rubidium clusters, and also demonstrate a potential application of the LICo effect. Firstly we show cluster formation on the micron scale, showing that clusters of order 1 µm or smaller firstly formed, before combining to form larger clusters up to 3 µm over an illumination timescale of around 7 s. We then show that by moving the 450 nm laser focal spot, it was possible to move these clusters around the cell. Here we moved the clusters from a 500 nm thickness 'slab' region into a 500 nm × 5 µm channel above. Finally we observed the dissipation of these clusters upon ceasing 450 nm illumination, with clusters persisting for a timescale of at least 4 s. It has already been suggested that diffusion dynamics play a role in vapour distribution in thin cells (especially in more confined geometries such as channels [1]), and the 4 s timescale observed here is longer than the 0.5 s timescale for cluster dissipation in Fig. 4.4. However, we postulate that due to the greater magnification in these images we can observe smaller clusters for more of their lifetime. It is still unclear from these results whether dissipation into the vapour phase and the dynamics of vapour diffusion is considerable, or whether dissipation into the glass substrate and its dynamics is dominant. As such, later in Fig. 4.6 we will present the fluorescence activity from a region close to a LICo spot.

We postulate that the LICo effect we have measured is of similar origin to those described in [141, 147], as discussed in section 4.1. However, much further study is required to understand the effect and its mechanisms in detail. Another potential explanation for the effect observed is the possibility of electric fields being induced at cell surfaces, which could induce dipoles in the rubidium atoms and thus attract them. We could test the theory that the effect we observe is the formation of Rb nanoparticles on surfaces further using methods as described in [150]. In that work, the authors illuminate the formed nanoparticles with NIR light, detaching atoms from the clusters leading to them no longer being visible. However, one considerable difference between their experiment and the one presented in this work lies in the substrate choice. This is likely to be a factor in the considerably different timescales observed for their clusters to diffuse naturally (hours in their work compared to seconds in our study).

To test one potential use case of the LICo effect, we decided to study the atomic fluorescence in a 500 nm region of the cell before and after a LICo spot

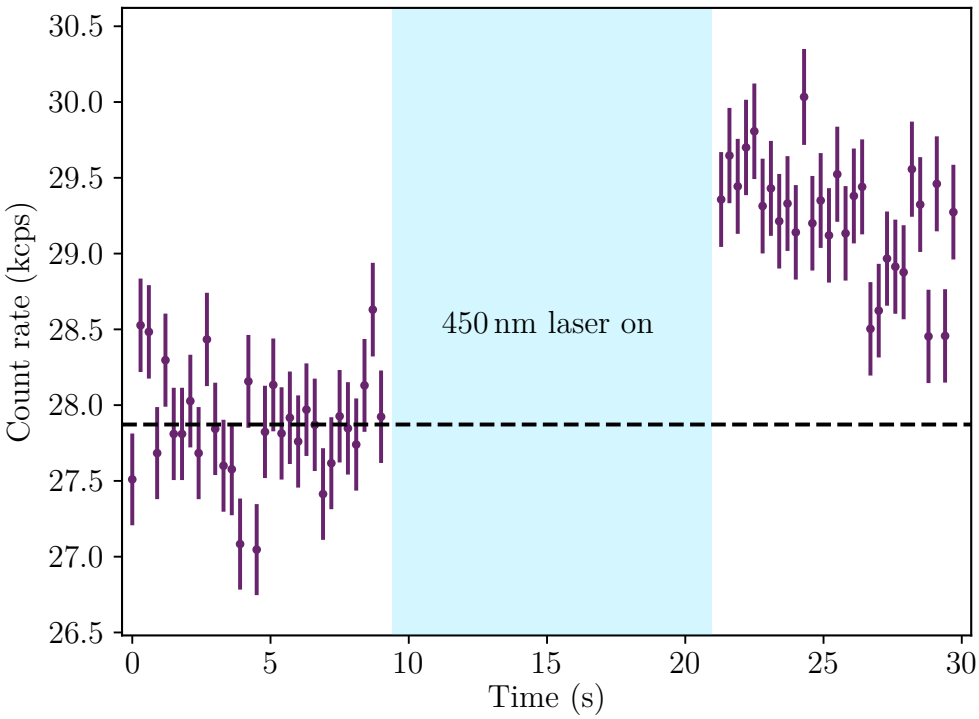

Figure 4.6: Graph showing the atomic fluorescence activity at 420 nm (purple), before and after illumination for approximately 12 s with 450 nm light. This illumination caused condensed regions of rubidium to form in the vicinity on the cell surfaces, through the effect we term LICo. The vapour phase atoms were excited to the $5D_{5/2}$ state using co-propagating 780 nm and 776 nm lasers (both with powers of 300 µW), and could then decay via the emission of a 420 nm photon. We used 7 mW of 450 nm laser light, incident on a cell thickness region of 500 nm at a temperature of 70 °C. All lasers were focused into the cell using an $f = 2$ mm objective lens. The black dashed line indicates the average background fluorescence count rate before 450 nm illumination.

had been formed. For this we used a two-colour excitation scheme (which will be discussed at length in chapter 5). Two lasers (at 780 nm and 776 nm) were used to excite vapour atoms to the $5D_{5/2}$ state, from which they could decay via the $6P_{3/2}$ state and emit a photon at 420 nm. This technique is particularly useful for situations where scattering can be an issue, as the emitted photons are far from the excitation wavelengths, meaning standard spectral filtering can easily separate the two. As such we opted for it here where single-colour excitation would be hampered by the LICo condensed regions scattering laser light onto the detectors. For this experiment, we studied the atomic fluorescence activity at 420 nm before and after illumination using our 450 nm laser,

and the results of this are shown in Fig. 4.6. With our setup (and due to the power of the 450 nm laser used) we could not observe fluorescence during the formation of the LICo spots. However, we recorded fluorescence activity before and after this. We observed that the atomic fluorescence activity after LICo spot formation is indeed higher than before, suggesting some atoms diffuse into the vapour phase from the transient higher wall-adsorbed atom density due to LICo. The higher density decays slightly over a timescale of order 10 s. However, the effect is only a 6% increase on the background level before the illumination, and further study would be needed to verify this increase and quantify it in more detail including the time dynamics and decay of the higher density. This increase is not considered to be of LIAD origin, as the fluorescence activity is higher after the turn off of the 450 nm laser and decays back toward the background level, in stark contrast to the LIAD results shown in Fig. 4.2.

4.4 Conclusion

In conclusion, for the simple case of non-resonant illumination of a rubidium nano-cell using an inexpensive 450 nm laser diode setup, we have observed two complex and competing effects. For LIAD, we have quantified the increase in vapour density achievable in a 2 µm thick uncoated fused silica vapour cell, adding to the information already available as to the effectiveness of LIAD in different regimes. We have also studied in detail the temporal dynamics of the LIAD process over seconds of 450 nm illumination in our cells, measuring the various decays and timescales involved. We have further demonstrated that LIAD can be performed in an incredibly localised manner, using our high-NA objective to focus our activation laser down to approximately 1 µm, paving the way for experiments with localised on-demand density variation and gradients.

We have observed a contrasting effect which we term LICo, whereby a buildup of condensed atoms is observed at the location of the 450 nm laser spot. This effect has previously received relatively little attention in the literature, and our cells facilitate study of the effect on lengthscales previously little-explored. We have induced the effect in a localised manner using a laser focal spot of order 1 µm, and imaged the resulting clusters with sub-micron resolution, enabling the measurement of cluster sizes. Understanding the

LICo effect is crucial, not least in avoiding its adverse impacts during LIAD experiments, whereby the dark spot induces noise by blocking and scattering laser light.

We studied the variation of the two effects (LIAD and LICo) with temperature, and found that LIAD is more effective in hotter cells, whilst LICo was observed across a range of cell temperatures including room temperature. This thus informs parameter choices for future experiments in these regimes. The difference in timescales between the two processes is also thus of key importance, and given the timescales we have measured (milliseconds for LIAD and seconds for LICo), we suggest that using short pulses of 450 nm light is a promising avenue of further study. In this way it may be possible to gain the fast millisecond vapour density variation benefits of LIAD without allowing for the slower buildup of condensed rubidium of LICo over the course of seconds. However, future studies would need to assess the appropriate duty cycle of the pulses to stop the formation of LICo clusters.

Chapter 5

Two-colour spectroscopy in micron-scale structures

5.1 Introduction

Spectroscopy of atoms in confined geometries and close to surfaces has long been an area of much interest, with techniques such as selective reflection allowing early insights through excitation of atoms via short (of order 100 nm) evanescent fields [151]. Later, thin vapour cells were developed, where the tight confinement ensures all vapour-phase atoms exist within a given distance from a cell surface [45]. This development also allowed for other conventional spectroscopic methods to be used in atom-surface investigations [46]. Spectroscopy of vapours confined to small volumes has now been the subject of much study, for example with atoms confined to the micron-scale core of hollow-core fibres [84]. In that work, the authors assessed the relative contributions of power broadening and transit time broadening to spectral line-shapes, and proposed these to be limiting factors for technological applications of atoms close to surfaces. As that study demonstrates, spectroscopy provides a good measure of atomic behaviour and is a key tool in understanding the behaviour of confined atoms and the technological limitations of atom-based devices.

Spectroscopy of thermal vapours confined specifically to thin cells has been an active area of research for many years [152]. A number of techniques have been used successfully, including transmission spectroscopy [37, 108], total internal reflection fluorescence (TIRF) [1, 82], and selective reflection [72, 106]. The various methods studied each have benefits and drawbacks. Transmission

spectroscopy is a standard technique in conventional vapour cell experiments, is simple to implement, and has generally well-understood results for which robust models exist [3, 22]. However, the optical depth of the sample in a micro- or nano-cell is generally much lower than in conventional vapour cells, and thus transmission spectroscopy results in a much lower signal-to-noise ratio than in conventional cells, necessitating higher temperature operation (which is less desirable for some applications, and induces extra spectral line-broadening). The TIRF technique, meanwhile, employs an evanescent field of order 100 nm in extent, useful for probing atoms close to surfaces. It can give a high signal-to-background ratio [1] for spectroscopy, as well as generating unconventional polarisation modes to interact with the atomic sample [153,154]. However, the technique has limitations in terms of requiring a planar surface for total internal reflection to occur at, as well as requiring optical access at an angle to the cell surface. Our nano-cells were designed to overcome some of these issues, as detailed in chapter 3, however the requirement of a planar surface is still an issue for probing atoms confined in complex structures (such as those shown in Fig. 3.4).

For rubidium, the techniques outlined above often use a single laser frequency to interact with the vapour atoms, a common example being the pathway labelled (a) in Fig. 5.1. Here the atoms are excited to the $5P_{3/2}$ state using 780 nm laser light, and emitted photons of the same wavelength are detected. The inability to use spectral filtering to separate the input and output light is the main drawback of such single-colour fluorescence techniques, meaning that although geometries such as TIRF allows for single-colour spectroscopy which is theoretically dark-field, in practice results are often not free of background noise. Generally such noise is due to scattered laser photons from, for example, cell surfaces and features. This noise poses a problem, in particular for cells with more complex structures such as micro- and nano-channels or pockets (see, for example, Fig. 3.4(b-h)), where laser light is efficiently scattered into the detection path by feature edges. Hence, in complex structures, spatially-filtering the excitation laser light away from the detection pathway using the TIRF geometry is no longer sufficient to remove background laser photons.

In this chapter, we detail and demonstrate an alternative two-colour excitation scheme which allows spectroscopy in our thin cells (and specifically of atoms confined to nano-structures) via fluorescence detection at 420 nm.

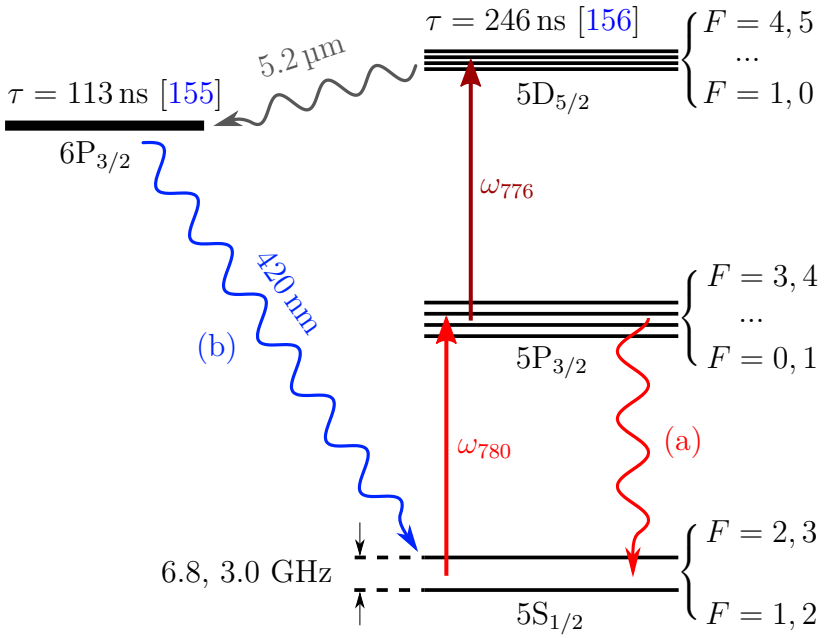

Figure 5.1: Partial rubidium energy level diagram showing the key transitions used in this work to probe the atoms inside the nano-cell. Relevant hyperfine states are indicated for ^{87}Rb, ^{85}Rb (note that these are omitted for $6P_{3/2}$ which we do not spectroscopically probe). The two fluorescence detection pathways used in this work are labelled (a) and (b). Scheme (a) relies on a single excitation laser at 780 nm addressing the rubidium D2 line, driving population to the $5P_{3/2}$ state which then decays via emission of a photon of the same frequency. Scheme (b) employs two lasers at 780 nm and 776 nm to drive atoms to the $5D_{5/2}$ state, from which they can decay via the $6P_{3/2}$ state and produce a photon at 420 nm. The lifetimes, τ, of each of these upper states are indicated.

The scheme is depicted in Fig. 5.1, with the fluorescence pathway used for detection labelled (b). The scheme for producing this 420 nm fluorescence is already well-documented, with numerous existing studies [157–159] and various applications including the generation of collimated 420 nm light [160]. Fluorescence spectroscopy has even been performed using this scheme in a hollowcore fibre with 45 µm internal diameter [161], demonstrating narrow line-widths and high optical depths. However, reported results from more confined systems such as nano-cells have been limited. Some are described in [82] and [1], the latter of which will form the basis for this chapter. One study asserted that using this scheme in a thin cell may be advantageous, as the emission at 420 nm as compared to other pathways is more favourable than would be expected from branching ratios. The relative increase in fluor-

escence from this pathway in a thin cell is due to incomplete quenching of the $5D_{3/2}$ state at the cell walls [162].

As fluorescence (420 nm) and excitation (780 nm and 776 nm) photons are considerably separated in wavelength in the two-colour scheme used in this chapter, we can perform straightforward spectral filtering of any excitation photons scattered by the substrate (using commercially available bandpass filters). This facilitates dark-field measurements in arbitrarily complex geometries, whereby 420 nm photons are only generated where the two beams overlap in locations containing vapour atoms. In this chapter we will show that adopting this two-colour excitation scheme in combination with the approach of tightly-focusing one or both excitation beams into the nano-cell allows for novel experiments probing atomic vapour confined to nano-structures. Such experiments include studies of vapour distribution and diffusion in these confinement regimes, which may prove useful in the development of compact atom-based devices. The study of vapour diffusion in confined geometries is important in many fields, for example for understanding the filling rate of hollowcore fibres [163].

5.2 Methodology

As detailed in [1], the thin front panel of our nano-cell design allows for the use of high NA optics to image cell features and probe atoms within. With such high-NA lenses it is possible to optically resolve individual nano-scale structures, as well as address individual structures with laser light and collect fluorescence from atoms confined within. In this work we employed a NA = 0.7 plan apochromat microscope objective to address atoms within volumes of order λ^3 confined in nano-scale structures, where spatial confinement is typically ≤ 1 µm in one or two dimensions. Figure 5.2 shows the experimental setup, where the two excitation lasers are delivered to the nano-regions in one of two geometries. We will investigate both geometries, with the beams delivered in either co- or counter-propagating arrangements (labelled (a) and (b) respectively). For co-propagation, the two excitation lasers were both tightly-focused into the cell via the microscope objective, whereas for counter-propagation the 780 nm excitation beam was instead incident on the nano-regions through the back-face of the cell, via a $f = 100$ mm lens (whilst the 776 nm laser was incident through the microscope objective as before).

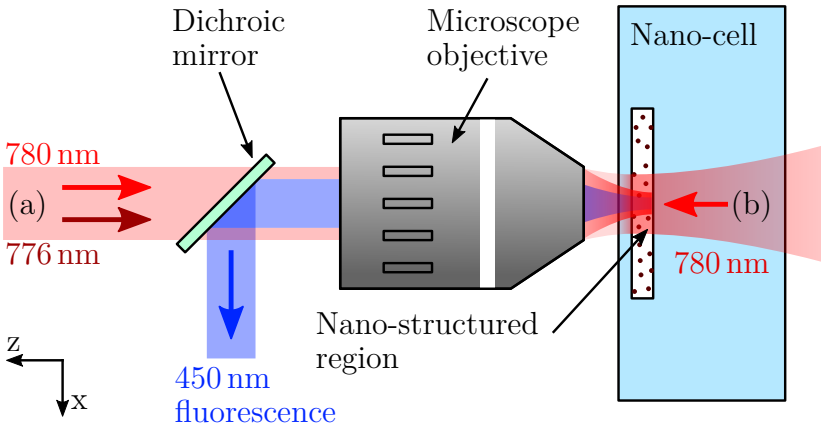

Figure 5.2: Top-down schematic (not to scale) of the fundamental components in the two-photon fluorescence microscopy (TPFM) setup. Probe lasers at 780 nm and 776 nm were delivered to the nano-regions of the vapour cell, with the 780 nm beam co-propagating (a) or counter-propagating (b) relative to the 776 nm beam. Beams from position (a) were focused into the nano-cell by a 100× plan apochromat microscope objective, with 2 mm focal length, 6 mm working distance, and NA = 0.7. From (b) 780 nm the beam was weakly focused through the back face of the cell (and ITO coating) using an f = 100 mm lens. Atoms inside the nano-structures produce 420 nm fluorescence (see the excitation scheme in Fig. 5.1) which was collected by the microscope objective, and reflected by a dichroic mirror onto a photon-counting photomultiplier tube (PMT) for detection. Bandpasss filters at 420 nm (with 5 nm FWHM) excluded background light from the PMT.

Fluorescence at 420 nm was collected via the microscope objective, separated by a dichroic mirror, and detected by Hamamatsu H10682-210 photon-counting photomultiplier tube (PMT). Photon counts were recorded by a sensL HRM-TDC single-photon counting module (or by a LeCroy WaveRunner 625Zi oscilloscope for more crude measurements and testing - however this was slower and gave a reduced timing resolution). Multiple bandpass filters were placed before the PMT, and these typically had 5 nm FWHM centred at 420 nm (giving 97% transmission at 420 nm and OD7 around 780 nm). Using a number of these in combination allowed for near-perfect extinction of emitted or scattered light at 780 nm and 776 nm, as well as other background light.

For spectroscopic measurements, the atomic response was studied as the 780 nm laser was frequency scanned through resonance. Excited state polarization spectroscopy [164] was employed to frequency stabilize a second laser

at 776 nm to the $5P_{3/2} \rightarrow 5D_{5/2}$ transition. More details of the experimental setup can be found in Appendix A.2. Using this methodology, we spectrally probed the D2 transition through detecting 420 nm fluorescence photons from the $6P_{3/2} \rightarrow 5S_{1/2}$ transition (see Fig. 5.1). By splitting off a portion of the scanning 780 nm laser light before the experiment, and passing this through a reference 75 mm rubidium vapour cell in a counter-propagating geometry, scans were calibrated using the known frequencies of the relevant rubidium sub-Doppler hyperfine features [21]. A Fabry-Perot etalon was also used in the calibration, to correct for non-linearity in the variation of frequency with time during a laser scan. This was necessitated by the use of a DFB laser diode which had a significantly non-linear scan rate.

5.3 Discussion

5.3.1 Counterpropagation

In thermal vapour physics, it is common to use two beams (of the same or differing frequencies) to resolve sub-Doppler spectral features [21] for use as reference spectra (e.g. see the top panel of Fig. 5.4). In a counter-propagating geometry, an atom that is Doppler-shifted away from resonance with one beam due to its velocity component parallel to the beam (i.e. an effective detuning from resonance of$\Delta = k_1 v$) is Doppler shifted in the opposite direction with respect to the second beam (i.e. $\Delta = -k_2 v$). Thus, in the limit where the two beams have similar enough frequencies, i.e. $k_1 \sim k_2$, the Doppler shifts are cancelled. We have implemented such a scheme for TPFM, in which the two excitation beams are counter-propagating (see Fig. 5.2, with the 780 nm laser along pathway (b)). As both excitation lasers are close in wavelength, this scheme would give sub-Doppler resolution in a conventional cell. In thin cells there are other sources of broadening such as due to the transit time of the atoms. However, as can be seen from the resulting fluorescence spectrum shown in Fig. 5.3, this scheme gives well resolved sub-Doppler resonance lineshapes in our thin cell. The lines observed correspond to the transitions from hyperfine $5S_{1/2}$ ground states to the allowed $5P_{3/2}$ hyperfine states (which are indicated above the main plot). Due to the nature of the two-photon scheme, and in contrast to single frequency pump-probe schemes [21], crossover resonances are absent. This affords better resolution of the allowed hyperfine

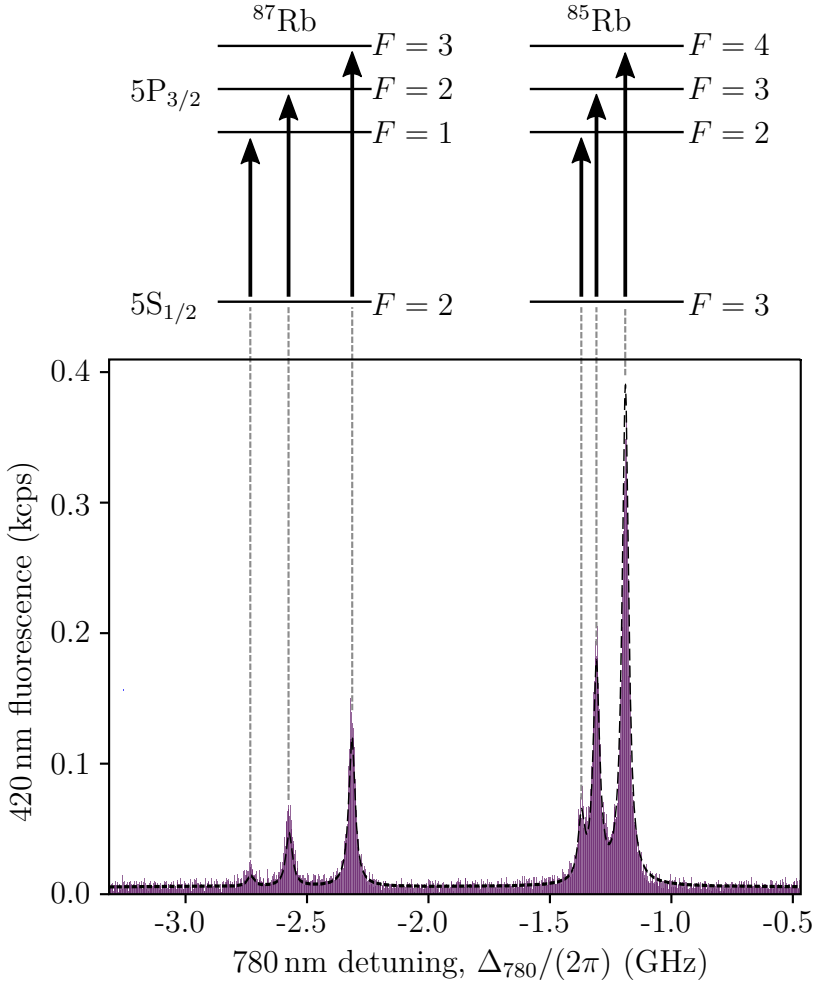

Figure 5.3: 420 nm fluorescence (purple histogram) recorded from a 1 µm thick cell (i.e. 1 µm confinement along z in Fig. 5.2). A counter-propagating two-photon excitation geometry was used. An empirical fit comprising six Voigt profiles is shown (black dashed line). For fitting, the locations of the resonances were constrained to the relevant hyperfine transition frequencies, their relative magnitudes were constrained to the isotopic abundance-weighted transition strengths, and their widths were set to be equal (but allowed to vary as a fit parameter). Partial energy level diagrams are shown above the main plot for reference. For this dataset, powers of 350 µW at 780 nm (focused into the nano-region with the $f = 100$ mm lens) and 20 µW at 776 nm (focused with the $f = 2$ mm lens) were used, with a cell temperature of 60 °C and an integration time of 12 hours.

transitions.

Our empirical Voigt fit to the resonance line-shapes gave a FWHM value of 31.8(8) MHz, much less than the usual (unconfined) Doppler width which is of order 1 GHz. The fit also constrained the ratios of the peak heights

to be the isotopic abundance-weighted transition strengths for the relevant transitions. The best-fit line shows good agreement with the data, suggesting the peak heights are weighted in the expected way, which is notable given the possible extra processes at play such as hyperfine pumping and collisional effects. We also observed a high ratio of signal to background, demonstrating the usefulness of this two-colour scheme. However, the long integration time of 12 h is a trade-off for using such low laser powers, and extra broadening would be induced at higher powers.

5.3.2 Copropagation

For comparison to the counter-propagation case, spectra were also obtained using the TPFM method with a co-propagating geometry, and a selection of these are shown in Fig. 5.4. For this experiment the nano-cell was positioned at various distances from the focal point of the $f = 2\,\text{mm}$ microscope objective, such that atoms in the nano-region experienced the local field at each displacement. The excitation beams had powers of 7 µW at 780 nm and 20 µW at 776 nm (with each dataset having an integration time of 1–10 min at a cell temperature of 65 °C). The spectral features in the datasets arise due to the hyperfine structure of the $5P_{3/2}$ state, though not all hyperfine states were fully resolved. For ^{85}Rb we observed a secondary resonance to the left of the main peak. This is due to contribution from a hyperfine level which is slightly off-resonance with respect to the 776 nm laser. This peak appears shifted, and whilst for the purposes of this dataset no specific effort has been made to perfect the calibration of the spectra, we speculate that this is a shift akin to those seen in EIT studies [165].

The dataset shown in Fig. 5.4 illustrates the potential of micro- and nano-scale alkali-metal vapour cells for sensing applications: as the thin atomic medium is translated, it has a clear spectral response to changes in the spatially-varying intensity. The observed modification of the spectra can be attributed to two effects. Firstly, power broadening causes the broader spectral features closer to the focus ($z = 0\,\mu\text{m}$) due to the higher intensities experienced by the atoms. Secondly, moving away from the focus alters the amount of fluorescence generated by the atoms (via changing both intensity and illuminated area) and also collected by the objective lens, causing the changes in count rates observed. The spectra which do not strongly exhibit the effects of power

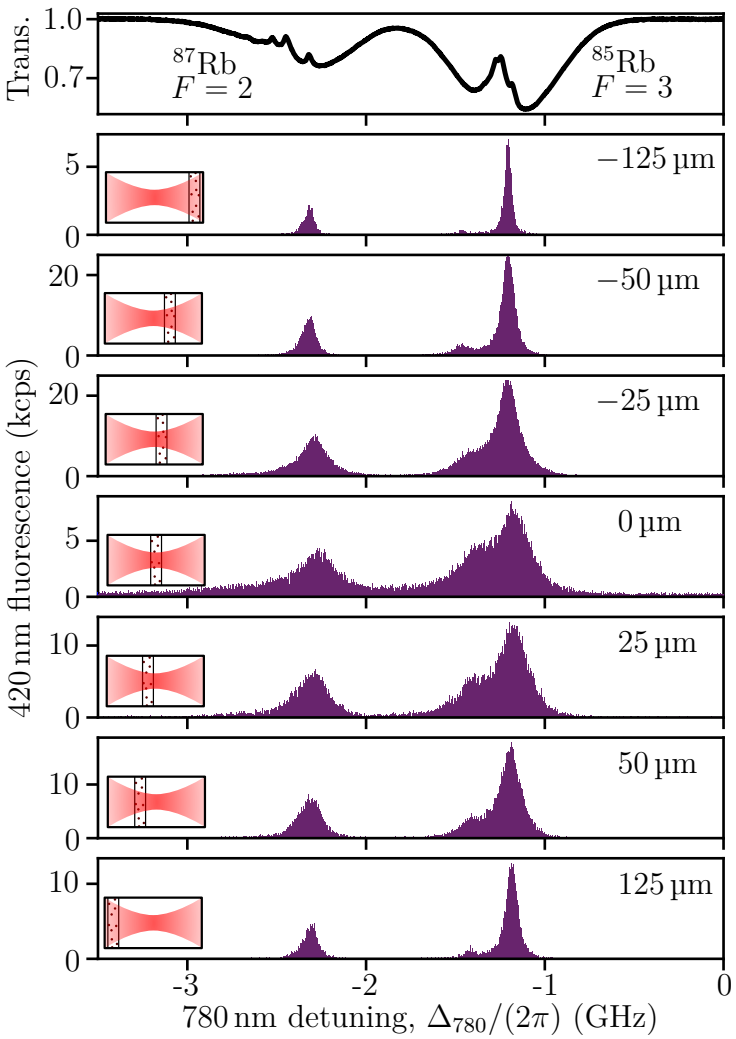

Figure 5.4: **Top:** Sub-Doppler transmission spectrum produced using pump-probe spectroscopy in a 75 mm vapour cell, used as a frequency reference. Sub-Doppler features associated with the hyperfine splitting of the $5P_{3/2}$ state (see Fig. 5.3) appear within the Doppler-broadened profiles of the hyperfine ground states of the two Rb isotopes (the chosen states are labelled). **Below:** TPFM spectra recorded with 780 nm and 776 nm beams co-propagating (both along path (a) in Fig. 5.2) incident on a region of the cell with 1 µm thickness in the direction of the excitation beams. The cell was translated with respect to the focal point of the beams (labelled 0 µm), such that the atoms experienced different intensities at different z positions (labelled). The inset diagrams illustrate this translation of the cell (and thus the atomic layer). High intensities at the focus gave rise to power broadening, and differing count rates were due to the changing collection efficiency and illumination area. Features in the TPFM spectra relate to the hyperfine $5P_{3/2}$ states, though some were not fully resolved or observed.

broadening (for example those at $z = \pm 125\,\mu m$) also illustrate the benefit of nano-scale confinement of atoms: narrow sub-Doppler fluorescence resonances are obtained in a co-propagating geometry as well as the counter-propagating one seen in Fig. 5.3. This property of thin cells allows for a compact scheme whereby a single objective lens delivers both excitation beams to a tightly focused spot in the atomic medium, as well as collecting the atomic fluorescence. Fitting a Voigt profile to the uppermost spectrum ($z = 125\,\mu m$) in Fig. 5.4 yields a FWHM of 57.5(6) MHz, which is the same order of magnitude as was achieved in the counter-propagating case. We attribute this to the velocity selection effects in micro- and nano-thickness vapours (which are discussed in chapter 2 and will be studied in more detail in chapter 6), which suppress spectral contributions from atoms with higher velocity components perpendicular to the cell walls. This allows sub-Doppler spectroscopy in geometries which would, in bulk vapours, produce Doppler-broadened spectra [166].

As discussed in section 5.1, the two-colour method facilitates dark-field spectroscopy of atoms confined to complex micro- and nano-scale structures. To illustrate this, the TPFM method in the co-propagating geometry was applied to probe atomic vapour confined along a channel with width 1 µm and depth 1 µm, yielding the results shown in Fig. 5.5. By translating our cell and studying the fluorescence activity at various distances along a $1\,\mu m \times 1\,\mu m$ channel, we studied the distribution and behaviour of atoms confined within. We found that the fluorescence intensity reduced along the channel (with all other experimental parameters held constant between measurement sites), suggesting that a density gradient existed in the vapour. Given that this particular cell had been in operation for 1 year, it would be reasonable to expect that an effective steady state had been reached in terms of atomic vapour distribution. However, as is shown by the decaying integrated count rate in Fig. 5.5(b), this is not the case. By repeating such measurements, we have found that atomic vapour density was reproducibly not uniform along channels with confinement on lengthscales $\leq 1\,\mu m$. This provides new and important insight into the diffusion properties of atoms inside micro- and nano-scale structures. The vapour pressure is perturbed simply by the presence of tight confinement, which is a result that has also been observed in hollow core photonic crystal fibres [63]. Our cell platform allows for novel insight by facilitating measurements on the lengthscales over which this effect occurs (singular microns), both in terms of atomic confinement but also

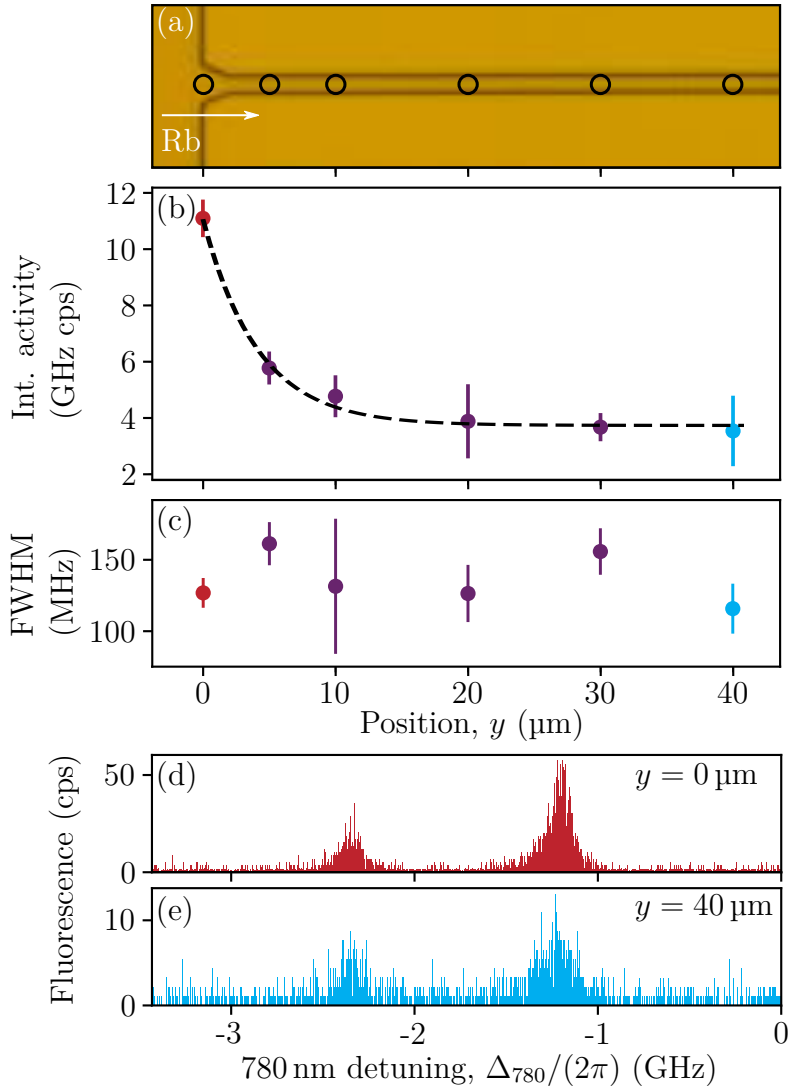

Figure 5.5: **(a)** Bright-field image of a single channel, with a width and depth of 1 µm. In this image the source of rubidium atoms (reservoir) is to the left, as indicated. TPFM spectra were recorded at various locations along this channel (indicated). All spectra were empirically fitted with Voigt profiles, and the integrated activity **(b)** and FWHMs **(c)** obtained from these fits are plotted as a function of position. An empirical exponential decay was fitted to the activity data (black dashed line), which yielded a characteristic 1/e decay length of 4.0(11) µm. Error bars for both the activity and FWHM values were estimated using the functional approach [167]. Plots **(d)** and **(e)** show two example spectra from the extreme points studied. For this experiment, the excitation beam powers used were a compromise between signal strength and power broadening, with 50 nW of both 780 nm and 776 nm light focused to an approximately 1 µm spot. Integration times varied between 0.5 hours for the 0 µm dataset up to 9 hours for the 40 µm dataset, and the cell temperature was 60 °C.

spatial resolution (i.e. the micron-scale laser spot size allows for measurement of the change in response over micrometric distances).

To the author's knowledge, the only similar result to this density-dependence along a thin channel was published in a previous work [82] by Hamlyn. In that study, the cell was kept at room temperature, and a smaller channel cross-section (500 nm × 1 µm) was used. It is likely that different laser powers were also used. However, experiments were performed in a similar way and using the same excitation scheme to obtain fluorescence spectra. In both studies the same qualitative reduction in atomic fluorescence (and thus density) along a thin channel was observed, for two different nano-cells at different temperatures and with different histories of heating and flooding. Indeed, later in this thesis in section 6.5.4 we report the same effect using a slightly different methodology in a cell with a different history. Thus we can conclude that this density variation is a property of vapours confined to thin channels.

That we can achieve the required SNR to perform spectroscopy on vapours confined to micron-scale channels is also a significant achievement. By fitting Voigt profiles to the spectra shown in Fig. 5.5(d) and (e), we obtained FWHMs of 155(4) MHz and 130(30) MHz, respectively. This alludes to the tight focussing of the beam, which leads to power broadening of the spectra. However, the width of these spectral features is still smaller than the Doppler width, owing to the velocity-selective nature of thin cells. The FWHM of all spectra obtained at different distances along the channel are shown in Fig. 5.5(c), and it was observed that the FWHM of the resonances did not vary significantly in the tight confinement regimes studied.

The TPFM method applied to a nano-cell offers promise for the detection and study of low numbers of vapour atoms confined to complex nano-scale structures. From the count rates observed in Fig. 5.5(e), we have extracted an estimate of the number of atoms excited to the $5D_{5/2}$ state. Accounting for the efficiency and throughput of our detection setup, as well as the lifetime of the $5D_{5/2}$ state, we estimate that the on resonance count rate observed corresponds to a mean value of just 0.01 of these excited atoms within the excitation volume. If instead we extract the atomic number density from the measured cell temperature and the rubidium vapour pressure curve, as is standard in experiments with bulk vapour cells [38], we find a mean ground state atom number of 1.5 within the same volume. This could be consistent, as we would expect that only a fraction of these are excited to the $5D_{5/2}$

state, and an even smaller fraction have chance to decay and emit a photon before colliding with a cell wall (see chapter 6). We have also illustrated that tight confinement impacts atomic density, and thus it is unlikely that even the mean ground state atom number is as high in our confinement regimes as vapour pressure curves would predict. However this crude estimate provides an approximate order of magnitude atom number for context.

5.4 Conclusion

In this chapter, we have demonstrated thin cell spectroscopy in various confinement regimes and laser beam geometries. Overall, this demonstrates the versatility of our bespoke cell platform and aids in the fundamental understanding of spectroscopy of tightly-confined vapours. Furthermore, our results are an initial step towards the development of technological applications, for example in the demonstrations of the differing vapour-layer response when translated across a tightly-focused beam. Using this spectral data combined with imaging the atomic response could be useful to give a full picture of a tightly focused laser beam or more complex field with variations on the micron-scale.

Our data have shown that it is possible to spectrally filter fluorescence signals using the TPFM scheme in such a way that the noise observed far off resonance, such as that in the spectra shown in Fig. 5.3 and Figs. 5.5(d) and (e), is consistent with the dark count rate for the photon-counting photomultiplier tube used (approximately $\leq 5\,\mathrm{cps}$). This was true for laser powers in the regime of µW–nW. From this observation we can see that the methodology is highly sensitive, whilst also allowing for long integration times to accumulate sufficient signals. In fact, our estimates suggest that we have probed mean atom numbers of less than one atom in the focal spot of our laser beam at a given time. Given our demonstrated experimental versatility and considerable control over atom numbers through cell temperatures and confinement, work towards interrogating and studying the response of low numbers of atoms is a promising avenue of further study.

We have performed novel measurements of the reduction of fluorescence activity from an atomic vapour confined along a micron-scale channel structure. Our cell design facilitated novel measurements of the decay lengthscale of this effect, which was found to be in the micrometre range. We conclude

from this result that the confinement itself alters the vapour density distribution. This result provides important insight into the diffusion properties of thermal atomic vapours, and should inform future experiments with highly confined atoms.

Chapter 6

Pulsed excitation of atoms in thin cells

6.1 Introduction

As we have discussed throughout this thesis, experiments using thermal vapours hold some key benefits over those using cold atoms, including in terms of equipment cost, simplicity, and scalability. However, they also have drawbacks, notably stemming from the fact that the atoms being probed are travelling at thermal velocities. In a nano-cell with confinement on the order of hundreds of nanometres, the wall-to-wall transit time for the average thermal atom (with most probable speed $u \approx 300\,\mathrm{m\,s^{-1}}$ at room temperature) can be as little as a few nanoseconds. This short timescale poses a problem for experiments where e.g. a long excited state lifetime or atom-atom interaction time may be required. However, this wall collision timescale also gives rise the velocity-selective nature of such cells, whereby faster atoms contribute proportionately less to overall spectroscopic signals due to quenching at the cell walls. This effect was first noted by Dicke in 1953 [80] and has since been used advantageously, for example as a method of sub-Doppler spectroscopy [105, 107]. In fact, some spectroscopic studies utilising this velocity-selection already exist, using schemes such as spatially-separated pump and probe beams in a micro-cell [168]. However, the temporal dynamics of atomic excitation and emission processes under micro- and nano-scale confinement have received relatively little attention to date. A brief study exists in [37], where a Pockels cell is used to generate resonant laser pulses to interact with

atoms confined to a nanocell. This study by Keaveney suggests that the wall-to-wall transit time becomes the limiting factor on the effective excited state lifetime in a thin cell. The Keaveney experiment, however, was limited by the low (kHz) repetition rate of the input pulses from the Pockels cell.

In this chapter we will investigate the excited state population dynamics of atoms confined to thin cells and build upon the work of Keaveney. Pulsed excitation in thermal vapours has previously been used to demonstrate coherent dynamics [169] and study excited state transition dynamics through effects such as quantum beats [170, 171]. Pulsed excitation is a powerful tool in understanding the time dependence of atomic systems, and has been used previously in cold atom systems to study effects such as the Wigner time delay [26]. Excitation using nanosecond pulses is also a potential method of mitigating the impact of the decoherence time due to atomic motion (which can be of order of nanoseconds in thermal vapour systems), which would help towards the development of technologies based on coherent processes in thermal atomic systems. Thus it is of key importance to understand the vapour response to such short light pulses. In [37], the author shows some preliminary evidence of coherent dynamics in a thermal vapour confined to a thin cell under pulsed excitation, however no other such studies are known to the author.

Velocity selection could also be of crucial importance in future thermal vapours experiments. The observation of some effects (for example certain features in $g^{(2)}$ correlations) can be dependent on interactions between atoms and their emitted fields, which necessitate atoms being in close proximity for a certain period of time [2]. Otherwise, effects such as motional dephasing can become problematic. Thus selecting 'slow' atoms from a thermal vapour ensemble may enhance the response of such collective behaviours. Short pulses on nanosecond timescales also open doors to performing operations on atoms on a shorter timescale than the timescales over which motional dephasing or wall-to-wall transit occurs. This could allow for experiments which overcome the traditional motional issues encountered in atomic vapour physics, without the need for bulky and costly cooling and trapping setups.

As discussed previously in this thesis, the pursuit of low atom numbers in the thermal regime could help towards the realisation of scalable single-photon sources. However, an understanding of the velocity and lifetime of the atoms which can be isolated and interrogated needs to be achieved so as

to understand the limitations of such devices. In this chapter, we will study such effects with a scheme using 1.5 ns resonant laser pulses to excite rubidium atoms confined to a nano-cell with internal dimensions as low as 500 nm. We firstly employ a quantum jump type Monte Carlo model (see section 2.3.2) to simulate the overall dynamics of the atomic fluorescence activity under pulsed excitation, as well as understand the relative contributions of different atomic velocity classes. We then experimentally observe fluorescence from atoms confined to a nano-cell and excited using 1.5 ns resonant laser pulses, which allows us to measure the effective excited state decay lifetime. By comparison with theory, we will then infer the velocity classes which contribute to our fluorescence signals. Such novel insight may be useful in shaping the future of experiments with thermal vapours in confined geometries, whilst the velocity-selective nature of the combination of our confinement and excitation schemes may prove useful for isolating slow atoms within a thermal vapour population.

6.2 Quantum jump simulations

To simulate the behaviour of an ensemble of atoms with thermal velocities, distributed over a Gaussian laser spot and across a vapour cell with nano-scale confinement, it was decided that a Monte Carlo approach would be most fruitful. It was decided that the motional state of the atoms would be modelled classically, whilst the internal state of the atoms would be modelled using the quantum jump (or Monte Carlo wavefunction) method. For simplicity, the QuTiP python package [77] was used for most internal state simulations, which has a built-in function *mcsolve* to perform quantum jump calculations. The quantum jump method and use of the QuTiP python package has been introduced previously in section 2.3.2.

Our simulations were initialised with up to 10^7 starting ground-state atoms, which were each assigned a uniformly randomly chosen x, y, z co-ordinate (within the boundaries of the chosen cell confinement and laser spot size), and a thermal velocity randomly chosen from the Maxwell-Boltzmann distribution. For simplicity, we considered the atoms to be non-interacting. For experiments in this section at room temperature this is valid, as the inter-atomic spacing is much greater than $\lambda/2\pi$. However, deviation may be observed at higher densities - indeed one aim of comparing simulation to experiment later in this chapter is to ascertain whether such assumptions remain

valid in the regimes studied. Each simulation atom was attributed an effective detuning $\Delta_{\text{eff}} = kv_z$ based on its velocity component in the z-direction, v_z (perpendicular to the cell walls and parallel to the laser propagation direction). For each atom, the quantum jump simulation was continued until such time that it collided with a cell wall, which we assume to be quenching and return the atom to the ground state. After this occurred, we added a 'new' atom to the simulation at one of the boundaries to maintain a constant atom number, which was assigned a new set of random parameters. We also applied the Knudsen "$\cos\theta$" law for the angular distribution of atoms leaving the cell surfaces [172]. Effectively our simulations constitute a classical wrapper containing the motional state of the atoms, whilst the internal state is calculated using the standard methodology for quantum jump calculations. More specific details of our simulations are given in appendix B. Note that in reality the internal and motional states of the atom are coupled through atomic recoil upon fluorescence, however we neglect this. This approximation is valid as each atom is likely to undergo at most one fluorescence event before colliding with the cell walls, owing to the short pulse duration and thin cell.

We considered our atoms to be distributed across a Gaussian laser spot in the xy-plane (i.e. we averaged over a Gaussian intensity distribution, which amounts to a distribution of Rabi frequencies experienced by different atoms). Averaging over the contributions of all atoms gave us the overall evolution of the ensemble over time, and thus the temporal dynamics of the atomic fluorescence activity (which is an experimentally-measurable quantity). Meanwhile, information about which simulation atoms performed a quantum jump was retained, allowing us to probe, for example, which velocity classes of atoms contributed to fluorescence activity. Below we will outline some of the key observations from the simulations, before comparing them to experimental data in the rest of this chapter.

Note that in this section the parameters input into the simulations are those relevant to rubidium atoms, as we have ready access to rubidium-filled nano-cells and lasers for experimentation. However, the method could be more generally applied to other alkali metal vapours confined to thin cells.

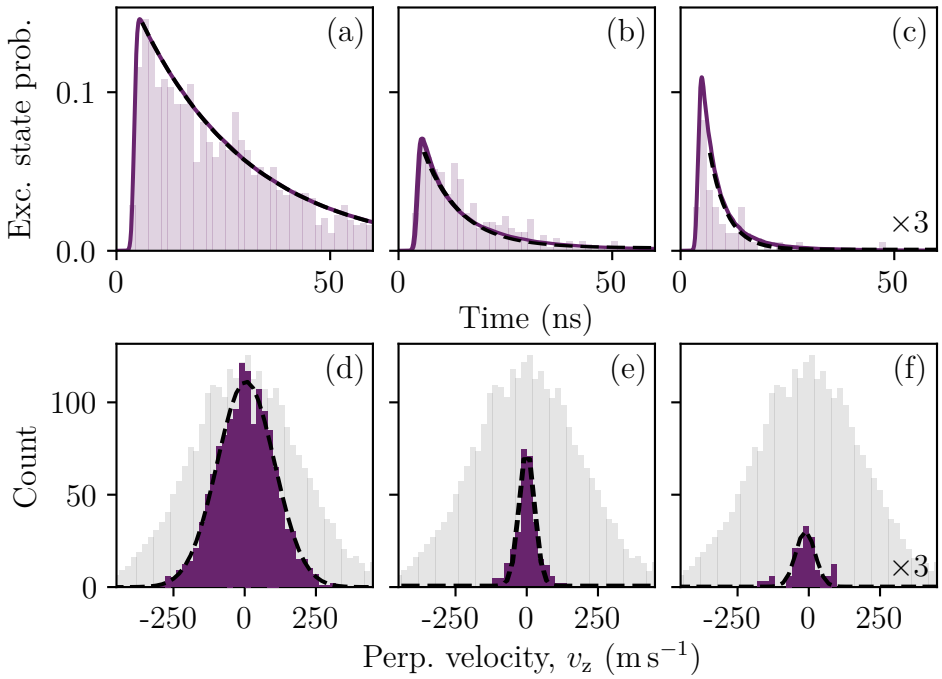

Figure 6.1: Simulated excited state probability upon interaction with a 1.5 ns resonant laser pulse (top), and velocity classes which contribute to atomic fluorescence activity (bottom), for three cases: (a,d) 1 mm 'bulk' cell; (b,e) 1 µm thin ('slab') cell; (c,f) 1 µm × 1 µm 'channel' (shown ×3). The top plots (a,b,c) show the quantum jump events (purple histogram), as well as the excited state probability dynamics (purple line) with an exponential decay fit (black dashed line). The bottom plots (d,e,f) show the perpendicular velocities (v_z) of atoms which perform a quantum jump (purple histogram) for the same three cases as above, with a Gaussian fit (black dashed line). The initial thermal Maxwell-Boltzmann distribution of velocities is shown for comparison (grey histogram). The fitted decay lifetimes and associated velocity distribution FWHMs for the three cases are: (a,d) 25.992(10) ns, 265(3) m s^{-1}; (b,e) 8.60(3) ns, 72(2) m s^{-1}; (c,f) 4.216(17) ns, 60(4) m s^{-1}. For comparison, the Maxwell-Boltzmann distribution has a width of 318(4) m s^{-1}. All simulations were run with 10^5 starting two-level atoms, a peak pulse Rabi frequency of 100 MHz and a pulse FWHM of 1.5 ns, and with a cell temperature of 100 °C. The pulse was modelled as a Gaussian with a peak at 4 ns.

6.2.1 Dimensionality dependence

Our nano-cell design allows for the probing of different dimensionalities of atomic confinement, in principle from confinement in one spatial dimension up to confinement in all three dimensions. The result of our simulations for three different dimensionalities is shown in Fig. 6.1. Here we compare

the effective decay lifetime and velocity distribution (in the z-direction) of atoms contributing to fluorescence activity for three cases: a 1 mm 'bulk' cell, a 1 µm thin ('slab') cell, and a 1 µm × 1 µm 'channel'. The 1 mm cell gives the expected rubidium D2 lifetime of 26 ns, with a considerable width of atomic velocity classes contributing to fluorescence activity. Reducing the dimensionality to a thin 'slab' and then further to a 'channel' reduces both the effective fluorescence lifetime and the width of the contributing velocity distribution. This is due to the decreased atomic time-of-flight before a wall collision in the more confined geometries, illustrating the considerable impact that the choice of geometry has on atomic excitation dynamics.

The technique of TIRF facilitated by our nano-cell geometry has shown to be fruitful for spectroscopy [1]. By extending our simulations to an exponentially-decaying evanescent excitation region (which has a 1/e decay length of order 100 nm), we can attempt to understand more about the dynamics of the excitation and emission processes with a new constraint. The results are shown in Fig. 6.2, and compared to those for the case of a transmitted excitation beam. We observe a change in the decay dynamics, to a curve which is much further departed from a single exponential decay. This is because the excited atoms are now further constrained to be close to one wall, and thus a significant number (those travelling towards the nearby wall) will decay more quickly, whilst the others (travelling away) will have more time to fluoresce. We also observe that fluorescence activity in the TIRF geometry preferentially comes from atoms travelling in one direction (in z), shown by the unequal distribution of velocities on the right hand middle graph. Furthermore, the position of atoms at the point of fluorescence is confined largely to a few hundred nanometres from the cell wall, in a similar way to the evanescent field itself. This extra imposition of confinement of both position and velocity of emitters could be useful towards allowing further precise control and selection of specific classes of atoms confined to thin cells, and especially in preferentially selecting atoms close to walls. This kind of selectivity may be useful for atom-surface studies.

6.2.2 Coherent dynamics

Another notable aim for many experiments is to observe coherent dynamics in the form of Rabi oscillations. Indeed preliminary data in reference [37]

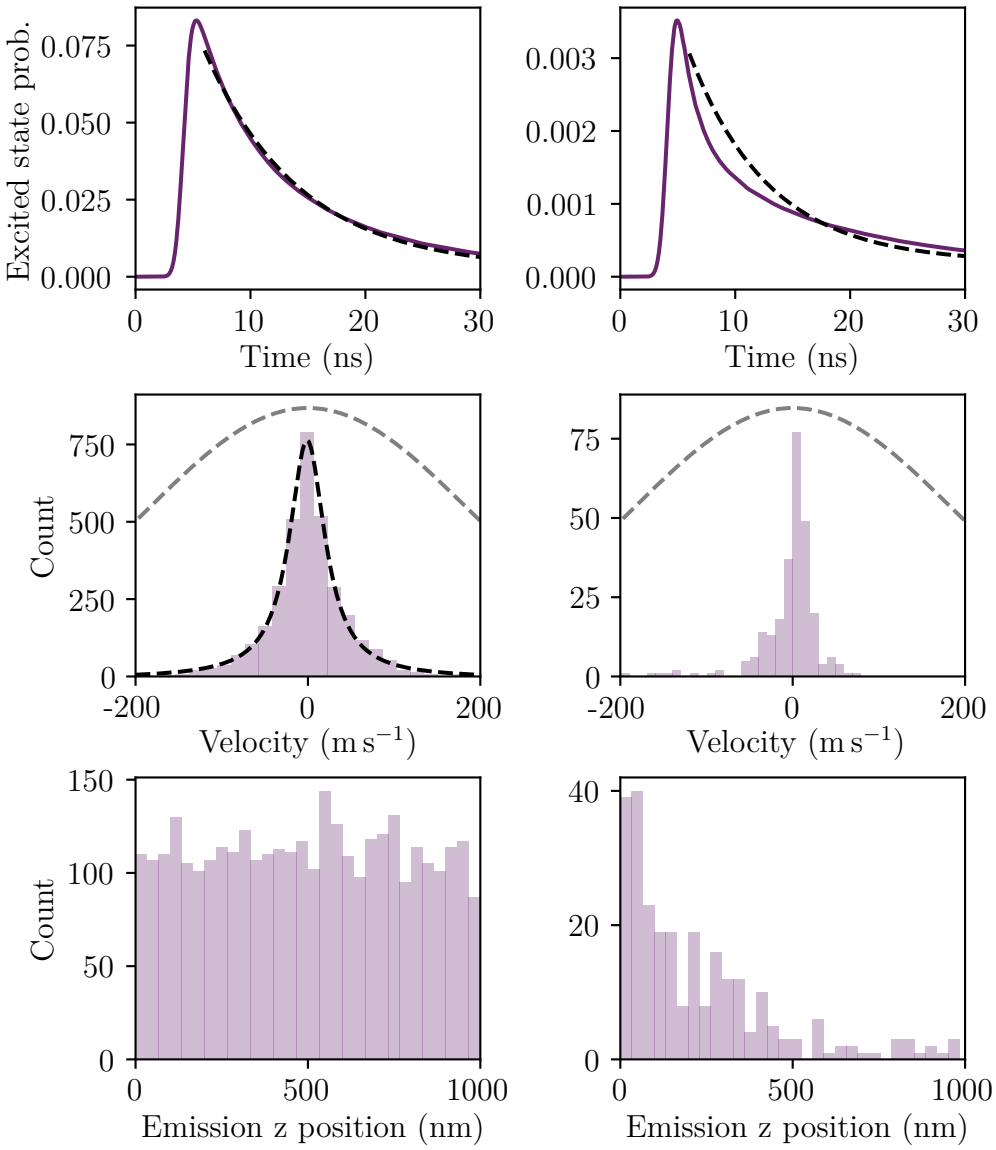

Figure 6.2: Comparison between simulations for the case of a transmitted excitation laser (left), and a TIRF geometry with an exponentially decaying field (right). Simulations were initialised with 10^5 random atoms distributed across a 1 µm cell. **Top:** Excited state probability after a 1.5 ns excitation pulse with a peak Rabi frequency of 100 MHz (modelled as a Gaussian with a peak at 4 ns). For the transmitted case, the decay is approximately exponential (dashed fit), but for the case of TIRF this is not a good fit. **Middle:** Velocity distribution of atoms which contributed to fluorescence. A Lorentzian fit is shown to the left plot, which yields a FWHM of 11 m s^{-1}. The Maxwell-Boltzmann starting velocity distribution is shown for comparison (grey dashed). **Bottom:** Position of atoms within the cell at the time they underwent a quantum jump.

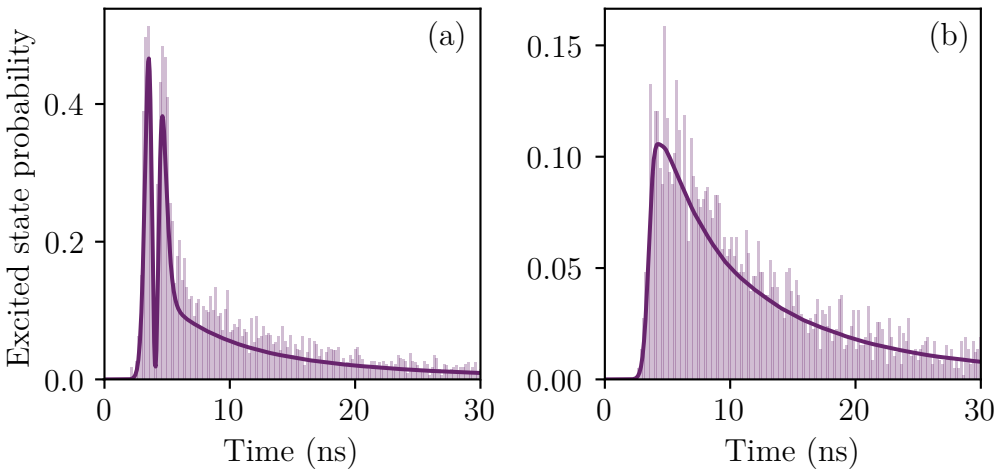

Figure 6.3: Quantum jump simulations for two different regimes: **(a)** a uniform intensity excitation region; **(b)** an excitation region with exponentially-decaying intensity, which is analogous to the evanescent excitation region imposed during a TIRF experiment. The excited state probability is plotted (purple line) alongside the histogram of spontaneous decay events (purple bars). This illustrates that decay events follow the excited state population trend as expected. Note the Rabi oscillation observed in (a) but absent in (b). Both simulations were run with 10^5 starting two-level atoms, a peak pulse Rabi frequency of 1 GHz and a pulse width of 1.5 ns, and with a cell temperature of 100 °C. The pulse was modelled as a Gaussian with a peak at 4 ns.

suggests it may be possible to observe such oscillations even in a thermal vapour confined to a nano-cell. Our simulations help to illustrate the regime necessary to observe such effects. As a simple test, we set the peak pulse Rabi frequency to 1 GHz (so that dynamics are observable over timescales on the order of 1 ns), and ran the simulations for the case of uniform intensity illumination, and for an exponentially-decaying intensity.

The results of our simulations are shown in Fig. 6.3, where it can clearly be seen that the simple addition of averaging over an exponentially-decaying field has the effect of washing out any Rabi oscillations which would be clearly visible in the uniform illumination case. Thus our simulations can be used to set limits on the intensity uniformity needed to see oscillations, further illustrating the usefulness of the quantum jump methodology. Similarly, even without an evanescently-decaying field, experiments commonly use a laser spot with a Gaussian intensity distribution, which amounts to a similar distribution of Rabi frequencies experienced by the atoms. Averaging over this

distribution has the same effect as shown above, washing out any observable coherent dynamics.

6.2.3 Detuning dependence

Whilst potential experiments are envisaged to use resonant pulsed excitation light, it is interesting to expand our simulations to mapping out the detuning dependence of the excitation dynamics. This allows us to, for example, test whether an experimental laser drift from resonance would considerably impact results. Furthermore, due to the Doppler shift induced by atomic motion, in a conventional bulk vapour cell scanning a laser across a range of detuning values excites a range of different velocity classes (which in conventional spectroscopy leads to a Doppler-broadened feature). However, it is useful to map out the relative spectral contributions from different velocity classes in a nano-cell, where the atoms with non-zero velocities perpendicular to the cell walls (which would conventionally contribute to the wings of the Doppler-broadened feature) now contribute proportionally less to the overall signal due to quenching collisions with the cell walls.

We ran our two-level atom simulations with 10^5 starting atoms at several discrete detuning values, yielding an excitation and decay curve for each (similar to those shown in e.g. Fig. 6.1 and Fig. B.1). We then calculated the area under each of these curves, as a measure of the excited state population. This is shown as a function of detuning for various cell thicknesses in Fig. 6.4.

As can be seen in Fig. 6.4, the spectral width of the features for all cell thicknesses is considerably larger than the conventional Doppler width for room-temperature rubidium of 0.5 GHz [22]. This is because we are using high excitation Rabi frequencies, leading to considerable power broadening (see, for example, [92]). There are several reasons for using such high powers. Firstly, the considerable broadening makes the system less sensitive to deviations in laser frequency and less sensitive to specific velocity groups. Secondly, the high laser intensity will lead to high levels of excitation, yielding larger experimental signals. Thirdly, to be able to perform some experiments, it is advantageous to be able to perform operations quickly. For example, to be able to perform a full Rabi cycle before a thermal atom has moved a distance of the order of a wavelength, and to mitigate problems with motional dephasing and atomic movement outside of the excitation volume or into

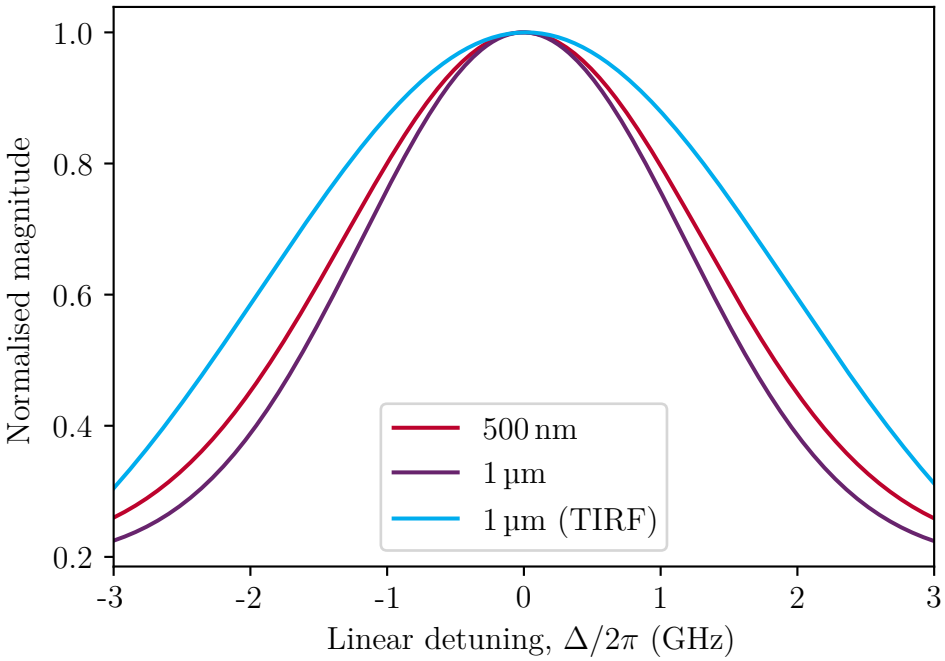

Figure 6.4: Results of quantum jump simulations for a range of detunings, illustrating the spectral widths obtained for the cases of confinement of 1 µm (purple) and 500 nm (red), and the case of a TIRF evanescent excitation region with a 1/e lengthscale of 100 nm in a 1 µm cell (blue). Simulations were run for 20 discrete detuning values, each with 10^5 starting atoms, and the area under the excited state probability curve was recorded. The trend of area against detuning for each case was fitted with a Gaussian line-shape to produce the curves shown here. All curves are normalised to have a peak height of 1.

a wall. This is another benefit of our thin cells, in that very high Rabi frequencies of order GHz can be achieved at relatively low laser powers using high-NA objectives, and can be interfaced with our atomic ensemble without averaging in the direction parallel to the laser beam (as our cell length can be shorter than the Rayleigh range). Note that in a thin cell we will still average over the Gaussian intensity distribution, unless different optics are used for the collection and excitation pathways or the cell has sub-micron confinement in more than one dimension.

We note that the curves for the nano-cell thicknesses (500 nm and 1 µm) are narrower than for atoms in a bulk cell subjected to the same intensity field, which is to be expected. The process of power broadening involves saturation of atomic velocity classes firstly close to zero perpendicular velocity (v_z, in the direction of laser propagation and perpendicular to the cell walls),

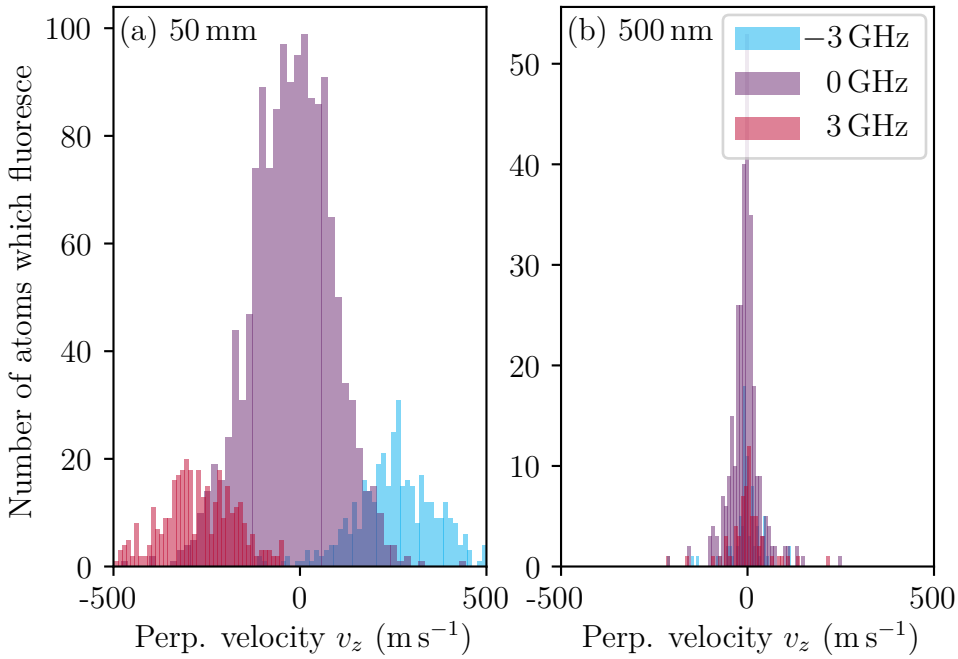

Figure 6.5: Results of quantum jump simulations showing the numbers of atoms which contribute to fluorescence signals as a function of perpendicular velocity (v_z) for three different values of linear detuning ($\Delta/2\pi = -3, 0, 3$ GHz), for the cases of **(a)** a 50 mm bulk cell, and **(b)** a 500 nm thin cell. Each simulation was performed with a discrete value of laser detuning, and was initialised with 10^5 starting atoms with a Maxwell-Boltzmann distribution of velocities.

with velocity classes of atoms further from $v_z = 0\,\mathrm{m\,s^{-1}}$ contributing to the spectral feature at larger detuning values and thus in the wings of the lineshape. Whilst these atoms contribute proportionally more to signals in the power-broadening dominated case than in the standard Doppler-broadened case, we also know that these atoms contribute proportionally less in a thin cell. This is due to the well-known velocity selectivity imposed by the cell wall confinement as described throughout this section. We observe that the curve shown in Fig. 6.4 for a 1 µm cell is slightly narrower than for a 500 nm cell, and attribute this to the extra transit time broadening in the thinner cell case. The same explanation holds true for the TIRF curve, where the 100 nm evanescent field extent imposes even greater transit time broadening. Simulations such as these provide greater understanding of the complex interplay between the effects of transit time broadening, power broadening, and Dicke narrowing as we have shown here.

We can also go further and extract which atomic velocity classes contrib-

uted to fluorescence signals for a given detuning. The results of this are shown in Fig. 6.5, comparing the response of a bulk cell (a) to that of a thin cell (b). For the bulk cell, as expected we observe that at non-zero detunings, the relevant velocity classes are non-zero, and shifted onto resonance by the Doppler effect. However, the thin cell results are in stark contrast to this. We observe that in a thin cell, regardless of the detuning of the laser beam, the velocity classes that contribute are centred around zero. This is due to the velocity selective nature of thin cells, whereby the faster velocity classes which would, in a bulk cell, contribute to the signals for non-zero detuning now hit the cell walls more quickly than they can fluoresce and contribute. The velocity classes that contribute are also much narrower in the thin cell case, for the same reason.

Note that our simulations for both the bulk and thin cell shown in Fig. 6.5 are for a power-broadened line-shape with a width as shown in Fig. 6.4. Thus at $\pm 3\,\mathrm{GHz}$, there is still a significant absorption or fluorescence signal. However, the question of which atoms contribute to a signal further from resonance even in a bulk cell is not trivial, and is discussed in detail by Hughes in [173].

6.2.4 Conclusion

In this section we have shown the versatility and usefulness of the quantum jump method for computationally simulating the behaviour of an atomic ensemble confined to a thin cell. We have shown that velocity selectivity can impact the observed emission dynamics of the ensemble, as well as investigating the impacts of different beam geometries. Having simulated these situations in detail and gained greater understanding of the underlying processes, we will move on in the rest of this chapter to performing experiments and comparing their results to our simulations.

6.3 Single-colour pulsed excitation

Our experimentation will begin with the simple case of using a single resonant pulsed laser to excite atoms confined to the nano-cell. This allows for simple tests of the excitation dynamics and measurements of the effective excited state lifetime of our atoms, which we will study by recording the fluorescence

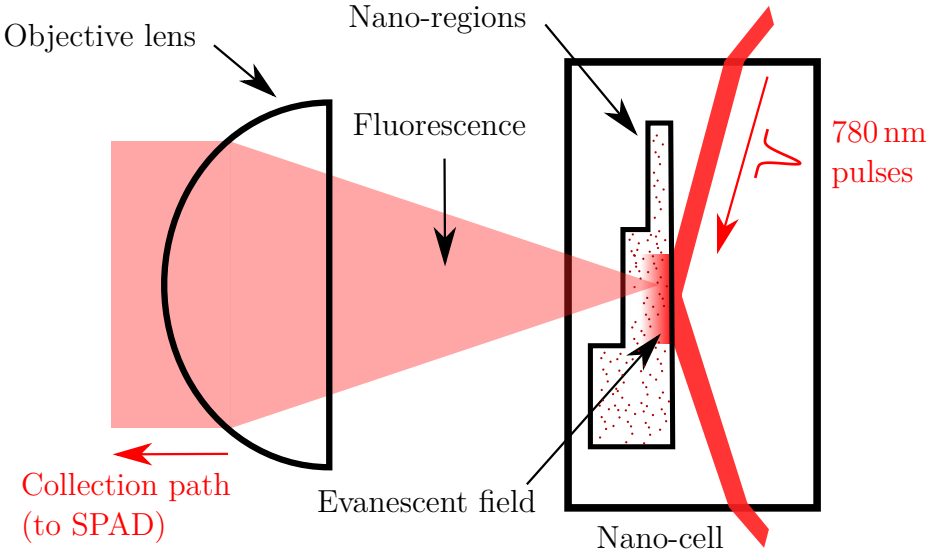

Figure 6.6: Experimental setup schematic (not to scale) for single-colour pulsed excitation in a nano-cell. A 780 nm laser with 1.5 ns pulses at a repetition rate of 1 MHz was incident on the back face of the nano-regions (focused to a spot size of order 100 µm at this location). This laser was resonant with the ^{85}Rb D2 $5S_{1/2} \rightarrow 5P_{3/2}$ ($F = 3 \rightarrow F' = 4$) transition. This incident beam undergoes total internal reflection, producing an evanescent field in the vapour region. Atomic fluorescence at 780 nm was collected by an objective lens (which was either an $f = 2$ mm or $f = 30$ mm lens depending on the desired collection volume), and was passed through a 780 nm bandpass filter before being coupled into a fibre and onto a single photon avalanche diode (SPAD).

activity of the atoms after a pulse event.

6.3.1 Experimental methods

For this work, we again used our nano-structured alkali metal vapour cell (nano-cell), constructed in-house using the methodology explained in detail in [1] and discussed further in chapter 3. Confinement regions with thicknesses ranging from 500 nm to 2 µm in one and two spatial dimensions were used for experimentation.

The experimental setup is shown in Fig. 6.6. For this single-colour excitation scheme, a single 780 nm laser with 1.5 ns pulses at a repetition rate of 1 MHz, resonant with the ^{85}Rb D2 $5S_{1/2} \rightarrow 5P_{3/2}$ ($F = 3 \rightarrow F' = 4$) transition, was incident on the nano-region of interest. The pulses were produced

using an Aerodiode SOM-std fibre optic modulator, seeded by a resonant CW 780 nm laser source (stabilised on resonance using the methodology outlined in appendix A.1). Atomic fluorescence photons at 780 nm were collected via the objective lens and recorded on a single-photon avalanche diode (SPAD). The 780 nm laser was incident on the back face of the cell in a total internal reflection geometry, producing an evanescent field in the vapour as explained in [1]. Fluorescence photon counts were recorded over many pulse events to build up a histogram of the overall fluorescence activity profile relative to the time elapsed after a pulse trigger. This repetition was necessary to mitigate the impact of the dead-time of the detectors and the low count rates observed (down to of order 0.001 counts per repetition for some of the experiments in this chapter). The experiment was run at a 1 MHz repetition rate, and collection times for the results shown in this work varied from the order of minutes to hours depending on the laser powers used.

6.3.2 Fluorescence dynamics

We measured the temporal dynamics of the atomic fluorescence activity of the ensemble under pulsed excitation by building up a histogram of count rate versus time (since a pulse trigger) over many subsequent pulse events. In this section we will discuss and analyse in detail the features of the resulting fluorescence activity curve, an example of which is shown in Fig. 6.7. Here we observed a sharp turn on in activity on a similar timescale to the pulse itself. The fluorescence activity subsequently decayed. This decay was empirically fitted to a sum of two exponentials (with additional sinusoidal components which will be discussed later), yielding 1/e lifetimes of $\tau_1 = 3.8(2)$ ns and $\tau_2 = 11.0(2)$ ns. We observe stochastic residuals, indicating our empirical fit curve is a good fit to the data. The reduced chi squared value for this fit was $\chi^2_\nu = 1.3$, further indicating a good fit [167].

To model the decay timescale for this dataset, we first employed a simpler simulation than the quantum jump simulations discussed in the previous section. We began with 10^5 simulation atoms, with velocities selected at random from a Maxwell-Boltzmann distribution and positioned at random across the cell. We then calculated the time at which each atom collided with a cell wall, and thus mapped out the population reduction in the region of interest over time. We then multiplied this decaying population function with an ex-

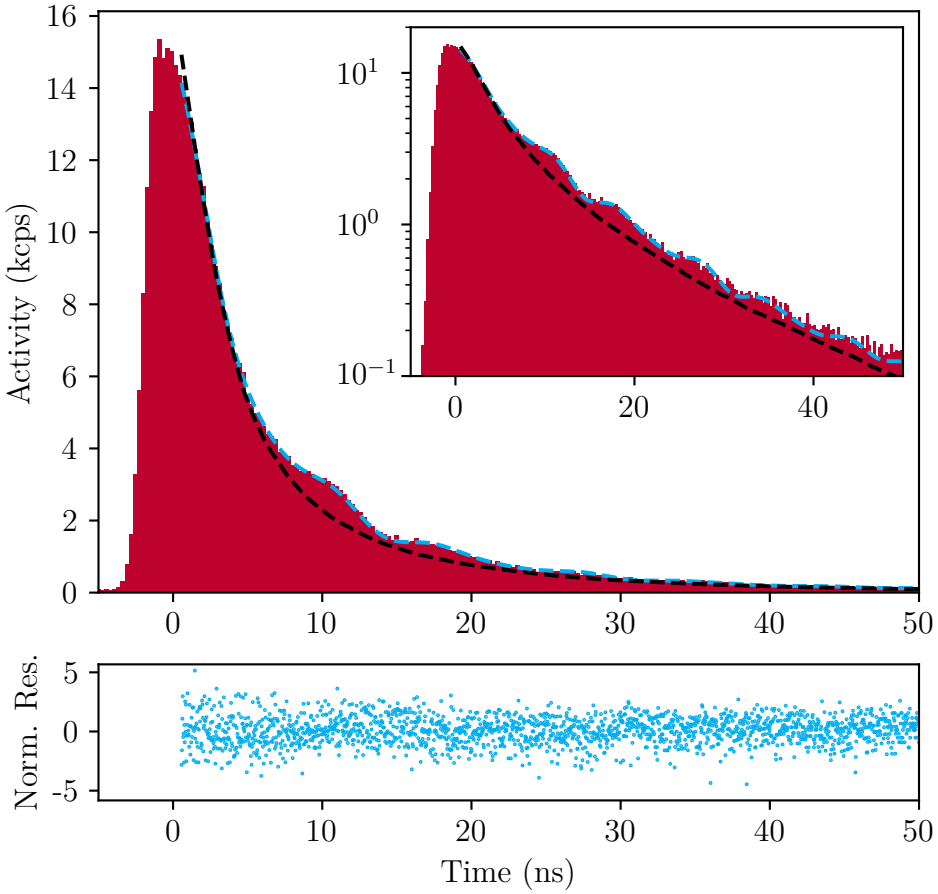

Figure 6.7: Fluorescence activity at 780 nm (red) from a 1 µm thick cell under excitation by 1.5 ns resonant 780 nm laser pulses. Also shown is a simple simulation based on the decay lifetime of the $5P_{3/2}$ state and the 'lifetime' of the atomic ensemble due to wall collisions (black dashed line), and an empirical fit (blue dashed line). The empirical fit is the sum of two exponential decay curves multiplied by a sinusoidally-oscillating curve (modelling quantum beats), and the normalised residuals from this fit are shown below. The fit assumes Poissonian statistics for the number of counts. Inset is the same plot on a logarithmic scale. For the experimental data, the peak 780 nm pulse power was 30 µW with a focal spot size of 100 µm, and the cell temperature was 100 °C. The 1/e decay timescales extracted from the empirical fit are $\tau_1 = 3.8(2)$ ns and $\tau_2 = 11.0(2)$ ns. The oscillations observed in the experimental data are considered to be quantum beats due to the hyperfine structure of the rubidium $5P_{3/2}$ state (where the hyperfine level spacings are less than the bandwidth of the laser pulse), which was not considered in the simulation. The zero point of the time axis is chosen to be at the peak of the activity curve.

ponential decay with a 26 ns (1/e) lifetime, modelling the conventional decay of atoms from the $5P_{3/2}$ state. The results of this simulation are shown (black

dashed line) alongside the experimental data in Fig. 6.7, and give a reasonable agreement with the experimental data. We also found that a similarly good agreement was achievable using the same model and comparing to data from a 2 µm thickness cell. We thus conclude that the ensemble behaves largely as if all the atoms were excited and thus the timescales observed in the fluorescence activity decay depend mostly on two parameters: cell thickness and excited state lifetime.

For comparison, a quantum jump simulation performed in the same way as described in the previous section for the experimental parameters used here yields a double-exponential with decay timescales of $\tau_1 = 4.2\,\text{ns}$ and $\tau_2 = 13.5\,\text{ns}$. These are similar to the values given by the empirical fit to the dataset in Fig. 6.7 ($\tau_1 = 3.8(2)\,\text{ns}$ and $\tau_2 = 11.0(2)\,\text{ns}$), however do not agree within error. Despite this, the two types of simulation shown do reproduce qualitatively the reduction in fluorescence lifetime shown in the experimental data for a thin cell as compared to a bulk cell. This agreement is notable given the simplicity of both models, which do not include details such as the hyperfine states, atom-atom collisions, surface roughness, multiple scattering events, or atom-wall interactions. In the case of the simpler model, even new atoms entering the system from the cell walls and outside the excitation volume as well as the Gaussian laser spot and the excitation pulse shape are not considered. It is likely that a combination of such factors accounts for the small discrepancies in timescales between the simulations and the experimental data. It is also worth noting that the 'simpler' simulation described here only models the decay timescale for the atomic fluorescence, and cannot be used to study the full dynamics of the excitation and emission process in the same way that the full quantum jump simulations can.

The decay timescales measured in this study are significantly reduced from the 26 ns lifetime of the excited $5P_{3/2}$ state (which would be expected from a measurement in a conventional vapour cell), showing the influence of the confinement on the decay dynamics. However, conversely it also illustrates how a proportion of the atoms survive well beyond the few nanoseconds that the average atom would take to collide with a cell wall. One could envision that these 'slow' atoms could be 'selected' in this way, for example by simply waiting a given time after a pulse event or using a second pulse, temporally offset from the first, to excite the narrower velocity class of excited atoms to a higher-lying state. This would allow the study of dynamics of only the

chosen population. As a first step to this end, in the section 6.5 we will study a more complex excitation setup using two lasers to excite atoms to the $5D_{5/2}$ state.

We observed oscillations on the approximately 10 ns timescale in the decaying part of the experimental data presented in Fig 6.7. Our input laser was frequency-stabilised to the ^{85}Rb $5S_{1/2} \rightarrow 5P_{3/2}$ $F = 3 \rightarrow F' = 4$ transition, however we propose that the oscillations observed were due to quantum beating with the nearby hyperfine levels $F' = 3$ and $F' = 2$. Our pulse width is only 1.5 ns and thus has a bandwidth of order 700 MHz. The $F' = 3$ and $F' = 2$ levels lie only 120 MHz and 183 MHz away from the $F' = 4$ level, respectively. To test our hypothesis of quantum beats, we empirically fitted an exponential decay multiplied by two sinusoidal functions with periodicity corresponding to these two hyperfine splittings (shown as a blue dashed line in Fig. 6.7). From this fit we found that the magnitude of the contribution from the further away $F' = 2$ hyperfine level was six times less than that from the $F' = 3$ level. As shown in the lower plot of Fig. 6.7, we observed stochastic residuals, suggesting our empirical fit describes these oscillations well. The fit also has a reduced chi squared value $\chi^2_\nu = 1.3$, indicative of a good fit [167]. Thus we conclude that the oscillations we observe are indeed quantum beats.

We can also compare our work to that presented by Keaveney in [37]. In his study, Keaveney suggested that the lifetime of the state varied linearly with cell thickness, with a trend $\tau \sim l/u$. Here τ is the 1/e decay lifetime, l is the cell length, and $u \approx 300\,\mathrm{m\,s^{-1}}$ is the most probable thermal velocity of the atoms. In comparison, we find that our data better fits to the sum of two exponential decays than a single exponential. The shorter of these ($\tau = 3.8(2)$ ns for a 1 µm cell, and $\tau = 6.9(2)$ ns for a 2 µm cell) are not dissimilar to the trend observed by Keaveney, though do not agree within error. However, we also observed a longer second decay timescale ($\tau = 11.0(2)$ ns for a 1 µm cell, and $\tau = 16.60(10)$ ns for a 2 µm cell) which is not alluded to in the work of Keaveney. Results from our simulations also fit better to a double exponential decay curve than a single exponential decay, adding weight to the conclusion that the fitting of a double exponential to our experimental data is valid. The experimental setups used in both our study and that of Keaveney were fundamentally similar, with similarly short pulses and fluorescence-based detection methods. Differences lie in the type of cell used (fused silica cells

in the present work, Armenian sapphire nano-cells by Keaveney), as well as the specific experimental parameters such as laser power, pulse length, spot size, beam geometry, and cell temperature, which were used. The low signal-to-noise ratio due to the low repetition rate of the Keaveney experiment may have hampered the observation of the longer but lower magnitude decay 'tail', explaining why a double-exponential fit was not necessary. However, more work is required to understand the physical origin of the difference in timescales measured even for the shorter decay.

We can also compare our experimental results to more sophisticated quantum jump simulations, as discussed in section 6.2, and contrast this with the simple model shown (black dashed line) in Fig. 6.7. The simple model combines the atom-wall flight time with the excited state lifetime to produce remarkably good fits, and is fast to compute. However, it does not predict the full dynamics of the fluorescence activity over time, being unable to predict the excited state population dynamics during the laser pulse. Our Monte Carlo quantum jump simulations are more computationally intensive, requiring minutes to hours of computation time on a standard computer. However, these more sophisticated simulations can be used to predict the dynamics of the excited state population rise and fall including during the laser pulse. They also yield greater insights into the classes of atoms which contribute to fluorescence activity at a given time, as the trajectories of individual simulation atoms are recorded.

The comparison between the results of a quantum jump simulation and the 1 µm experimental data (which has already been presented in Fig. 6.7) are shown in Fig. 6.8. We observe good qualitative agreement between the simulation and the experiment, and reasonable quantitative agreement given the simplifications made in modelling (neglecting hyperfine levels and atom-atom collisions, for example). The rise time of the atomic fluorescence activity as the pulse is turned on is predicted with good accuracy, however the model over-estimates the atomic fluorescence expected at longer times after the pulse. This suggests the model expects more atoms to survive (relative to the numbers observed at short times) to longer times and fluoresce than we observe. It is possible that a simplification of our model becomes less valid in the longer timescale regime (e.g. when there has been more time for an atom-atom collision to have taken place). The discrepancy, however, is relatively small (as emphasised on a logarithmic scale, shown in the inset in

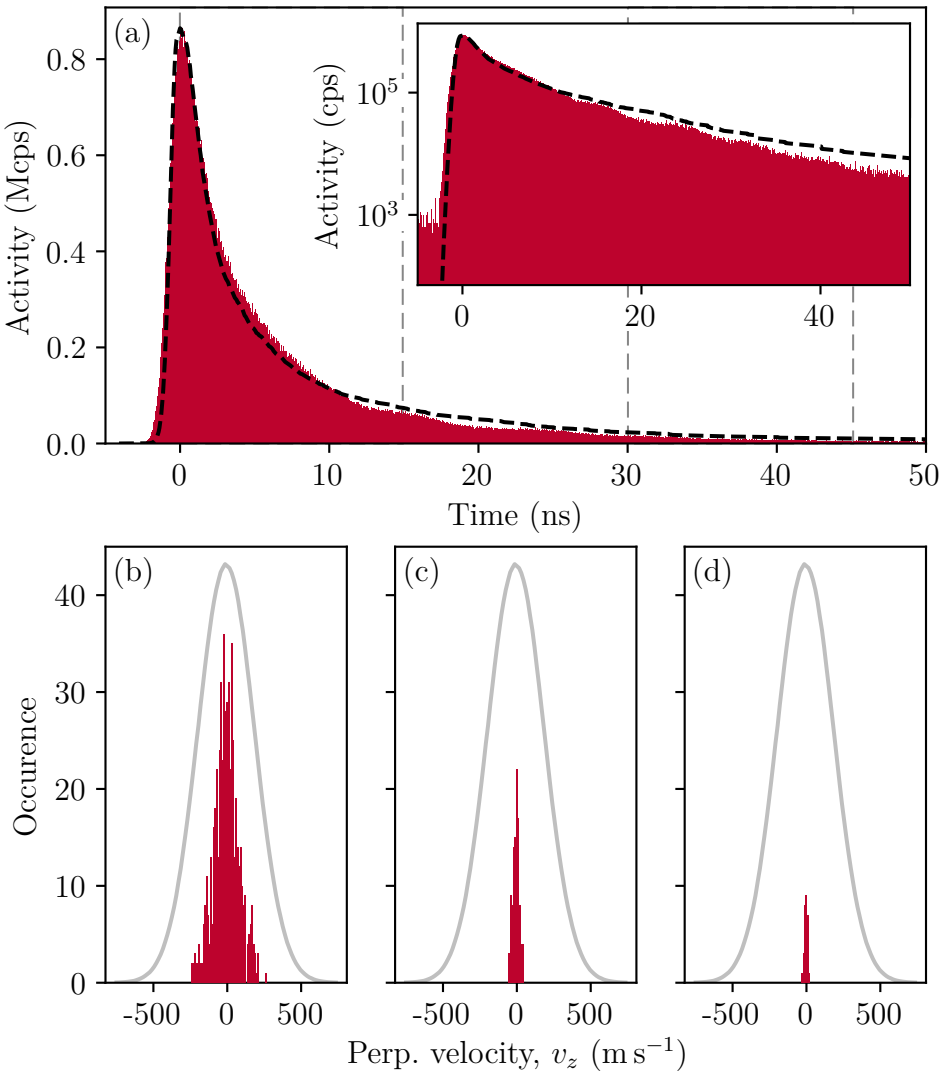

Figure 6.8: **(a)** Experimental fluorescence activity from a 1 µm cell (red histogram, as previously shown in Fig. 6.7) compared to quantum jump simulations (black dashed line) for the same parameters used in the experiment. Inset is the same plot on a logarithmic scale. Below are three graphs showing which atomic velocity classes (where velocity, v_z is perpendicular to the cell confinement direction) contribute to fluorescence activity at different time intervals in the simulation: **(b)** 0–15 ns; **(c)** 15–30 ns; **(d)** 30–45 ns. The boundaries between these intervals are indicated by the vertical grey lines in (a). A thermal Maxwell-Boltzmann distribution is shown for comparison (grey line).

Fig. 6.8), and thus we conclude that the model can still be used to give good predictions for experimental results.

Having verified the validity of our simulations by comparing their results

to experimental data above, we can move to extracting further information from our simulations which cannot be directly observed experimentally. In the lower plots of Fig. 6.8 the (simulated) perpendicular velocity (v_z) classes which contribute to fluorescence for three discrete time intervals are shown. We observe a considerable narrowing of the velocity classes which contribute at later times, owing to the faster velocity classes having collided with the cell walls before having chance to excite and subsequently fluoresce. Thus our combination of thin vapour cells and a pulsed excitation scheme gives velocity selectivity from a thermal atomic ensemble.

In further sections of this chapter we will go on to measure similar curves to that shown in Fig. 6.7 but for differing experimental parameters, to gain a greater insight into the fundamental physics of our system. Note that whilst we have discussed above that a double-exponential decay fit is better than a single-exponential for these datasets, for some future datasets presented in this work a single-exponential decay will be fitted. This is for simplicity where the signal-to-noise ratio is much lower, and is considered to be valid for comparisons between datasets given that the contribution of the longer of the two exponentials is proportionally less than the shorter one. For such datasets the quantum beats are also not discernible above the noise and so are also neglected from the fits.

6.3.3 Timing of pulse and fluorescence

Whilst we have now dealt with the temporal dynamics of the fluorescence activity, we have not yet considered the dynamics in relation to the arrival time of the input laser pulse. To study this, we can record one fluorescence activity measurement as described above, and then subsequently cool the cell to room temperature and record a second dataset in the same way. In the latter case at room temperature, the density of atoms will be reduced by almost three orders of magnitude as compared to a typical experimental cell temperature of 90 °C (see Fig. 1.1). Thus the atomic fluorescence activity will also be considerably reduced, leaving a much greater fraction of the activity detected by the SPAD being due to scattered laser light from the input pulse (which is scattered by, for example, cell surfaces and defects). Thus our measured activity now maps out the pulse shape rather than the atomic fluorescence dynamics. With all other experimental parameters remaining

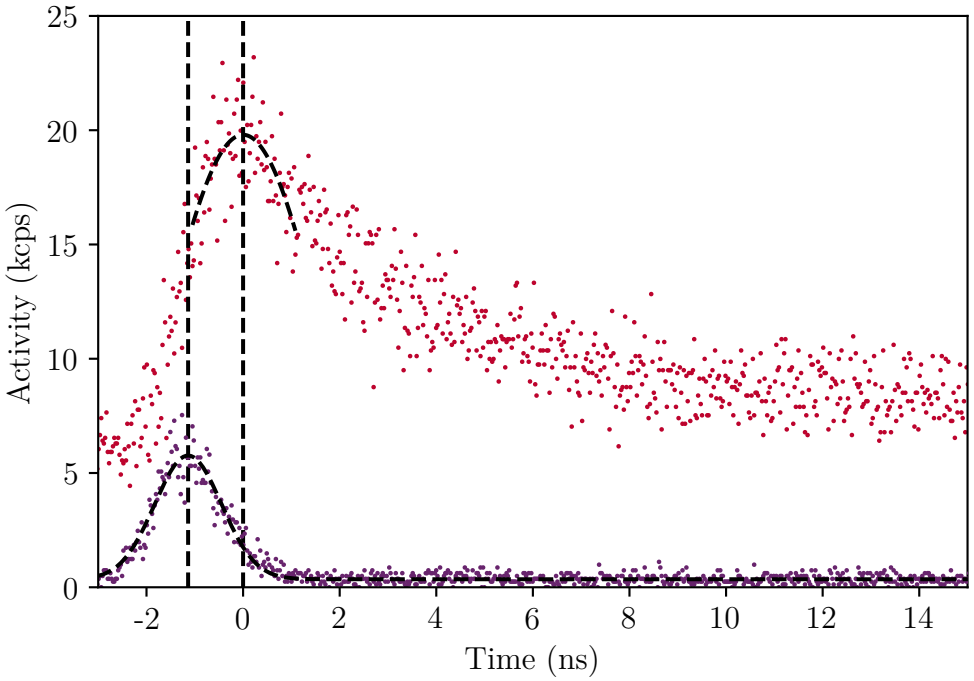

Figure 6.9: Graph illustrating the time delay between the excitation pulse and the subsequent atomic fluorescence activity rise. This experiment was done in a 1 µm thickness cell using a TIRF geometry, as for previous experiments in this section. For the fluorescence activity curve (red) the cell was held at 90 °C. The pulse arrival time was measured with the same setup but at room temperature, such that the atomic density in the cell was low and thus measured counts on the detectors were largely due to scattered laser light from cell surfaces. The pulse curve is shown in purple. A Gaussian was fitted to the pulse and to the peak of the fluorescence data (black dashed lines). As emphasised by the vertical dashed lines, the time delay between the peaks of the two curves was measured to be 1.14(4) ns. The Gaussian fit to the pulse yields a FWHM of 1.630(13) ns. The peak pulse power for this dataset was 500 µW, which gave a peak Rabi frequency of 0.9 GHz (calculated as described in section 2.2).

the same between the two measurements, we can use this method to directly compare the arrival time of the pulse at the location of the atoms and the turn-on dynamics of the atomic fluorescence.

An example measurement is shown in Fig. 6.9. By fitting a Gaussian line-shape to both the pulse and the top part of the fluorescence curve (as shown), we can find the locations of the peak of each. We see that for this pulse, with peak Rabi frequency of 0.9 GHz, we had a 1.14(4) ns time delay between the peak pulse intensity and the subsequent peak in atomic fluores-

cence. We believe that for this 'two-level' case with a single 780 nm excitation laser, the rise time is related to the reciprocal of the Rabi frequency, as this sets the rate at which atoms are excited to the $5P_{3/2}$ state. Our quantum jump simulations predict a 1 ns delay between the pulse peak and the peak fluorescence for the same input parameters as used in this experiment. This is reasonable agreement with the experimental data and adds weight to the claim that the simulations can be used to accurately predict the atomic ensemble behaviour. Such excitation dynamics can be mapped out using the quantum jump method but not the 'simple' simulations described in the previous section (as these only model emission decay timescales and not the full absorption and emission process).

6.3.4 Density dependence of fluorescence decay

Another parameter of interest in any thermal vapours experiment is density, which is generally varied by varying cell temperature (as described in chapter 1). We thus decided to study the dynamics of the atomic fluorescence activity as we have above, but whilst varying the cell temperature. For each temperature we recorded a curve similar to that shown in Fig. 6.7, and fitted this with a double exponential decay. The results of this fitting for all datasets are shown in Fig. 6.10. No clear trend was observed in the shorter fitted decay timescale with density, with a negligible variation over 0.3 ns. However, there is a clear negative trend in the longer timescale with increasing activity, with a variation in decay constant of 4 ns over the range studied. We postulate that this may be the result of collective effects becoming more dominant at higher densities, and having more impact on the system dynamics. Collective effects will have less impact for the fast atoms which dephase and hit the walls quickly, hence why the shorter decay timescale shows little variation but the longer timescale does.

We note that we have chosen total activity as the parameter which most closely relates to atomic density in the region of interest, rather than temperature. This is because we believe that due to diffusion timescales in the nano-cell, the number density of atoms in the vapour phase can deviate from the standard vapour pressure-temperature equations. This effect is described in section 3.4. We observed at the highest temperatures studied the total activity began to reduce, suggesting the nano-regions were depleting of ru-

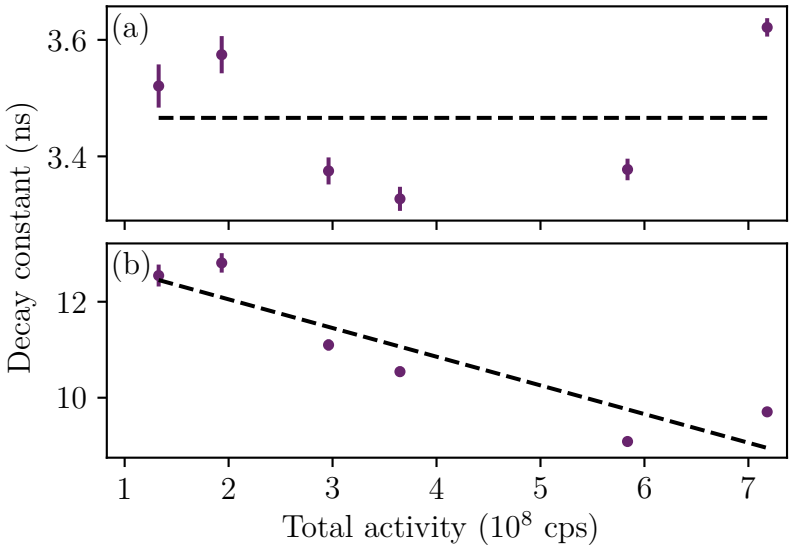

Figure 6.10: Plots showing fitted fluorescence decay timescales against total fluorescence activity. For this experiment, a 1 µm cell thickness was used, with a resonant 1.5 ns excitation pulse in the TIRF geometry. Each datapoint represents one experimental run at a fixed temperature, which produced a curve similar to that shown in Fig. 6.7. To this curve, the sum of two exponential decays (plus quantum beats) was fitted, and it is these fitted 1/e decay timescales that are plotted here. We believe total activity to be a better relative measure of atomic density than temperature in our nano-cells, and thus this was chosen as the appropriate x-axis unit. Also note the difference in scale of the y-axes between (a) and (b). We observe that the shorter timescale (a) varies in a stochastic manner with no discernible trend. However, the longer timescale (b) has a clear negative trend with increasing total activity (and thus increasing atomic density).

bidium vapour. Changing the parameter of interest to total activity from temperature made the trend in Fig. 6.10 much clearer.

For context, the temperature range used to achieve the activity (and thus density) range in Fig. 6.10 was 125–185 °C. Whilst we have discussed above that we are unlikely to have the conventional mapping from temperature to density described by the steady-state vapour-pressure equations (see Fig. 1.1), we can still use this as a crude order-of-magnitude estimate of the vapour densities and thus atomic spacings involved. This temperature range covers an approximate mean inter-atomic spacing variation between 200 nm and 70 nm, well within the sub-wavelength ($\lambda = 780$ nm) regime and even into the regime of below $\lambda/2\pi$ whereby collective behaviour becomes much more significant (see section 2.3.4).

6.4 Pulsed fluorescence photon statistics

Another method for understanding the nature of the atomic ensemble under resonant excitation is by studying the photon statistics of the emitted light. One metric is the the second order correlation function, which is a measure of the correlations between photons emitted by the system. This is defined as [174]

$$g^{(2)}(\tau) = \frac{\langle I(t)I(t+\tau)\rangle}{\langle I(t)\rangle^2} \tag{6.1}$$

for a light beam with intensity $I(t)$ and time delay between subsequent photons τ (and where $\langle . \rangle$ denotes the time average). A classical thermal source emits bunched light with $g^{(2)}(0) > 1$; a coherent source such as a laser gives $g^{(2)}(0) = 1$; whilst an ideal single-photon source such as a single emitter gives $g^{(2)}(0) = 0$. Previously, perfect bunching ($g^{(2)}(0) = 2$) has been observed in thermal atomic vapour systems [175]. However, some previous $g^{(2)}$ studies using thermal vapours have been impacted by multiple scattering events [176]. The frequency of such events should be reduced in a thin vapour confined to a nano-cell. One experimental study has previously dealt briefly with the photon statistics of a thermal ensemble of rubidium atoms confined to a nano-cell under excitation with CW laser light [82]. Theoretical studies have shed light on the potential availability of various photon statistics regimes in a disordered thermal vapour confined to a nano-cell [2,117], however such non-classical statistics have not been observed in previous works. To the author's knowledge, there has been no similar previous study of the photon statistics of a thermal atomic vapour under pulsed excitation.

Pulsed excitation has some potential key benefits over CW excitation for photon statistics measurements. For example, using short nanosecond pulses ensures all excited atoms were initialised into the excited state within the same time window. This should make for a cleaner system in which it is less likely that two observed photons are from two uncorrelated atoms that were excited at different times. Short (nanosecond) pulses are more likely to fully capture the atomic dynamics as they are shorter than the relevant decoherence timescales, such as the excited state lifetime (26 ns for the rubidium $5P_{3/2}$ state) and the wall-to-wall transit time (of order 3 ns for the average thermal atom in a 1 µm thick cell).

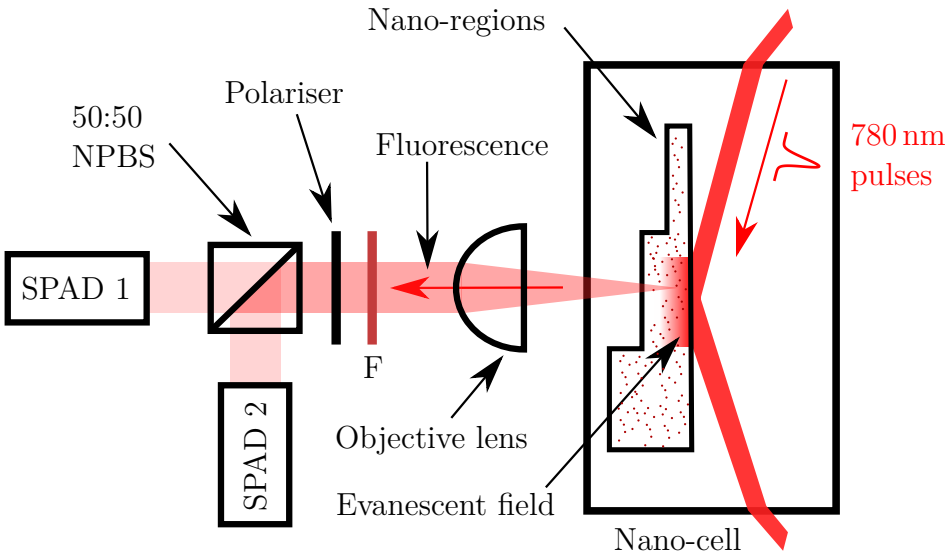

Figure 6.11: Experimental setup schematic (not to scale) for pulsed photon statistics ($g^{(2)}$) measurements in a nano-cell. Atoms confined to the nano-regions were excited by a pulsed 780 nm laser, resonant with the ^{85}Rb D2 $5S_{1/2} \rightarrow 5P_{3/2}$ ($F = 3 \rightarrow F' = 4$) transition, in a similar way to that shown in Fig. 6.6. The 780 nm atomic fluorescence produced was then passed through a 780 nm bandpass filter (F) and a polariser to select only one of the two orthogonal polarisation modes, and then collected by an objective lens and split 50:50 by a non-polarising beamsplitter (NPBS) onto two SPADs. The correlation between the photon detection times on each of the two SPADs was analysed on a computer, yielding our $g^{(2)}$ measurement.

6.4.1 Experimental methods

In this section we use the conventional Hanbury Brown-Twiss setup [177] for measuring the second order correlation function ($g^{(2)}(\tau)$) of the fluorescence from atoms confined to our nano-cell. The setup is shown in Fig. 6.11. By studying the rate of coincidences (the observation of one photon on each detector with a given time delay, τ), we can deduce whether the emitted photons have super- or sub-Poissonian statistics (i.e. the light is bunched or anti-bunched).

Whilst in the CW case one can simply study the peak at $\tau = 0$ (accounting for time delays due to the electronics of the detection setup), in the pulsed case we observe a peak in coincidences at intervals described by $\tau = nT$, where T is the period between excitation pulses and n is an integer. This is due to a peak in fluorescence activity occurring after each pulse event, and

subsequently decaying away over the course of the effective atomic lifetime (as measured in previous sections). Thus we have not chosen to plot $g^{(2)}(\tau)$ in this section, but to illustrate this by plotting the occurrence of a photon on each detector with various delay time (τ) bins. By comparing the height of the $\tau = 0$ peak (which relates to coincidences during a single pulse event) with subsequent $\tau = nT$ peaks, one can deduce the value of $g^{(2)}(0)$. This is because photons within one peak can be correlated with each other, but not with photons in a subsequent peak. For example, a peak at $\tau = 0$ which is taller than subsequent peaks indicates bunching, whilst a shorter peak indicates anti-bunching. As a simple test, we inputted a small amount of pulsed laser light directly into the HBT setup, which yielded an initial peak at $\tau = 0$ which was the same height (within error) as the mean of the subsequent peaks. This data is shown in Fig. 6.12. For laser light we have $g^{(2)}(0) = 1$, so the data agrees with the theory and verifies our method for this test case.

6.4.2 Results and discussion

An example nano-cell photon statistics dataset is shown in Fig. 6.13, using a single-colour excitation scheme in the TIRF geometry (the same scheme as was used in section 6.3). Here we observe a peak in occurrences of two photons with close to zero time delay on both detectors (around $\tau = 0$) which is taller than subsequent peaks, indicating bunching. By normalising the data by the height of the subsequent peaks and fitting a double-exponential decay to the feature, we measure the value $g^{(2)}(0) = 1.312(13)$. This is a signature of classical bunching and is generally observed from thermal light sources. The value of $g^{(2)}(0)$ is consistent with previous CW $g^{(2)}(0)$ measurements [82], which showed similar values for this cell temperature with some variation dependent on the excitation Rabi frequency. However, the cited work measured a variation with temperature that was not observed in the current work. In this investigation we observed a stochastic variation in $g^{(2)}(0)$ values between 1.25 and 1.35 across a temperature range of 90–170 °C, suggesting a lack of strong temperature (and thus density) dependence. One might logically expect a variation in $g^{(2)}(\tau)$ curve for different density regimes: at low enough densities one could expect single atom behaviour, giving antibunching, whilst at high densities collective effects may alter the decay timescale and height

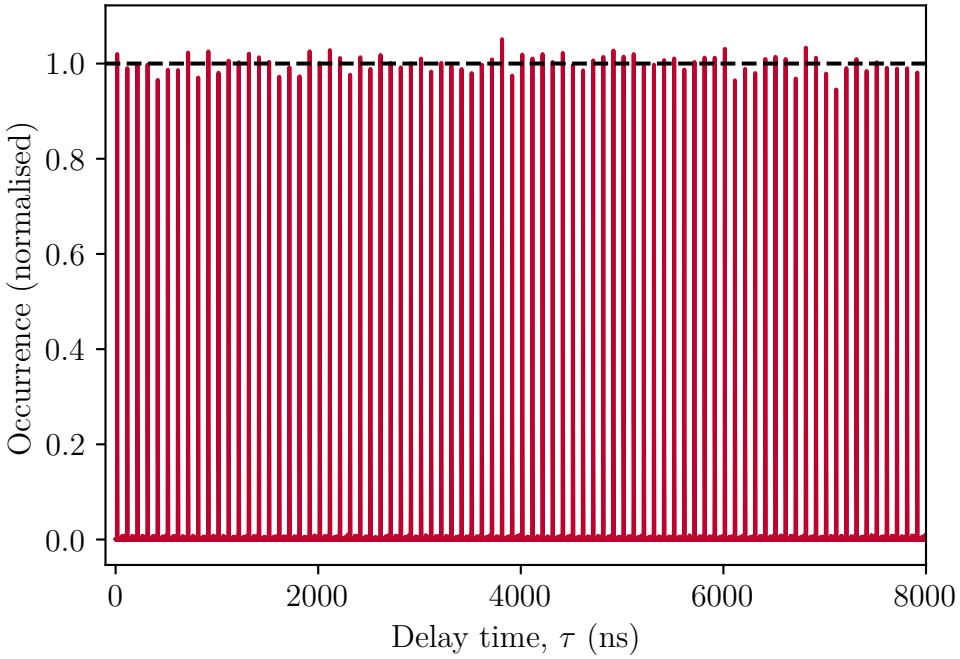

Figure 6.12: Occurrence of delay times τ between photon arrivals on two detectors (red), for pulsed laser light. Photons were recorded using a Hanbury Brown-Twiss setup. The y-axis is normalised by the mean height of all peaks excluding the first. The height of the first peak (i.e. number of coincidence events with no delay between the two detectors) relative to the other peaks (which are spaced by the pulse repetition rate) gives a measure of $g^{(2)}(0)$. The horizontal black dashed line at 1 is a guide to the eye. By fitting a Gaussian to the initial peak and accounting for the uncertainty in the mean peak height of the subsequent peaks, we find $g^{(2)}(0) = 1.02(3)$, in agreement with the expected value for laser light of $g^{(2)}(0) = 1$.

of the $g^{(2)}(\tau)$ peak. It is not clear why this study differs from the CW study in reference [82] in terms of density dependence, however further study could focus on broadening the temperature regimes investigated using the pulsed scheme.

We also note that the chosen double-exponential fit may under-estimate the peak value, $g^{(2)}(0)$. It is clear from Fig. 6.13(b) that the points around the peak all lie above the best-fit line, and do not vary stochastically around it. Thus we conclude that our chosen fit function may not be the perfect choice for this dataset, and that thus the quoted $g^{(2)}(0)$ value may be an underestimate. The datapoints at the very peak of the curve are at around 1.45. However, this is still classical bunched light and so our conclusions remain the same.

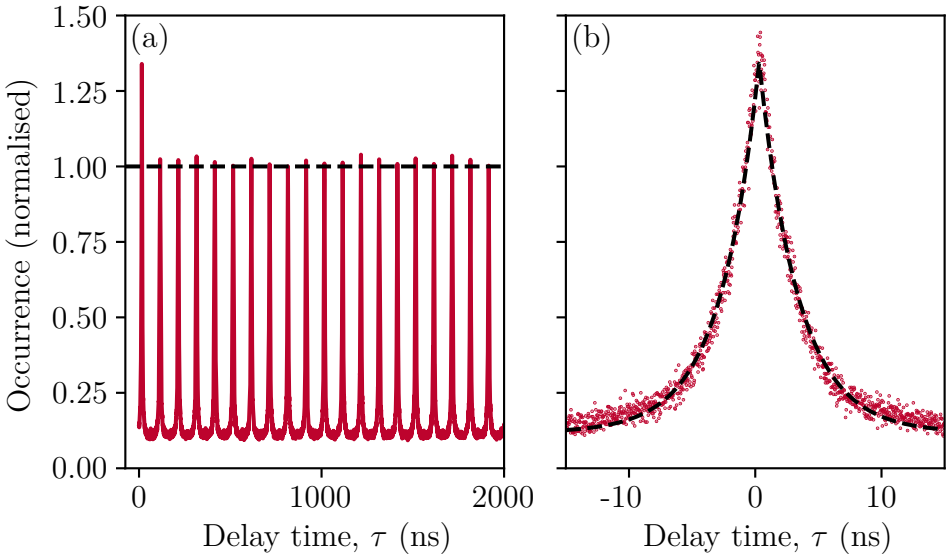

Figure 6.13: Measurement of the second order correlation function for pulsed laser light, illustrating our method. The occurrence of different delay times τ between photon arrivals on opposite detectors is plotted (red). The y-axis is normalised by the mean height of all peaks excluding the first. Photons were recorded using a Hanbury Brown-Twiss setup, for atoms confined to a 1 µm cell region at 150 °C, interacting with 780 nm Gaussian laser pulses with 1.7 ns FWHM, a repetition rate of 10 MHz, and a peak Rabi frequency of 0.9 GHz (calculated as discussed in section 2.2), in a TIRF geometry. **(a)** We observe regular peaks spaced by the repetition period of the excitation laser pulses, with the $\tau = 0$ peak being taller than subsequent peaks. This indicates bunching. **(b)** The $\tau = 0$ peak in detail, with a double-exponential fit (black dashed). This fit yields $g^{(2)}(0) = 1.312(13)$, and a 1/e decay timescale of 3.09(2) ns. Note that the data in (a) is more coarsely binned as compared to (b), and thus the initial peak height appears reduced.

We can also compare the timescale of the decay of the coincidence count rate with the timescale of fluorescence decay recorded on a single detector (the latter being measured in the same way as the results shown in Fig. 6.7). By fitting a simple exponential decay to each, we find a timescale of 3.09(2) ns for the coincidence rate, and 2.988(10) ns for the overall fluorescence activity. Whilst these values do not agree within their uncertainty, they are negligibly far apart, especially given that the maximum resolution of our photon counting is 26 ps. We postulated that collective effects may impact our measurements at higher densities, however we observed no trend in the coincidence decay rate with varying temperature. Indeed, the timescales measured from a single exponential decay fit show no trend, as was shown for the dominant

'short' timescale fits in Fig. 6.10.

6.5 Two-colour pulsed excitation

In the previous sections, we used only a single laser frequency to excite atoms confined to our nano-cell, and utilised fluorescence at the same frequency to measure their effective lifetime. As explained in chapter 5, to probe atoms and test their response in more complex geometries (such as nano-channels or nano-pockets, see chapter 3) we cannot use such simple excitation schemes without inducing considerable scattered laser light (and thus noise). As such, to enable pulsed measurements in more confined geometries, a more complex scheme was required. This scheme employed two lasers to excite atoms to a higher energy state, with a much longer lifetime than the 26 ns of the rubidium D2 transition used in the previous section. Thus we postulate that the velocity-selective dynamics of the excitation and emission process may also change, changing the effective lifetime from those which we measured above.

6.5.1 Experimental methods

The experimental methodology for two-colour pulsed excitation follows closely that already outlined for single-colour pulsed excitation in section 6.3.1, whilst the new two-colour excitation scheme has been described and deomonstrated previously in chapter 5. The modified setup is shown in Fig. 6.14. The key differences between this and the single-colour setup lie in the addition of a second laser beam and the choice of beam geometry. For this two-colour excitation scheme, a CW laser at 776 nm was added, which was frequency stabilised on resonance with the $5P_{3/2} \rightarrow 5D_{5/2}$ transition (using excited state polarisation spectroscopy as outlined in appendix A.2). Through this addition, atoms could be excited to the $5D_{5/2}$ state, from which there is approximately 7.5 % probability that they will decay via the $6P_{3/2}$ state and produce a 420 nm photon [75]. These 420 nm fluorescence photons were collected by the objective lens and recorded on a Hamamatsu H10682 photon-counting photomultiplier tube (PMT).

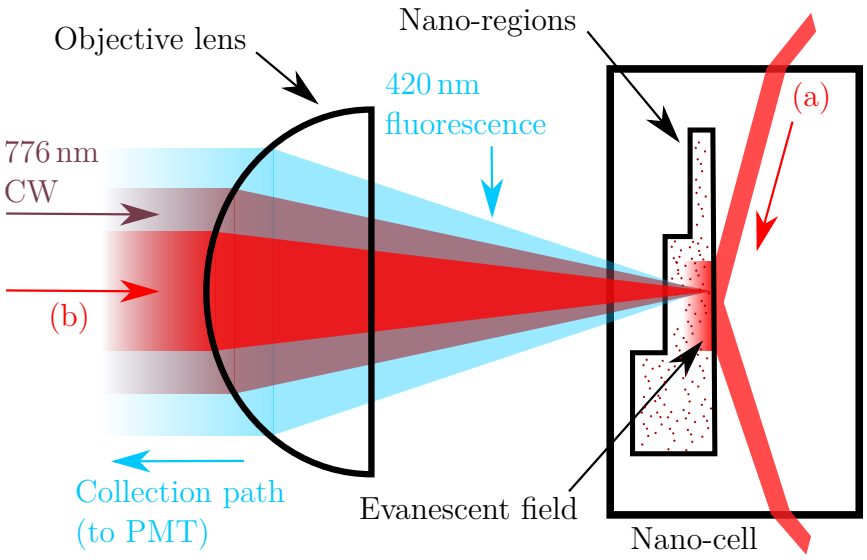

Figure 6.14: Experimental setup schematic (not to scale) for two-colour pulsed excitation in a nano-cell. A CW 776 nm laser beam resonant with the Rb $5P_{3/2} \rightarrow 5D_{5/2}$ transition was incident on the nano-regions via the objective lens. The 780 nm laser with 1.5 ns pulses at a repetition rate of 1 MHz was incident on the nano-regions in one of two geometries: (a) in a total internal reflection geometry in the same way as Fig. 6.6 (focussed to a spot size of order 100 µm at the nano-regions); (b) confocally via the same objective as the 776 nm laser. Atomic fluorescence at 420 nm was collected via the objective lens and onto a photon-counting photomultiplier tube (PMT). 420 nm bandpass filters were used to extinguish reflected laser light before the PMT.

6.5.2 Pulsed fluorescence dynamics

In this section we employ a scheme using 1.5 ns 780 nm laser pulses as in the previous section, but with the addition of a CW laser at 776 nm. Atoms are excited by the two lasers to the $5D_{5/2}$ state, from which they can decay via the $6P_{3/2}$ state and emit at 420 nm (see chapter 5, and Fig. 5.1 for details). The $5D_{5/2} \rightarrow 6P_{3/2}$ transition has a lifetime of 822 ns, whilst the $6P_{3/2} \rightarrow 5S_{1/2}$ transition has a lifetime of 500 ns [75]. As such, the whole two-colour scheme has a much longer natural lifetime than the 26 ns of the scheme in the previous section.

In Fig. 6.15, we show the excitation and decay dynamics for this new scheme through the 420 nm fluorescence activity for three different nano-cell thicknesses. We observe a trend of reducing 1/e decay timescale with reducing thickness, as would be expected for a lifetime limited by wall collisions.

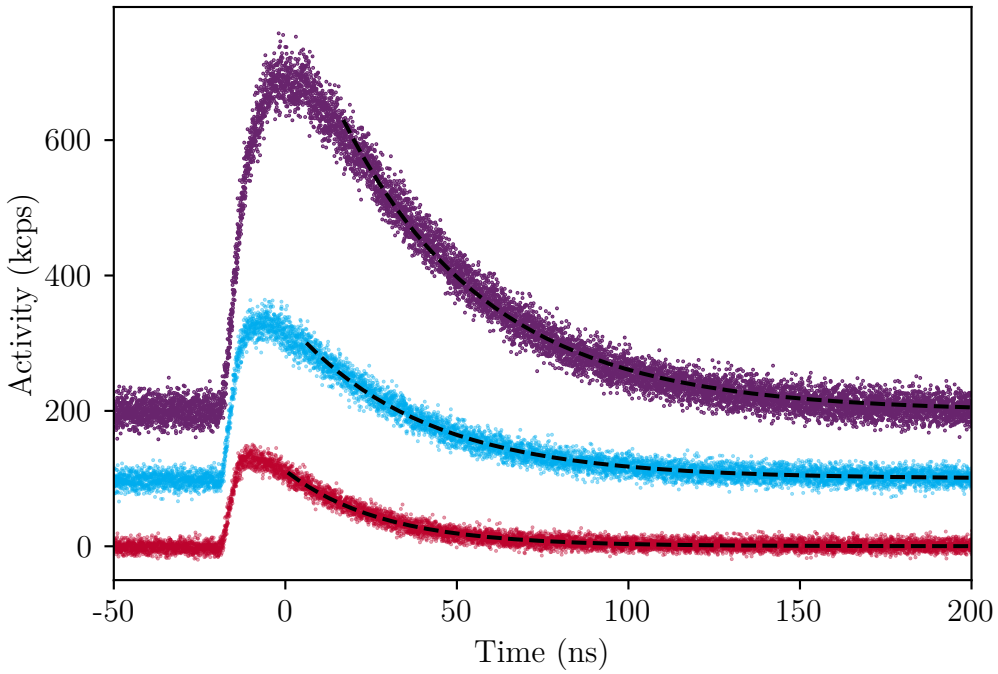

Figure 6.15: Fluorescence activity at 420 nm under pulsed excitation, from atoms confined to three different cell thicknesses: 2 µm (purple), 1 µm (blue), and 500 nm (red). Each plot is vertically offset by 100 kcps for clarity. Empirical exponential decay fits (black dashed) yielded 1/e decay timescales of 42.75(10) ns, 38.71(13) ns and 28.03(14) ns, respectively. The zero point of the time axis was chosen to be at the peak of the 2 µm activity curve, however all curves share a common experimental trigger (i.e. the time at which the pulse arrived at the cell was the same for each one). The atoms were excited by a 1.7 ns FWHM 780 nm pulse with peak power of 400 µW in a TIRF geometry (pathway (a) in Fig. 6.14), and a CW 400 µW 776 nm laser perpendicular to the cell walls. The cell temperature was 120 °C.

However, we observe that the lifetimes are still proportionally longer than those measured in the previous section for single-colour excitation. We can still observe fluorescence activity above the background level in the 1 µm cell at at least 100 ns, which is considerable given the atomic wall-to-wall time of flight of an average thermal atom for this confinement is on the order of a few nanoseconds.

The peak of the activity curve also varies with thickness. We observe an earlier and narrower peak before activity decays for the thinner cells. We postulate that this is due to the increased velocity selection imposed by the closer cell walls. For a thinner cell, we will have fewer atoms entering the excitation region from the sides, and those that do will have a narrower

velocity distribution in the transverse direction. Thus they will experience a narrower range of Rabi frequencies and thus the excitation timescale will be less smeared out. In a thinner cell wall collisions will be more significant at earlier times, and thus begin to reduce the fluorescence activity earlier than in a thicker cell. Thus we believe these factors explain the shorter turn-over time and thus narrower peak.

We note that the ratio of the total fluorescence counts within each curve for the three thickness regions is 1 : 0.38 : 0.16 for 2 µm, 1 µm and 500 nm respectively. That the ratio of fluorescence counts is not 1 : 0.5 : 0.25 following the ratio of cell thicknesses is believed to be due to quenching at the walls. If, for example, atoms fluoresced upon colliding with the walls, the ratio of the total fluorescence counts should be proportional to the cell thickness ratios as all atoms would fluoresce (just with different temporal dynamics). However, if atoms collide with the cell walls and decay non-radiatively, the reduction in count rate will not be linear with thickness, as disproportionately more atoms in thinner cells collide non-radiatively without having chance to fluoresce whilst in the vapour phase.

We reported in section 6.3 that a good fit to our fluorescence activity decay dynamics was achieved by a simple model - multiplying together the decay curves due to the natural lifetime of the state and the rate of atom loss due to cell wall collisions. The lifetimes of the states involved in the excitation scheme used in this section are now much longer. However, even combining the lifetimes of the decays involved ($5D_{5/2} \rightarrow 6P_{3/2}$ has a lifetime of 822 ns, $6P_{3/2} \rightarrow 5S_{1/2}$ has 500 ns), using the same simple methodology considerably underestimates the decay lifetime of the 420 nm fluorescence activity observed. This simple model yielded an exponential decay time of only 9.3 ns for a 2 µm thick cell, which is considerably different from the measured value of 42.75(10) ns. This suggests that the simple model is now no longer encapsulating the full dynamics of the system. Thus we will instead compare our results to a four-level Monte Carlo wavefunction simulation, similar to those described in section 6.2.

The results of our simulations compared to experimental data are shown in Fig. 6.16 for a 1 µm cell. The simulations also predict the rise time and turnover time of the curve with reasonable accuracy. However, the simulated results have a longer exponential decay timescale than the experimental results, meaning that the simulation predicts proportionally more atoms de-

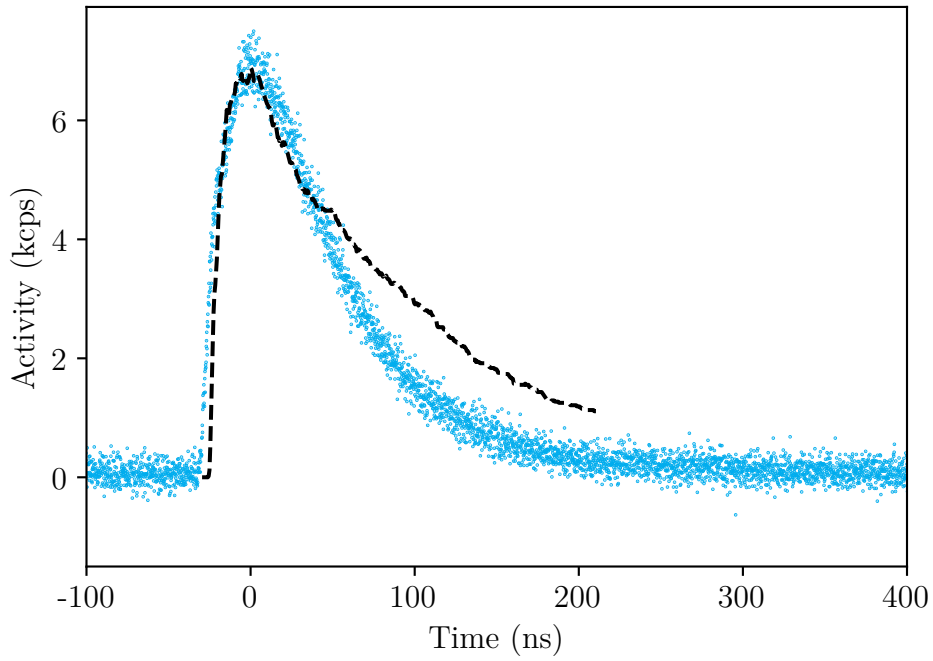

Figure 6.16: Results of a four-level quantum jump simulation (black dashed line) as compared to experimental data for a 1 µm cell. The simulation was initialised with 5×10^5 starting atoms, with input parameters matched to those of the experiment (see Fig. 6.15 where this experimental data was initially presented along with parameters).

caying at longer times than the experiment shows. There are some possible explanations for this discrepancy. Firstly, this four-level scheme involves a transition from $5D_{5/2}$ to $6P_{3/2}$, which is 5 µm in wavelength. This means that collective behaviour for this transition could become considerable at much lower densities than for other transitions we probe in this work (e.g. at 780 nm). The 5 µm wavelength is also within the range of the substrate phonon absorption spectrum, and it is possible that this alters the atom-wall interaction behaviour. Incomplete quenching of the $5D_{5/2}$ state for this reason when interacting with a sapphire substrate has been studied previously [162]. Other possible causes of the discrepancy lie with the simplicity of the simulation: the level structure of rubidium including all hyperfine levels is not accounted for, nor are the two rubidium isotopes or atom-atom collisions. However, this quantum jump simulation does much more closely predict the decay timescale observed in the experiment than the simple simulations involving only the state lifetimes and the decay in atom number due to wall collisions.

We repeated similar experiments to those which yielded the results shown in Fig. 6.15, but with varying peak pulse power and varying cell temperature. For the case of varying 780 nm peak pulse power, measurements were taken in the range 4–1000 µW. This was done in a 500 nm thickness cell region at 130 °C, with a CW 776 nm power of 380 µW. The fitted decay timescales varied negligibly for these datasets, suggesting there was no trend with varying 780 nm power over the range studied.

For the case of temperature variation, measurements were taken in the range 60–130 °C in a 2 µm thickness cell region. There was negligible variation and no discernible trend for the fitted decay timescales with temperature. Using conventional steady-state vapour-pressure equations, this range amounts to a variation of nearly three orders of magnitude in atomic number density, and whilst these equations may not hold exactly in tightly-confined regimes [1], a measured variation in fluorescence activity of two orders of magnitude suggests a considerable density variation was achieved. In contrast, we have already demonstrated in Fig. 6.10 that for the single-colour excitation case there is some variation in decay timescale with density (and thus temperature). This, however, was measured over a higher temperature range (125–185 °C), whereby the considerably lower mean atomic spacings are more likely to facilitate collective behaviour. It would be interesting in future works to test whether this potential collective behaviour is also observed in the case of two-colour excitation.

6.5.3 Comparison between thin and bulk cells

So far in this chapter, we have presented results solely from thin cells. To verify that the behaviour we observe is related to the tight confinement as we have postulated, we decided to perform a similar two-colour pulsed excitation experiment in a bulk 75 mm vapour cell (filled with rubidium at natural abundance). The experimental methodology was closely related to that presented in section 6.5.1, with some modifications. The nano-cell was replaced with the 75 mm cell, and the 780 nm and 776 nm laser beams were overlapped and co-propagated into the cell without a focusing lens (with a beam diameter of approximately 1 mm). As we would expect longer decay timescales than in the thin cell case, the 780 nm laser was pulsed at a repetition rate of 100 kHz rather than 1 MHz to ensure that the whole timescale

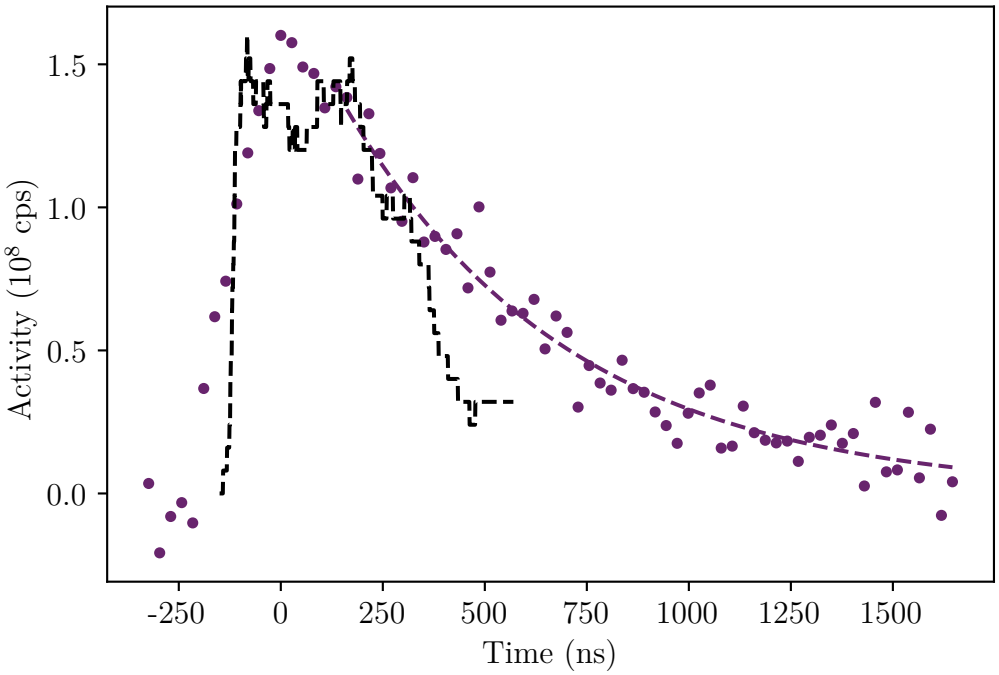

Figure 6.17: Experimental data and simulations for two-colour pulsed excitation in a 75 mm vapour cell. Experimental data is shown (purple dots) with an exponential decay fit (purple line). This fit yielded a 1/e decay time of 550(60) ns. The cell was at room temperature, and the two excitation lasers were co-propagated through the cell, with beam diameters of 1 mm. The 780 nm laser had 1.7 ns pulses with a peak power of 500 µW, and the 776 nm laser was CW with a power of 400 µW. Shown for comparison are the results of a four-level quantum jump simulation (black dashed).

of the fluorescence dynamics could be recorded before a subsequent pulse. Fluorescence was collected orthogonally to the laser beams through the side of the cell, and recorded via a PMT.

We endeavoured to understand the temporal fluorescence dynamics for vapour atoms in the bulk cell case from both a theoretical and experimental standpoint, and data for both are shown in Fig. 6.17. For our theoretical model, we again used the quantum jump approach (described in more detail in appendix B). For simulations in a bulk cell, wall collisions are rare and atoms spend much longer in the beam. Atoms which enter the $6P_{3/2}$ state can decay to the ground state via our pathway of interest, through emission of a 420 nm photon. We will denote the rate of decay for this pathway as A_1. However, they can also decay via alternative pathways which we do not measure photons from, with a higher rate. The total lifetime of the state

is 113 ns [75], but the effective lifetime of our transition of interest is much longer ($1/A_1 = 500$ ns).

In contrast to the simulations, our experimental fluorescence activity data shown in Fig. 6.17 shows a longer decay lifetime of 550(60) ns. This is consistent within error with the effective lifetime of our transition in question ($1/A_1 = 500$ ns). The observed discrepancy between theory and experiment could be due to a number of factors. We believe the main contributing factor to be the CW 776 nm laser re-exciting atoms that decayed from the $6P_{3/2}$ state via the $6S_{1/2}$ state into the $5P_{3/2}$ state. These atoms could then be re-excited to the $5D_{5/2}$ state and thus the rate of decay of population from the $6P_{3/2}$ state is governed most significantly by the decay back to the ground state (from which they cannot be re-excited after the duration of the 780 nm pulse). We have added such decays to our model by adding a pathway to return to $5P_{3/2}$ from $6P_{3/2}$, however this did not account for the decay lifetime of the $6S_{1/2}$ state, or further possible transitions. The rise time of the simulation is also much quicker than the experiment, which may be impacted by the spread of Rabi frequencies experienced by the atoms, as well as atoms more freely entering and leaving the beam in the bulk cell. Other factors not considered in our simple simulations include atom-atom interactions, hyperfine structure, and pumping processes, which may also impact the timescales observed.

Comparing the experimental results shown in Fig. 6.17(b) for a 75 mm vapour cell to the results we have presented in a 1 µm cell in Fig. 6.16, we observe a stark difference. The 1/e decay timescale for a 1 µm cell is 38.71(13) ns, as compared to 550(60) ns in the 75 mm cell. This shows the considerable impact of the imposition of micron-scale confinement in reducing the timescale observed. We also observe differences in rise time and turn-over time of the curve, which we postulate are due to a combination of the different Rabi frequencies used between the two experiments and the velocity selectivity in the thin cell which has been discussed above. Whilst our simulations do not quantitatively fit the experimentally observed data well, they do qualitatively reproduce the stark difference in timescales and dynamics observed between bulk and thin cells.

6.5.4 Pulsed fluorescence in a micro- and nano-channel

In the section 6.5, we gained an understanding of the atomic dynamics under two-colour pulsed excitation in a conventional thin cell (with confinement in one dimension). As such, we can now move to probing atoms confined to the more complex structures facilitated by our cell manufacturing methodology [1]. We have already found that confinement in more than one dimension can lead to variation in atomic density (see section 5.3.2 and references [1,82]), and we postulate that this extra confinement may alter the dynamics of the atom-light interaction process further. For example, in a 'channel' structure, atoms which have a higher speed in not one but two different dimensions now collide more quickly with the cell walls and thus have less time to interact and emit. As well as this, the supply of new vapour atoms into the interaction region is now only from the cell walls or along the channel in one dimension, the latter limiting the possible velocity classes.

To test the pulsed excitation response in the channel regime, we have used a similar two-colour pulsed excitation scheme to that described in section 6.5. For this experiment we employed a NA = 0.7 microscope objective to focus the excitation laser light to a spot size of order 1 µm such that we could probe atoms confined to a single micron-scale channel. We collected atomic fluorescence light at 420 nm using the same objective, and filtered this from scattered laser light and other background light using a dichroic mirror and 420 nm bandpass filters. This setup bears similarities to that which was shown to be effective for spectroscopy of atoms in channel structures in chapter 5. As in section 6.5.1, atomic fluorescence was collected onto a photon counter and recorded over many pulse events.

Our first experiment studied the difference in dynamics between a 'slab' (confinement only in one dimension) and a 'channel' (confinement in two dimensions) region, as shown in Fig. 6.18. Here we measured the temporal fluorescence activity dynamics as was done in section 6.5.2, however with a different beam geometry. In this case both the pulsed 780 nm laser and the CW 776 nm laser were co-propagating and incident on the thin regions via the front face of the cell, with atomic fluorescence collected back along the same path (as shown in Fig. 6.14 with the 780 nm laser along pathway (b)). The 'slab' dataset (red) was for the same regime as the 1 µm data in Fig. 6.15, but with this differing beam geometry and also different experimental parameters

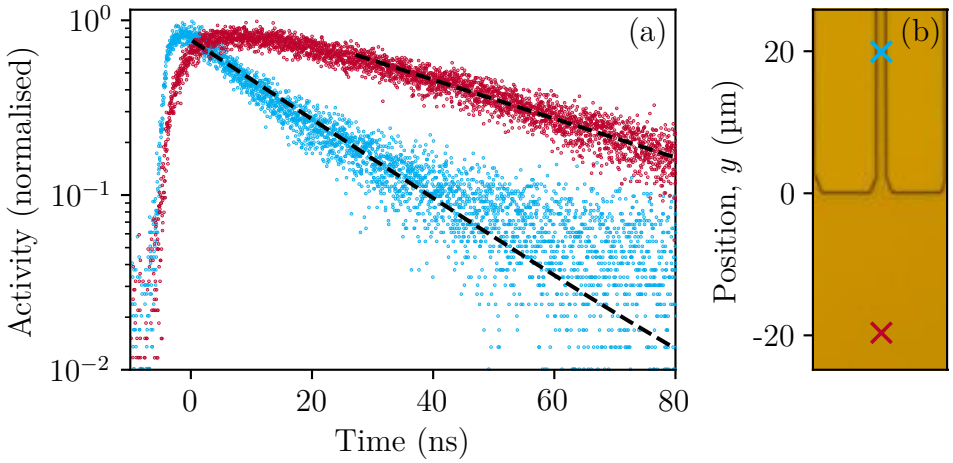

Figure 6.18: **(a)** Comparison between the atomic 420 nm fluorescence activity dynamics under pulsed excitation of a 'slab' region with 1 µm confinement in one dimension (red) and a 'channel' with 1 µm confinement in two dimensions (blue). Both datasets have been normalised to have a peak activity of 1 and had the background count rate subtracted for clarity of comparison. The peak activity before normalisation was 5× higher in the 'slab' than the 'channel' case. Exponential decay fits (black dashed lines) yielded 1/e decay timescales of 39.13(14) ns and 19.05(8) ns respectively. Note that the fits were chosen to start at different times due to the difference in 'turn-over' time of the two curves. For both datasets the cell temperature was 130 °C, and the atoms were excited to the $5D_{3/2}$ state with pulsed 1.7 ns FWHM 780 nm light with a peak power of 1.2 mW (at a repetition rate of 1 MHz), and 380 µW CW 776 nm light (both focused to a spot size of order 1 µm via an $f = 2$ mm lens, see Fig. 6.14 pathway (b)). **(b)** Bright-field image showing the 'channel' (top) and 'slab' region (bottom), showing the y position at which each dataset was taken.

(laser powers and cell temperature). The timescales measured in both cases are in reasonable agreement considering these changes. To take the channel dataset (blue), the cell was translated such that the laser beam was instead incident on a 1 µm × 1 µm channel. We observed a considerable change in dynamics between the slab and channel cases. Firstly, the rise time was shorter for the channel case, with the peak in activity occurring much earlier. The peak was narrower, with a much quicker 'turn-over' time before activity began to decay. As well as this, the decay timescale was considerably shorter (39.13(14) ns for the slab compared to 19.05(8) ns for the channel case). We postulate that both of these differences are due to the increased confinement and thus shortened average time before an excited atom collides with a cell

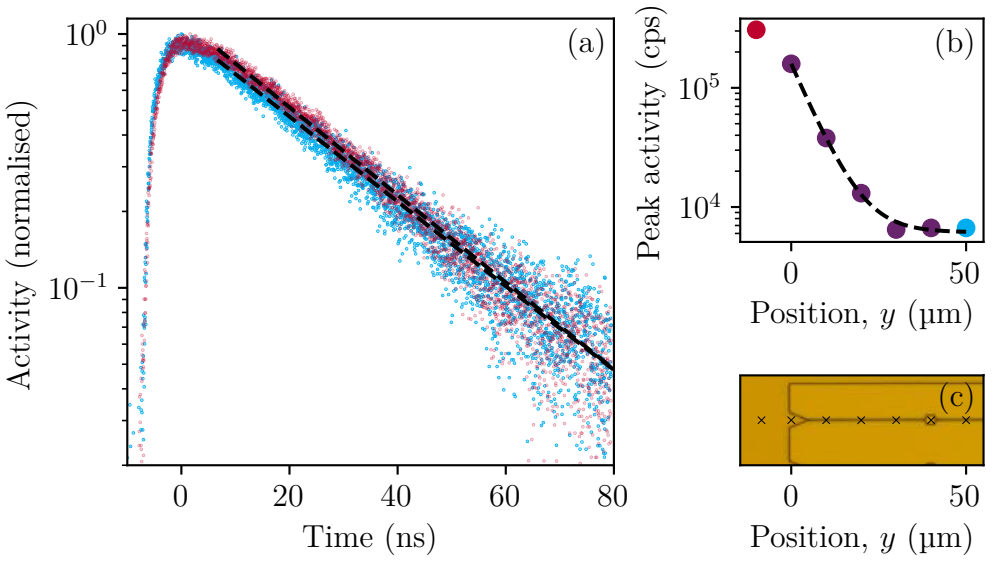

Figure 6.19: Comparison between the atomic 420 nm fluorescence activity dynamics under pulsed excitation from a 'slab' region with 500 nm confinement in one dimension (red) and positions along a 'channel' with 500 nm × 800 nm confinement (blue). **(a)** Activity dynamics for the 'slab' region and for a point 50 µm along the channel. Both datasets have been normalised to have a peak activity of 1 and had the background count rate subtracted for clarity of comparison. Exponential decay fits (black dashed lines) yielded 1/e decay timescales of 25.06(6) ns and 22.0(12) ns respectively. **(b)** The change in peak activity with distance along the channel. Error bars are smaller than the datapoints. For the extreme cases shown in (a), and denoted by their respective colours here, the peak activity was 46× higher in the 'slab' than the 'channel'. The fitted exponential decay (black dashed line) yielded a 1/e lengthscale of 6.37(13) µm. For all datasets the cell temperature was 130 °C, and the atoms were excited to the $5D_{3/2}$ state with pulsed 1.7 ns FWHM 780 nm light with a peak power of 500 µW (repetition rate of 1 MHz), and 400 µW CW 776 nm light (both focused to a spot size of order 1 µm via an $f = 2$ mm lens, see Fig. 6.14 pathway (b)). **(c)** Bright-field image showing the channel structure probed, with crosses indicating the points at which datasets were taken. Note that a 2 µm × 2 µm × 500 nm 'pocket' is located at $y = 40$ µm.

wall in the channel. We also tested a second point within the same channel (data not shown), which gave the same response dynamics as the first channel dataset, verifying that the results are an effect of the channel confinement and not specific to one singular location or dataset.

We studied a second channel with a smaller cross-section (0.5 µm × 0.8 µm) in more detail. Datasets were recorded (in the same manner as above) at six

points along the channel (as well as one outside the channel in the 500 nm thickness 'slab' region) in order to test for any change in dynamics. The results are summarised in Fig. 6.19. We firstly observe in (a) that the stark change in dynamics which was observed in Fig. 6.18 when moving from the 1 µm 'slab' region to the 1 µm channel is not present in this more confined geometry. There is still a reduction in 1/e timescale when moving to the more confined channel geometry as observed previously (25.06(6) ns in the slab as compared to 22.0(12) ns in the channel), but this difference is much less significant than in the data shown in Fig. 6.18. We postulate that the tighter confinement in the 500 nm region already leads to a more considerable suppression of the fluorescence decay timescale, and thus any additional reduction due to the extra confinement dimension in the nano-channel has proportionally less impact. We note that the second confinement dimension in the channel is larger than the initial confinement in the 'slab' region (800 nm vs 500 nm), whilst in the previous experiment they were equal. This is likely also the reason why the difference in peak activity between the two datasets in Fig. 6.19 is much larger than in Fig. 6.18. It would be interesting in future work to test whether a channel of (or narrower than) 500 nm width would produce a discernible difference from the 'slab' 500 nm region (this width of channel was the smallest achieved in our current generation of cells).

We also studied the change in activity with distance along the channel, and the results are shown in Fig. 6.19(b). We observed an exponentially-decaying activity, reducing to a background level. We observed little impact of the larger 2 µm × 2 µm × 500 nm 'pocket' present in the channel at $y = 40$ µm, with only a small increase in activity as compared to the previous datapoint. This is interesting as it may be expected that the larger area would contain more atoms which could be probed by the approximately 1 µm excitation laser spot, and also atoms in this region would take longer on average to hit the cell walls than in the rest of the channel. However, clearly diffusion dynamics still mean the atom number is low. From our activity results, we concluded that the number of atoms contributing to fluorescence, and thus the atomic density, was reducing along the channel. This matches our conclusion in section 5.3.2. In that section the 1/e decay timescale for this effect was measured to be 4.0(11) µm, whereas in this pulsed setup we found 6.37(13) µm. Whilst these do not agree within error, the values are relatively close, and there are some key differences between the two experiments. Firstly, the experiment

in section 5.3.2 summed the count rate under the whole width of two spectroscopic features, not just on resonance with one transition as in this case. They thus accounted for contributions of a wider range of atomic velocity classes and also for more transitions: those from both ^{87}Rb $5S_{1/2}$ $F = 1$ and ^{85}Rb $5S_{1/2}$ $F = 2$ to the relevant $5P_{3/2}$ hyperfine states. Other differences lay in the channel cross-sections (1 µm × 1 µm vs 0.5 µm × 0.8 µm in this case), laser powers, and in the use of pulsed or CW excitation. As well as these differences, the history of the cell at the time of each experiment was different, so it is possible that the distribution of atoms adsorbed onto the cell walls had changed, which we understand to impact local vapour density (see chapter 3). Whilst without considerable further study of the parameter space it is hard to evaluate the relative contributions of any of these differences, we can at least conclude that both experiments verify and corroborate the conclusion that atomic density reduces exponentially along a thin channel with a lengthscale of order microns.

6.6 Conclusion

In this study we have performed novel (to the author's knowledge) studies of the response of a thin atomic layer to nanosecond resonant laser pulses. We have investigated different excitation schemes and how their relative timescales and lifetimes impact the state of the atomic ensemble, which we infer from measured fluorescence activity. We find that for a single-colour pulsed excitation scheme resonant with the rubidium D2 line, the ensemble behaves as if every atom partakes in the excitation, with the turn-on time being related to the excitation Rabi frequency and the decay time simply a product of the state lifetime and the lifetime of atoms within the cell before wall-collision. However, perhaps more surprisingly, we have found that for a two-colour excitation scheme (with multiple levels and much longer lifetimes) the dynamics cannot be explained by this simple model. We propose that the longer timescales impart a velocity selectivity to the process, an effect which could be harnessed and would benefit from further study.

We have presented quantum jump type simulations which corroborate our velocity selectivity hypothesis. We have also demonstrated the extra insight that can be gained through pairing experimental measurements with such simulations, extracting information about the likely position and velo-

city distributions of the atoms in the excited state over time. Whilst our simulations do not perfectly agree quantitatively with all experimental datasets, their reasonable agreement and good qualitative agreement demonstrate that this is still a promising route of study. Overall, this investigation shows that there is still much to learn and understand about even seemingly simple test cases of atom-light interaction. We propose that our nano-cells provide a good test-bed to study such physics, as we have illustrated in this chapter and throughout this thesis.

Chapter 7

Conclusion and outlook

7.1 Conclusion

In this thesis, we have presented a number of studies involving our nanostructured alkali metal vapour cell platform. Each chapter presents a novel investigative route, each of which contributes to the development of the platform and understanding of the behaviour of thermal vapours and the fundamental physics of atom-light interaction in confined geometries. The aim for our platform is to facilitate both novel fundamental physics experiments and technological applications, and each of the investigations presented in this thesis provides critical insights and initial steps.

In chapter 3, we discussed advances to the fabrication and design of our nano-cell, which represent progress towards the cells forming the basis for atom-based technologies. Such incremental improvements and diversification of the platform are necessary for maturation towards a diverse range of applications. We have also tested the limits of our manufacturing process, and progressed towards incorporating ever smaller integrated features in our cells. We have demonstrated the new capability of integrating metal nanoparticles into our cells, as well as adding further confinement geometries in the form of arrays of pockets on the order of 100 nm in extent.

In chapter 4, we demonstrated the well-known LIAD effect on a novel lengthscale facilitated by our thin cell design. We demonstrated that vapour density within our cells can be controlled in a localised manner using non-resonant 450 nm laser light with a spot size of order 1 µm, and that with our fused silica substrate we can achieve density increases of up to 5× the back-

ground level. This adds critical insight to the body of knowledge already built up of the LIAD effect and its limitations and regimes of applicability. We also observed the competing effect we term LICo, and performed measurements of this effect at novel lengthscales. We have characterised the regimes in which it is applicable, and compared these to those relevant for LIAD, which will prove useful for future studies of both effects. As the LICo effect is little mentioned in scientific literature, our study provides novel insight into its behaviour in a new regime.

In chapters 5 and 6 (and briefly in 4) we used a two-colour excitation scheme to facilitate the study of atoms confined to nano-scale structures through fluorescence-based measurements. In chapter 5 we characterised the line-widths achievable for atoms in our confinement regimes with this scheme. The methodology was shown to be low-noise and effective in studying atoms in complex nano-scale confinement geometries. Our work paves the way toward further studies at reduced lengthscales, including of atoms confined to smaller and more complex structures. We demonstrated in chapter 3 the versatility of our cell manufacturing process and some further possibilities for patterning of our thermal vapour medium, and it would be interesting to further this by probing thermal atoms confined to patterned regular arrays and searching for enhanced collective responses.

In both chapters 5 and 6 we observed an exponential decay in fluorescence activity along a micron-scale or sub-micron etched channel with a hot (of order 100 °C) vapour. The same effect of confinement on vapour density in a nano-cell was first suggested in [82] in a study done at room temperature. We have both corroborated the observation of such an effect, and added to the knowledge surrounding it: we now understand that it occurs at higher temperatures and not just room temperature, and for cells with a much longer history of heating, cooling and flooding. Our cell design facilitated the necessary spatial resolution to perform measurements of the decay length in two different channels with differing micrometric and sub-micron cross-sections. This diffusive effect is still new to the thermal vapours community, and it could have applications in controlling the distribution of vapour number density without heating.

Finally, we provided insight into the fundamental physics of the atom-light interaction process in our thin cells as compared to conventional vapour cells, through the novel experiments and simulations involving the time-dependence

of the atomic response presented in chapter 6. Such work presents new knowledge in this little-studied area of thermal vapour physics, and has the potential to be built upon in future by more advanced modelling and more complex experiments (e.g. involving multiple pulsed lasers). Building upon this insight is critical for the development of thermal-vapour based devices where interactions and processes can be achieved on short timescales before motional effects such as dephasing become problematic.

Overall, throughout this work we have pushed the boundaries of our nano-cell platform, and demonstrated its versatility and applicability to a varied selection of technological problems and fundamental physics questions. We have demonstrated novel experimental results at lengthscales previously difficult to access for the thermal vapours community. In the following section, we will provide suggestions for further experiments and directions of study to build upon the basis of knowledge presented in this thesis. These will both push forward knowledge in the field of fundamental atom-light interaction and further our platform as a potential basis for technological applications.

7.2 Outlook

7.2.1 Nano-cell fabrication and characterisation

In chapter 3, we demonstrated an array of novel design capabilities and advancements to our nano-cell platform. Further development should focus on further pushing the limits of our manufacturing methods, towards smaller and more complex integrated structures. For example, the integration of waveguides into thermal vapour environments, and interfacing these with atoms (often through evanescent coupling), has previously been demonstrated [61,178–181]. Integration of such waveguide structures into our robust nano-cell platform could allow for further investigation of atom-light interaction physics with confinement of both the vapour atoms and the interacting light field. There are other possible integrated structures of interest which could be added to our cells, which include opto-mechanical features [182], diffractive elements [59], or complex photonic structures. Furthermore, solid immersion lenses could be integrated into the front face of our cell, allowing for even higher NA interrogation and imaging than is currently afforded by our current thin front panel and objective combination. This would allow

for smaller structures to be probed and improve mechanical stability during experiments by coupling the motion of the lens and the cell itself.

One specific proposed technological application involves integration of materials which would reside inside the finished nano-cell, close to the vapour layer. Thermal vapours have already been demonstrated as convenient magnetometers [8, 16, 72] and thus this capability could enable magnetic field measurements extremely close to material surfaces. The proximity and short extent of the vapour layer would mean that little averaging over the field at different distances from the surface would occur. We have already demonstrated metal particle and AlOx deposition which survives cell manufacture and bonding, so it is reasonable to expect that other materials may be possible. Other related possibilities include the deposition of anti-relaxation coatings on internal surfaces, which have been proven to be useful in other works [58, 126].

Miniaturisation has been a great driver of recent thermal vapour experiment innovations (as discussed in chapter 1), and is a possible area for improvement for our cells. We have already shown in chapter 3 that it is possible to reduce our overall cell thickness from 10.5 mm to 4.5 mm, and that there is a viable compact heating solution for our cell in the form of ITO coating. Cell dimensions, however, could be reduced further, perhaps even enough to allow high-NA access from both sides of the cell. This, however, would reduce mechanical robustness, and thus the question of improvements becomes application-specific. The rubidium reservoir would then become the size-limiting feature. This is currently approximately 50 mm in length and 8 mm in diameter, but could potentially be reduced, or an altogether different methodology used to insert rubidium into the cells. Getter pills are a potential candidate, and have been used in millimetre-sized MEMS cells as a source of alkali-metal vapour [56, 101].

7.2.2 LIAD and LICo in thin cells

In chapter 4, we demonstrated the effects of LIAD and LICo at novel length-scales, and used them for the generation of high densities of rubidium atoms in both the vapour phase and condensed onto the walls of our thin cells. In terms of LICo, we demonstrated potential to harness the effect for practical purposes. One possibility is creating transient high-density regions of wall-

adsorbed atoms, allowing for the redistribution of local reservoirs of rubidium within the cell. Since diffusion plays a key role in vapour distribution in thin cells, we believe such local reservoirs are of critical importance in maintaining vapour density locally (as described in section 3.4). Thus the ability to create and manipulate local reservoirs would be a useful tool to allow for more precise control of vapour density in future experiments. We have recorded results suggesting it may be possible to influence local vapour density by leveraging the LICo effect (see Fig. 4.6), but much more work needs to be done to verify and optimise this process. As discussed in section 3.4, diffusion of wall-adsorbed atoms appears to happen more slowly in thinner regions and in regions of greater confinement (e.g. channels, with confinement in two dimensions), and thus inducing a condensed region of rubidium atoms via LICo in one of these regions and studying the subsequent fluorescence may give higher vapour densities which do not diffuse as quickly as in the less confined regions. It would also be useful to study the LICo effect in, for example, a wedge-shaped cell. As we only observed the LICo effect in two of our three discrete thickness regions, this would allow us to measure the thickness at which this effect becomes significant (or indeed verify whether another parameter such as the etched surface roughness caused the differences between regions).

With view to technological applications, it would be interesting to test the wavelength dependence of the LIAD effect in our cells, so as to optimise the procedure of vapour generation. Towards the goal of fast and reproducible control of atomic density, it would also be useful to use an excitation laser with short pulses rather than simply switching on a CW laser. This is because we believe the turn-on time of our CW laser limited the rise time of our atomic density, and so faster pulsing could enable study of the underlying fundamental timescales of the turn on and off of the LIAD effect which could not be accessed here. It would be useful to then quantify, over many pulse events, the stability and reproducibility of the vapour density increase, as a lack of reproducibility is a common problem in LIAD experiments (though often not discussed in the literature). Along similar lines, it would be useful to investigate the reproducibility of the LIAD effect more quantitatively in relation to the history of our cells, as it has been suggested in previous works that 'curing' of the surface when exposed to the vapour of choice, as well as previous illumination, may factor in the subsequent LIAD response [138]. We

already know that the density of wall-adsorbed atoms varies with cell history through flooding and depletion (as was shown in section 3.5), and it is likely that time after flooding is a part of this history-dependent LIAD response.

7.2.3 Spectroscopy of atoms confined to thin cells

In chapter 5 we demonstrated a two-colour scheme for fluorescence-based spectroscopy in a variety of micro- and nano-scale geometries. For this work, rubidium was a convenient atom of choice given the availability of lasers and optics at the correct wavelengths. However, the two naturally-abundant rubidium isotopes make for complicated spectroscopy, especially if one wants to isolate a specific hyperfine transition (for example by addition of a magnetic field). As such, it would be interesting to revisit nano-cell spectroscopy in another commonly studied alkali metal such as caesium, with a single isotope and thus less complexity. Nano-cells have already begun to be produced containing other alkali metals such as caesium using our methodology and so this is a viable avenue of further work.

A variation of the scheme used in chapter 5 employs only a single laser at 778 nm to excite atoms via a two-photon transition to the $5D_{5/2}$ state. Possible further work could study this scheme in a nano-cell, which would simplify the experimental setup and complexity further. With two counter-propagating beams this two-photon setup could allow Doppler-free spectra, and studies have already suggested that such a scheme has potential applications in atomic clocks [183]. Other possible excitation schemes worthy of investigation include four wave mixing (see, for example, reference [184]). Four wave mixing schemes have been suggested as candidates for heralded single photons (through excitation to e.g. the $5D_{3/2}$ state in rubidium and then observing photons on the subsequent decays to $5P_{1/2}$ and then $5S_{1/2}$).

7.2.4 Pulsed excitation of atoms in thin cells

In chapter 6 we demonstrated novel experiments probing the temporal excited state dynamics of an atomic ensemble confined to a thin cell. There are a number of potential future experiments which could add to the knowledge gained in this study. Firstly, it would be interesting to continue to try to observe coherent dynamics in a nano-cell setting. There has already been evidence of Rabi oscillations in a nano-cell [37, 108], however such oscillations

were not observed in this work. However, coherent dynamics in the form of quantum beats were observed, suggesting that coherence can be maintained in our thermal vapour system. Our simulations have shed light on the regimes in which it may be possible to observe Rabi oscillations, and suggest that future work should focus on achieving a more uniform excitation region. This could be done, for example, by using optics to generate a laser spot with more spatially uniform intensity, or by using a large excitation laser spot but collecting fluorescence from a much smaller area.

Another experiment of interest would be to further the multi-level excitation investigation by pulsing both lasers (rather than having one pulsed and one CW). This may help to uncover the link between the level structure and the different timescales in the excitation and fluorescence dynamics. A related experiment would be to offset the two pulses in time. The first pulse, resonant with the D2 line, would prepare an ensemble of atoms in the $5P_{3/2}$ state. This ensemble would decay over time as the faster atoms hit the cell walls. Thus after some time, there will be proportionally more excited 'slow' atoms left in the vapour phase and in the region of interest. To then excite these atoms further to the $5D_{5/2}$ state with another pulse and watch them decay would be interesting, as one might expect the subsequent decay of this prepared ensemble of 'slow' excited atoms to be less impacted by shortening due to cell wall collisions.

We also briefly explored photon statistics measurements in a nano-cell using a pulsed excitation scheme. It has already been shown [185] that the second order correlation function can vary for excitation to higher states via one- or two-photon transitions, and so it may be interesting to move to a more complex excitation scheme, such as that described in chapter 5 and which has been begun to be investigated in section 6.5, and perform further photon statistics measurements. This scheme would have the further benefit that spectral filtering could be used to distinguish fluorescence photons at 420 nm from input infrared laser photons, and thus should produce cleaner signals.

7.2.5 Summary

In summary, we have outlined a diverse range of future directions of study involving thin cells and towards maturing our nano-cell platform. The diversity

of both the work presented in this thesis and the possible future experiments demonstrates the breadth of opportunity for development within our field. The opportunities described above are afforded by entering the new confinement regime for thermal vapour experiments facilitated by the development of nano-cells and furthered by our nano-structured cells.

Appendix A

Experimental setup and laser stabilisation

Throughout this thesis, experimental setups generally rely on one or two lasers to excite rubidium atoms from the ground $5S_{1/2}$ level to higher energy states. The most conventional is a single laser at 780 nm to excite from the ground state to the $5P_{3/2}$ state (commonly referred to as the D2 transition). For such experiments where resonant light was required, the 780 nm laser was frequency stabilised on resonance using ground state polarisation spectroscopy [186, 187]. Some experiments also employed a second laser at 776 nm, to excite atoms from the $5P_{3/2}$ state to the $5D_{5/2}$ state. This second laser was frequency stabilised on resonance using excited state polarisation spectroscopy. In this section we will detail these two methods, along with how we produced resonant pulsed laser light with possible repetition rates up to 10 MHz and Gaussian pulses with FWHM of less than 2 ns.

A.1 Ground state polarisation spectroscopy

The technique of ground state polarisation spectroscopy is a sub-Doppler pump-probe frequency stabilisation method, allowing for active stabilisation to a single hyperfine transition frequency to within a few MHz. In this work, we generally chose the strongest transition, ^{85}Rb $5S_{1/2}$ $F = 3 \rightarrow 5P_{3/2}$ $F' = 4$, for maximum signal and stability. However this method works generally for other choices of hyperfine transition.

Our stabilisation optical setup is shown in Fig. A.1 used a conventional

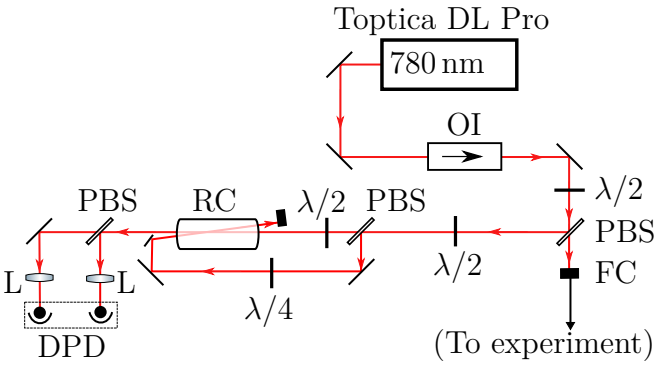

Figure A.1: Schematic diagram (not to scale) showing the optical setup for ground state polarisation spectroscopy. The laser used was a Toptica DL Pro at 780 nm, and the beam pathway is shown in red. Other components were: OI - optical isolator; PBS - polarising beamsplitter; FC - fibre coupler (sending laser light to the main experiment); RC - 75 mm rubidium cell (with magnetic shielding); L - $f = 50$ mm lens; DPD - differencing photodiode.

75 mm rubidium reference cell (with rubidium isotopes at natural abundance), which for this purpose did not require heating. The cell was, however, magnetically-shielded to reduce the impact of external magnetic fields on stability. We used a Toptica DL Pro laser with a CW output at 780 nm, which had a frequency scan range larger than the splitting of the four rubidium ground states (two hyperfine ground states for each natural isotope). We firstly split this laser beam into a weak linearly-polarised probe beam, and a stronger circularly-polarised pump beam. The pump beam was counter-propagated through the 75 mm cell at a small angle and overlapped with the probe.

The basic premise of the polarisation spectroscopy technique is to induce a birefringence in the atomic medium, and interrogate this using a weak probe beam. The circularly polarised pump beam drives σ^+ transitions, pumping population into the $m_F = F$ ground state. The linearly polarised probe beam can be considered a sum of two components, equal in amplitude but with opposite circular polarisation. The two components drive different transitions (σ^+ or σ^-), and due to the presence of the pump these will have differing absorption. This differing absorption results in a rotation of the probe beam polarisation, which can be measured by splitting this beam onto two photodiodes via a polarising beamsplitter cube (PBS). Taking the difference of these two signals gives the sharp error-function type signal at the frequency

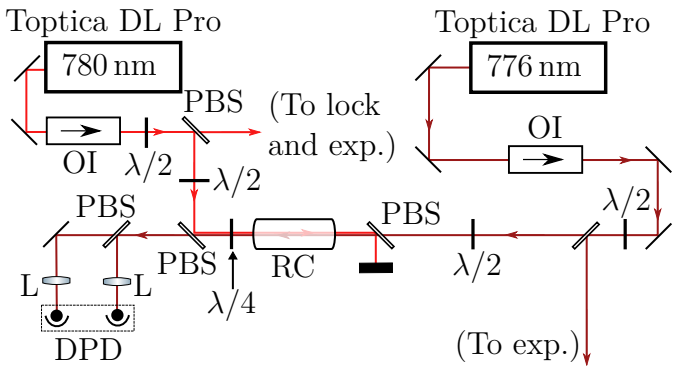

Figure A.2: Schematic diagram (not to scale) showing the optical setup for excited state polarisation spectroscopy. The two lasers used were both Toptica DL Pros, at 780 nm and 776 nm. Their beam pathways are shown in different shades of red. Other components were: OI - optical isolator; PBS - polarising beamsplitter; RC - 75 mm rubidium cell (with magnetic shielding); L - $f = 50$ mm lens; DPD - differencing photodiode. Note that some of the 780 nm laser is picked off before the cell to be used in its own stabilisation setup (denoted as 'lock', shown in Fig. A.1) and to go to the main nano-cell experiment.

of the transition in question, which was used for frequency stabilisation. This signal has a strong gradient around the resonant frequency, making it a good candidate for active stabilisation [186].

A.2 Excited state polarisation spectroscopy

The excited state polarisation spectroscopy technique follows a similar principle to that of ground state polarisation spectroscopy outlined in the previous section. However, in this case the pump and probe beams are at different frequencies. We used this technique to stabilise our 776 nm laser to the ^{85}Rb $5P_{3/2}$ $F' = 4 \rightarrow 5D_{5/2}$ $F'' = 3, 4, 5$ state (the hyperfine splitting of the $5D_{5/2}$ state is much smaller than that of the $5P_{3/2}$ state and thus individual F'' hyperfine states were not resolved).

The setup is shown in Fig. A.2, and was based around another 75 mm natural abundance rubidium reference cell. This cell was again magnetically-shielded, and was heated to 60 °C to increase vapour density and thus signal strength. We took our 780 nm beam (frequency stabilised as described in the previous section) and imparted a circular polarisation. In this setup this 780 nm beam was our pump, and transferred population into the $m_{F'} = F'$

state. We also had a probe beam from a second Toptica DL Pro at 776 nm, which was counter-propagated through the cell relative to the pump. Again an anisotropy is created in the medium, and thus the probe experiences differing absorption of left- and right-circularly polarised components. This difference was measured, as above, by taking the difference of two photodiode signals after splitting the two polarisation components using a PBS. The resulting signal again has a steep slope about the frequency of interest, and is a good candidate for frequency stabilisation [164]. We note that as this method used a stabilised laser as the first step, any fluctuations in the stability of that first step laser will carry through and potentially disrupt this second step stabilisation.

A.3 Producing nanosecond laser pulses

To produce the pulses of resonant laser light used in chapter 6, we began with a Toptica DL Pro CW laser, which was frequency stabilised as described in section A.1. This CW light was then coupled into an Aerodiode semiconductor optical modulator (SOM), which was triggered by an external function generator. This setup produced output light pulses down to approximately 1.5 ns in FWHM, which were Gaussian in shape for this short pulse duration (longer square pulses were also possible).

To measure the width and shape of the pulses, we used one of three methods. Two of these are shown in Fig. A.3. Firstly, we coupled the pulsed light into a fibre connected to a photon counting module (Excelitas SPCM-ARQH), making sure to lower the intensity sufficiently using neutral density (ND) filters so as to be far from saturating the counter. By correlating the counts incident on the photon counter with the pulse triggers and building up a histogram over many pulse events, a pulse profile was recovered which could be used to characterise the pulse width. The second method was to use a fast photodiode (EOT ET-2030A, with a rise and fall time of < 500 ps) to measure the pulse shape. The photon counting method gave a pulse with FWHM 1.5843(14) ns, whilst the photodiode gave a pulse width 2.581(17) ns. For the photodiode, the 500 ps timescale is sufficiently close to the pulse width that it had an impact on the measured width, whilst electronic ringing was also evident after the pulse.

The third method to measure the pulse width and shape was shown in

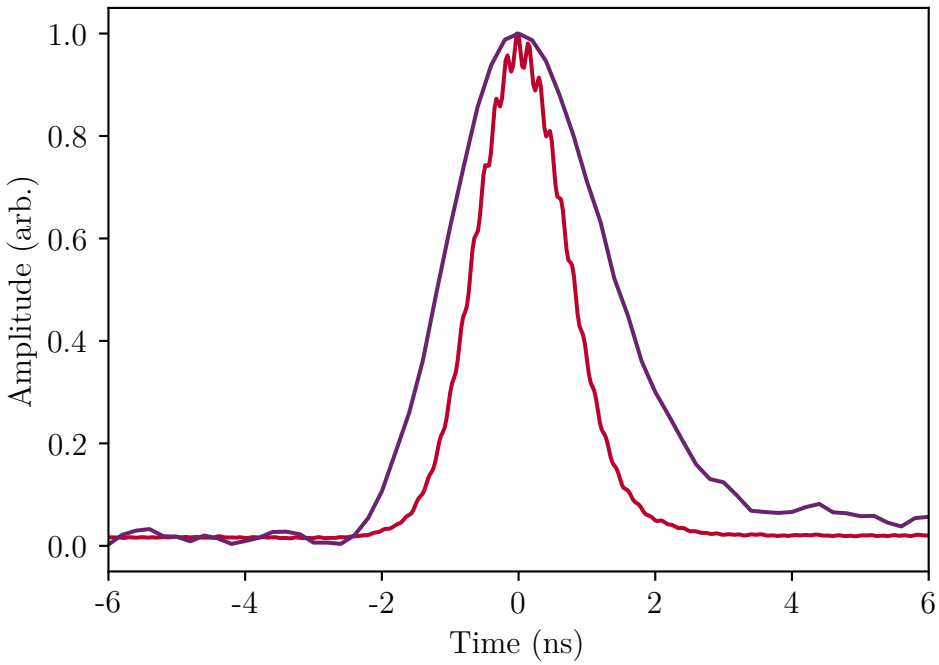

Figure A.3: Pulse width measured on the nanosecond timescale via two methods. An EOT ET-2030A photodiode (with a rise time of $< 500\,\text{ps}$) gave a pulse width of $2.581(17)\,\text{ns}$ (purple line). Coupling a small amount of the pulsed laser light into a fibre and onto an Excelitas SPCM-ARQH photon counter yielded a width of $1.5843(14)\,\text{ns}$ (red line). We conclude that the latter method yields the correct measurement of the width, whilst the former measurement is convolved with the rise and fall time of the photodiode.

Fig. 6.9. This method was very similar to that of coupling some pulsed laser light into a fibre and measuring the pulse over many repetitions using a photon counter. Here instead we had the setup exactly the same as for experiments described in chapter 6, and simply held the nano-cell at room temperature. In this regime, the vapour-phase atom number is so low in the micron-scale regions that the majority of the light detected by the photon counter was scattered laser light (e.g. from cell surfaces and defects) rather than atomic fluorescence. This method was convenient as it did not require a change of setup, just time to allow the cell to cool after an experimental run.

A.4 LIAD optical setup

For the measurements of LIAD in chapter 4, a different optical setup was used. This setup is shown in Fig. A.4. The 780 nm laser was stabilised

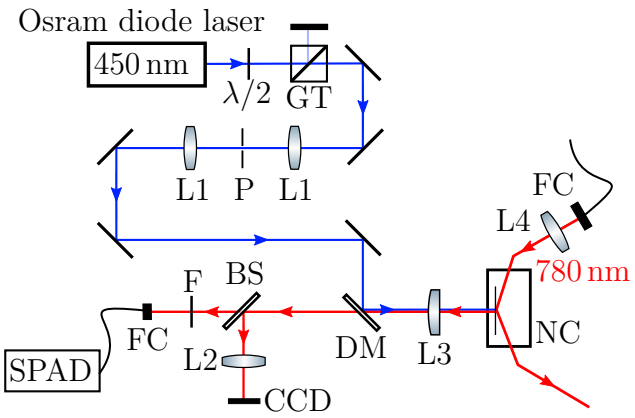

Figure A.4: Schematic diagram (not to scale) showing the optical setup for LIAD measurements. A Toptica DL Pro laser at 780 nm was used to excite the rubidium atoms in our nano-cell (NC). This excitation laser was stabilised as described in section A.1, and was incident on the cell in a total internal reflection geometry (generating an evanescent field in the vapour region). Fluorescence at 780 nm was recorded using a SPAD. A second laser at 450 nm was used to perform the LIAD and liberate atoms from the cell walls into the vapour phase. Imaging, if required, was done by splitting some light onto a CCD. Other components were: L1 - $f = 100$ mm lenses; L2 - $f = 75$ mm lens; L3 - objective lens (different focal lengths were used depending on the desired experiment); L4 - $f = 100$ mm lens; GT - Glan-Taylor polariser; P - 50 µm pinhole; BS - 50:50 non-polarising beamsplitter (this could be removed to allow all light towards the SPAD); DM - dichroic mirror; FC - fibre coupler; F - 780 nm band-pass filter.

on resonance as described in section A.1. This was used to excite atoms through an evanescent field produced by totally internally reflecting the beam at the back cell wall surface. Fluorescence at 780 nm was collected using the objective lens (L4 in the figure), and recorded using a SPAD. A second laser at 450 nm was used as the activation laser for the LIAD effect. This was an inexpensive Osram diode, and was focused into the cell via the same objective lens as was used to collect atomic fluorescence. A pinhole was used to clean up the beam shape from the Osram diode, whilst a Glan-Taylor polariser was used to clean up the polarisation.

For a typical experiment, the background fluorescence activity was measured before with only the 780 nm laser turned on. Then, the 450 nm laser was turned on for some time, and the atomic fluorescence activity was continually recorded during the turn on and turn off. This produced an activity curve where any increase in activity above the background level would correspond

to an increase in atomic number density.

Appendix B

Quantum jump simulations

The quantum jump method (otherwise known as the Monte Carlo wavefunction method) allows for simulating individual realisations of system dynamics, which can then be averaged to find the full system response. We employed this method for the case of excitation of rubidium atoms in our thin cells using CW laser light in chapter 2, and using pulsed laser light in chapter 6. In this section we will describe the method in detail. Whilst any numerical results presented in this thesis were gained by inputting the relevant parameters for our rubidium atoms, however the method could be applied generally to any similar atomic level scheme.

The evolution of the system is governed by the Schrodinger equation with an effective Hamiltonian

$$H_{\text{eff}} = H_{\text{sys}} - \frac{i\hbar}{2}\sum_i C_n^+ C_n, \tag{B.1}$$

where C_n are collapse operators corresponding to a transition between given states, and H_{sys} is the system Hamiltonian incorporating the Rabi frequencies (Ω) and detunings (Δ) for the transitions in question.

We choose our initial wavefunction $|\psi(0)\rangle = \sum \alpha_i |A_i\rangle$ for states A_i with probabilities α_i^2. It can then be shown that

$$|\psi(t+\delta t)\rangle = \left(1 - \frac{iH_{\text{eff}}\delta t}{\hbar}\right)|\psi(t)\rangle\,. \tag{B.2}$$

Thus we can evolve the system through a set of discrete timesteps, provided that δt is much smaller than the decay lifetime of any particular state. At each timestep we test for a quantum jump, which corresponds to a spontaneous

emission event occurring. For our specific case of thin cell dynamics, we also test for a wall collision at each timestep, and after collision we consider the system to also return to the ground state, through a non-radiative quenching event. A new atom is then added to the model, to simulate the conservation of local atomic number density in the vapour by continuous adsorption and desorption at the cell walls, as well as by atomic motion into and out of the interrogation volume from the surrounding cell.

For all simulations, an ensemble of $10^3 - 10^6$ atoms was initialised. Each atom was assigned a velocity chosen at random from the Maxwell-Boltzmann distribution, and also an initial position within the cell. From this information, the time until the atom collides with a cell wall was calculated. Our simulations constitute a classical wrapper which considers the atomic motional state, combined with internal state calculations handled using the quantum jump method described above. We consider the motional and internal states to be uncoupled.

B.1 Two-level atoms

For the two-level case, we chose to write the problem in the rotation matrix formalism. The rotation matrix is

$$R = \begin{pmatrix} \cos\frac{\theta}{2} - i\frac{\Delta}{\Omega_{\text{eff}}}\sin\frac{\theta}{2} & -\frac{\Omega}{\Omega_{\text{eff}}}\sin\frac{\theta}{2} \\ \frac{\Omega}{\Omega_{\text{eff}}}\sin\frac{\theta}{2} & \cos\frac{\theta}{2} + i\frac{\Delta}{\Omega_{\text{eff}}}\sin\frac{\theta}{2} \end{pmatrix}, \tag{B.3}$$

where $\Omega_{\text{eff}} = \sqrt{\Omega^2 + \Delta^2}$ and $\theta = \Omega_{\text{eff}}\mathrm{d}t$, with $\mathrm{d}t$ the timestep, Δ the detuning, and Ω the Rabi frequency. This Rabi frequency is a time-dependent function, which uses a Gaussian curve centred at 4 ns and with a FWHM of 1.5 ns to model a laser pulse. The peak Rabi frequency is chosen to match experimental values. At each timestep, the rotation matrix is applied to the state of each individual realisation of the system. A random number r is then chosen, and the system is tested for a wall collision or a quantum jump. The latter occurs when the condition $P_{\text{b}}\Gamma\mathrm{d}t > r$ is satisfied, where $\mathrm{d}t$ is the timestep, Γ is the natural decay lifetime, and P_{b} the excited state probability.

Whilst more control and understanding can be gained using the rotation matrix method outlined above, another convenient entry point into Monte Carlo wavefunction modelling is the QuTiP python package [77]. We com-

pared our rotation matrix method outlined above to using the QuTiP *mcsolve* function, and found they both gave the same results with the same input parameters for this two-level system. Due to the complexity of problems with more than two levels, it was decided to use the QuTiP package for further calculations, as outlined in the following section.

B.2 Four-level atoms

To simulate the evolution of an ensemble of four-level atoms, we used the QuTiP *mcsolve* function. We began with the Hamiltonian

$$H = \begin{pmatrix} 0 & \Omega_a/2 & 0 & 0 \\ \Omega_a/2 & -\Delta_a & 0 & \Omega_b/2 \\ 0 & 0 & 0 & 0 \\ 0 & \Omega_b/2 & 0 & -(\Delta_a + \Delta_b) \end{pmatrix}. \tag{B.4}$$

Here Ω_i are the Rabi frequencies for the relevant transitions, which can be time dependent to encapsulate the Gaussian laser pulse. The detunings for each transition are denoted Δ_i, which include the effective detuning $\Delta_{eff} = kv_z$ of each atom from resonance due to the Doppler effect, based on velocity parallel to the laser propagation direction (and perpendicular to the cell confinement direction). We also then defined collapse operators for each possible transition j→i as $C_{ji} = \sqrt{\Gamma_{ji}}\,|i\rangle\langle j|$, where Γ_{ji} is the natural decay rate for this transition. The *mcsolve* function tests for a quantum jump at each timestep in the same way as was described in the previous section, but now for each of the possible transitions defined by their various collapse operators.

B.3 Illustrative test simulation

A graph illustrating the quantum jump method is shown in Fig. B.1, for the two-level atom case. The pulse is shown in green (with arbitrary magnitude), and the temporal dynamics of the excited state probability averaged over all individual realisations of the system is shown in red. Some individual realisations are shown grey (for atoms which did not fluoresce, but could return to the ground state via wall collision) and purple (for atoms which fluoresced). We record the position and velocity of the atoms which fluoresce, which gives

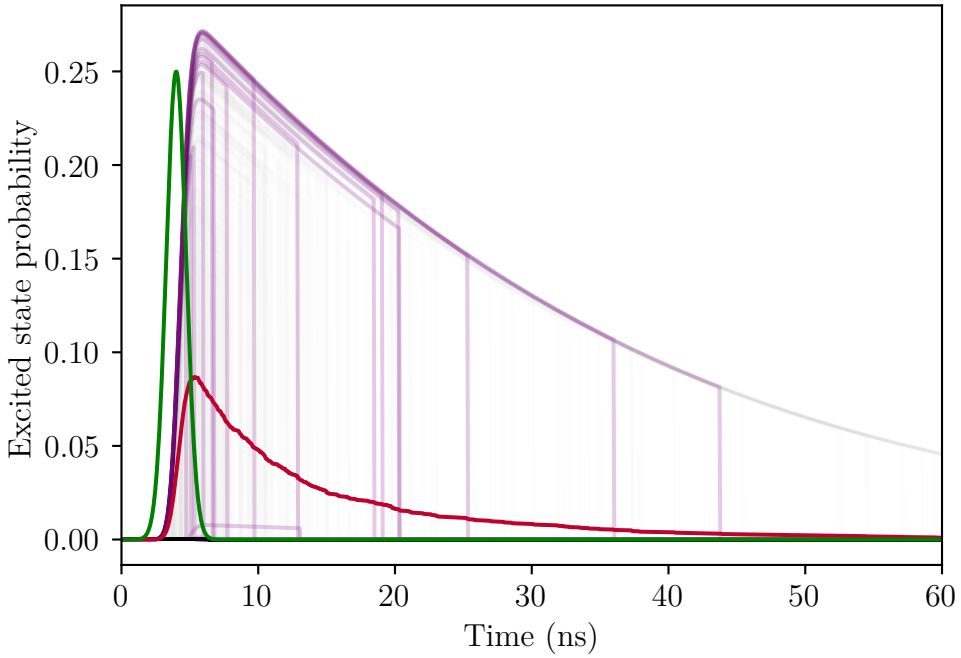

Figure B.1: Excited state probability plot illustrating the Monte Carlo quantum jump simulation method, for 600 atoms in a 1 µm cell subject to a 1.5 ns pulse (shaded green, height is arbitrary) with a peak Rabi frequency of 100 MHz. Individual atomic contributions are shown, in purple for those atoms which perform a quantum jump, and in grey for others (which may de-excite by hitting a wall). The excited state probability averaged over all simulation atoms is shown in red. We found that for a 1 µm cell, 99.9% of atoms hit a wall within the 60 ns simulation, but only 0.8% performed a quantum jump. For comparison, in a 1 mm cell these figures would be 1.7% and 12% respectively.

us further insight on the process and the velocity classes of atoms that are involved. We observe that a significant number of atoms survive for long enough for their individual system realisation to reproduce the 26 ns decay lifetime of the excited state. However, averaging these with the realisations which return to the ground state either through spontaneous decay or a wall collision gives an overall reduced effective lifetime.

The key parameters that we can vary in our simulations and experimentally are: pulse width (and shape), pulse Rabi frequency (which relates to pulse intensity measured in the experiment), cell confinement geometry, excitation beam shape (for e.g. averaging over a laser spot with a Gaussian intensity distribution, or for excitation with an evanescent field). There are other parameters we cannot vary so easily in the experiment, which are coded

into our simulations. For example, our simulations also use the standard parameters for rubidium atoms (but these could be changed to any other alkali metal), and we set the initial velocities of the simulation atoms to be a Maxwell-Boltzmann type distribution. We also set the number of simulation atoms, which is a trade-off between higher resolution simulation results and a longer computation time.

There are numerous initial tests which can be performed to check the validity of the simulation. Perhaps the simplest is to remove the imposition of the thin cell and collisions with the walls, and instead simulating atomic behaviour in a conventional millimetre- or centimetre-sized vapour cell. In this case, for the two-level system we recover the well known 26 ns decay lifetime for the rubidium D2 transition as expected. As discussed previously, for the two-level simulations we also compared the rotation matrix method to the QuTiP python package methods and achieved the same results.

B.4 Python code

Below, a minimal example of the python code used for the four-level quantum jump simulations described in the previous sections is shown.

```
import numpy as np
from scipy.interpolate import interp1d as interp
from scipy.special import erf
import multiprocessing as mp
import psutil
import qutip as qt

def gaussian(x, sigma, x0, a, c):
    gauss = c+a*np.exp((-(x-x0)**2)/(2*sigma**2))
    return gauss

def Lorentzian(x,gamma,x0,a,c):
    return c+ a*gamma**2/((x-x0)**2+gamma**2)

def MB_CDF(v,m,T):
    '''Cumulative distribution function of the
```

```
    Maxwell-Boltzmann speed distribution'''
    kB = 1.38e-23
    a = np.sqrt(kB*T/m)
    b = erf(v/(np.sqrt(2)*a))
    c = np.sqrt(2/np.pi)* v*np.exp(-v**2/(2*a**2))/a
    return b-c

def random_atoms(N_atoms):
    ```Returns arrays: atom speeds (m/s), atom thetas, atom phis.
    Each has length N_atoms.'''
    atom_speed = inv_cdf(np.random.rand(N_atoms)) # from MB dist
    atom_theta = np.arccos(np.random.uniform(-1,1,N_atoms))
    atom_phi = np.random.uniform(0,2*np.pi,N_atoms)
    return atom_speed, atom_theta, atom_phi

def the_mp_subroutine_qutip4lvl(args3):
    ```Subroutine for multiprocessing.'''
    perp_velocity,vx,Omega0,Omega776,times,sigma,z_coords,x_coords,
    y_coords,L,psi_0,hit_times,spotsize,cell_thickness,
    evanescent_depth,atom_i = args3

    #### TIME DEP HAMILTONIAN ####
    # (time dependence in function below)
    H1 = qt.Qobj([[0, 1, 0, 0],
                  [1, 0, 0, 0],
                  [0, 0, 0, 0],
                  [0, 0, 0, 0]])

    ### DETUNINGS
    delta_b = 2*np.pi/780e-9 * perp_velocity[atom_i]
    delta_a = 2*np.pi/776e-9 * perp_velocity[atom_i]

    ### GAUSSIAN AVERAGING
    f = gaussian2D(x_coords[atom_i],y_coords[atom_i],1e-6,0,0,1,0)

    ### HAMILTONIAN (constant part, per atom)
```

```
    H0 = qt.Qobj([[0, 0,                 0,  0],
                  [0,  -delta_b,         0,  Omega776*f/2],
                  [0,  0,                0,  0],
                  [0,  Omega776*f/2, 0,  -(delta_a+delta_b)]])

    def H_timedep(t, args):
        exp1 = np.exp(-0.5*((t-4e-9)/sigma)**2)
        return np.array(1e-15+Omega0*f*exp1)
    H=[H0,[H1,H_timedep]]

    sol = qt.mcsolve(H, psi_0, times[times<hit_times[atom_i]],
    L, [], ntraj=1) # solve until atom hits a wall

    coll_time = sol.col_times
    coll_operator = sol.col_which
    final_state = np.zeros((len(times),4,1),dtype=complex)
    for i, time in enumerate(times):
        if i >= len(times[times<hit_times[atom_i]]):
            final_state[i] = psi_0
        else:
            final_state[i] = sol.states[0,i]

    hit_state = sol.states[0,-1]
    results = [[final_state],coll_time,coll_operator,[hit_state]]
    return np.array(results)

if __name__ == "__main__":
     # create CDF
     vs = np.arange(0,2500,0.1)
     cdf = MB_CDF(vs,mass,T) # essentially y = f(x)

     #create interpolation function to CDF, for picking velocities later
     inv_cdf = interp(cdf,vs)

     #### Parameters ####
     amu = 1.66e-27
```

```
mass = 85*amu # Rb 85

T = 273.15+100 # Temp in K
N_atoms = 5000 # number of sim atoms

npts=7200 # number of timesteps to run simulation over
tmax=720.0e-9 # max time to simulate to (seconds)
times = np.linspace(0,tmax,npts) # set time points

Omega0 = 1e8  # pulse Rabi freq
Omega776 = 1e8 # pulse Rabi freq

fwhm = 1.7e-9 # pulse FWHM
cell_thicknesses = [75e-3] # array of cell thicknesses simulation over
psi_0=qt.basis(4,0) # initial wavefunction
evanescent_depth = np.inf # evanescent field length
# set above to inf for transmitted beam
spotsize = 2e-3 # collection spot size in m

#### Collapse operators ####
gamma10 = 2*np.pi * 6.0666*1e6 # Rb D2 780nm, 26ns lifetime
L10 = np.sqrt(gamma10)*qt.basis(4,0)*qt.basis(4,1).dag()
gamma21 = 1/(235e-9) - 1/(822e-9) #### TEST
L21 = np.sqrt(gamma21)*qt.basis(4,1)*qt.basis(4,3).dag()
gamma23 = 1/(822e-9)
L23 = np.sqrt(gamma23)*qt.basis(4,2)*qt.basis(4,3).dag()
gamma30 = 1/(500e-9)
L30 = np.sqrt(gamma30)*qt.basis(4,0)*qt.basis(4,2).dag()
gamma35 = 1/(113e-9)-1/(500e-9)
L35 = np.sqrt(gamma30)*qt.basis(4,3)*qt.basis(4,2).dag()
Ls = [L10,L21,L23,L30,L35] # all collapse operators for qutip


#### Pulse ####
sigma = fwhm/(2*np.sqrt(2*np.log(2))) # 1/e width of Guassian
Omega = 1e-15+Omega0*np.exp(-0.5*((times-4e-9)/sigma)**2)
```

```
# small offset or sqrt returns NaN   # Gaussian pulse

# do the simulation for each thickness for a number of reps
and average (to improve memory load)
reps = 1

for th in range(len(cell_thicknesses)):
cell_thickness = cell_thicknesses[th]
avg, avg2, avg3, avg4 = 0, 0, 0, 0
jump_times, jump_velocities = [],[]
hit_times_res, perp_velocity_res = [],[]
leave_times_res, leave_times_resy = [],[]
num_decays = 0
for rep in range(reps):
    # initialise random atoms
    atom_speed, atom_theta, atom_phi = random_atoms(N_atoms)

    z_coords = np.random.rand(N_atoms)*cell_thickness
    x_coords = (np.random.rand(N_atoms)-0.5)*1e-3
    y_coords = (np.random.rand(N_atoms)-0.5)*1e-3

    perp_velocity = atom_speed * np.cos(atom_theta)
    vx = atom_speed * np.sin(atom_theta) * np.cos(atom_phi)
    vy = atom_speed * np.sin(atom_theta) * np.sin(atom_phi)
    perp_velocity_res.append(perp_velocity)

    # calculate time to hit wall for each atom
    z_distances = []
    for atom_i in range(len(atom_theta)):
        if perp_velocity[atom_i]>0:
            z_distances.append(cell_thickness-z_coords[atom_i])
        else:
            z_distances.append(z_coords[atom_i])
    hit_times=(z_distances/np.abs(perp_velocity))
    hit_times_res.append(hit_times)
```

```
# calculate time to leave collection spot in x
x_distances = []
for atom_i in range(len(atom_theta)):
    if vx[atom_i]>0:
        x_distances.append(spotsize/2-x_coords[atom_i])
    else:
        x_distances.append(spotsize/2+x_coords[atom_i])
leave_times=(x_distances/np.abs(vx))

# calculate time to leave collection spot in y
y_distances = []
for atom_i in range(len(atom_theta)):
    if vy[atom_i]>0:
        y_distances.append(spotsize/2-y_coords[atom_i])
    else:
        y_distances.append(spotsize/2+y_coords[atom_i])
leave_timesy=(y_distances/np.abs(vy))

for i in range(len(hit_times)): # set time to run sim for
each atom to be the shorter of: time to hit wall and time
to leave collection area
    if hit_times[i]>leave_times[i]:
        hit_times[i]=leave_times[i]
    if hit_times[i]>leave_timesy[i]:
        hit_times[i]=leave_timesy[i]

############ RUN SIMULATION ############

atomsss = range(N_atoms)
args1 = ((perp_velocity,vx,Omega0,Omega776,times,sigma,
          z_coords,x_coords,y_coords,Ls,psi_0,hit_times,
          spotsize,cell_thickness,evanescent_depth,
          atom_i) for atom_i in atomsss)
pool = mp.Pool()

## low priority
```

```
parent = psutil.Process()
parent.nice(psutil.BELOW_NORMAL_PRIORITY_CLASS)
for child in parent.children():
child.nice(psutil.IDLE_PRIORITY_CLASS)

#run multiprocessing loop
#close pool and join
res = pool.map_async(the_mp_subroutine_qutip4lvl,args1)
pool.close()
pool.join()
res1 = np.array(res.get())

final_states = res1[:,0]
col_ops = res1[:,2][:,0]
hit_state2_res = res1[:,3][:,0]
jump_vels_res = res1[:,1][:,0]

for element in range(len(col_ops)):
    if np.array(col_ops[element]).size>0:
        for elementofelement in range(
        len(col_ops[element])):
            if col_ops[element][elementofelement] == 3:
                jump_velocities.append(jump_vels_res
                [element][elementofelement])
                num_decays+=1
    else:
        pass

for k in range(N_atoms):
    final_state = np.array(final_states[k])[0][:,0]
    prob = abs(final_state)**2
    avg+=prob

    final_state2 = np.array(final_states[k])[0][:,1]
    prob2 = abs(final_state2)**2
    avg2+=prob2
```

```
        final_state3 = np.array(final_states[k])[0][:,2]
        prob3 = abs(final_state3)**2
        avg3+=prob3

        final_state4 = np.array(final_states[k])[0][:,3]
        prob4 = abs(final_state4)**2
        avg4+=prob4

    output = np.array([np.array(times).flatten(),
     np.array(avg).flatten(),np.array(avg2).flatten(),
     np.array(avg3).flatten(),np.array(avg4).flatten()])
```

Bibliography

[1] T. F. Cutler, W. J. Hamlyn, J. Renger, K. A. Whittaker, D. Pizzey, I. G. Hughes, V. Sandoghdar, and C. S. Adams. Nanostructured alkali-metal vapor cells. *Phys. Rev. Applied*, 14:034054, Sep 2020. ix, 5, 18, 20, 24, 26, 27, 29, 38, 40, 43, 46, 47, 56, 61, 62, 63, 64, 80, 87, 88, 108, 111

[2] S. Ribeiro, T. F. Cutler, C. S. Adams, and S. A. Gardiner. Collective effects in the photon statistics of thermal atomic ensembles. *Phys. Rev. A*, 104:013719, Jul 2021. ix, 29, 76, 98

[3] M. A. Zentile, J. Keaveney, L. Weller, D. J. Whiting, C. S. Adams, and I. G. Hughes. ElecSus: A program to calculate the electric susceptibility of an atomic ensemble. *Comput. Phys. Commun.*, 189:162–174, Apr 2015. 1, 2, 15, 16, 22, 62

[4] J. Keaveney, S. A. Wrathmall, C. S. Adams, and I. G. Hughes. Optimized ultra-narrow atomic bandpass filters via magneto-optic rotation in an unconstrained geometry. *Opt. Lett.*, 43(17):4272, Sep 2018. 1

[5] F. D. Logue, J. D. Briscoe, D. Pizzey, S. A. Wrathmall, and I. G. Hughes. Better magneto-optical filters with cascaded vapor cells. *Opt. Lett.*, 47(12):2975–2978, Jun 2022. 1

[6] M. Hosseini, B. Sparkes, G. Campbell, P. K. Lam, and B. C. Buchler. High efficiency coherent optical memory with warm rubidium vapour. *Nat. Commun.*, 2:174, Feb 2011. 1

[7] N. Cherroret, M. Hemmerling, V. Nador, J. T. M. Walraven, and R. Kaiser. Robust coherent transport of light in multilevel hot atomic vapors. *Phys. Rev. Lett.*, 122:183203, May 2019. 1, 23

[8] J. Kitching, S. Knappe, and E. A. Donley. Atomic sensors - A review. *IEEE Sens. J.*, 11(9):1749–1758, Sep 2011. 1, 6, 120

[9] J. Keaveney, W. J. Hamlyn, C. S. Adams, and I. G. Hughes. A single-mode external cavity diode laser using an intra-cavity atomic Faraday filter with short-term linewidth <400 kHz and long-term stability of <1 MHz. *Rev. Sci. Instrum.*, 87(9):1–5, Sep 2016. 1

[10] R. S. Mathew, F. Ponciano-Ojeda, J. Keaveney, D. J. Whiting, and I. G. Hughes. Simultaneous two-photon resonant optical laser locking (STROLLing) in the hyperfine Paschen–Back regime. *Opt. Lett.*, 43(17):4204, Sep 2018. 1

[11] F. Ripka, H. Kübler, R. Löw, and T. Pfau. A room-temperature single-photon source based on strongly interacting Rydberg atoms. *Science*, 362(6413):446–449, Oct 2018. 1, 3, 23

[12] L. A. Downes, A. R. MacKellar, D. J. Whiting, C. Bourgenot, C. S. Adams, and K. J. Weatherill. Full-field terahertz imaging at kilohertz frame rates using atomic vapor. *Phys. Rev. X*, 10:011027, Feb 2020. 1

[13] G. Bison, R. Wynands, and A. Weis. Dynamical mapping of the human cardiomagnetic field with a room-temperature, laser-optical sensor. *Opt. Express*, 11(8):904, Apr 2003. 1

[14] M. Mosleh, S. M. Hamidi, and M. Ranjbaran. Multifunctional logic gates based on resonant transmission at atomic-plasmonic structure. *Sci. Rep.*, 12:10734, Jun 2022. 1, 38

[15] R. Ritter, N. Gruhler, W. Pernice, H. Kübler, T. Pfau, and R. Löw. Atomic vapor spectroscopy in integrated photonic structures. *Appl. Phys. Lett.*, 107(4):041101, Jul 2015. 1

[16] P. D. D. Schwindt, S. Knappe, V. Shah, L. Hollberg, J. Kitching, L.-A. Liew, and J. Moreland. Chip-scale atomic magnetometer. *Appl. Phys. Lett.*, 85(26):6409–6411, Dec 2004. 1, 6, 23, 120

[17] J. Kitching. Chip-scale atomic devices. *Appl. Phys. Rev.*, 5(3):031302, Aug 2018. 1, 6

[18] J. Sinclair, D. Angulo, K. Thompson, K. Bonsma-Fisher, A. Brodutch, and A. M. Steinberg. Measuring the time atoms spend in the excited state due to a photon they do not absorb. *PRX Quantum*, 3:010314, Jan 2022. 1

[19] R. Finkelstein, O. Lahad, I. Cohen, O. Davidson, S. Kiriati, E. Poem, and O. Firstenberg. Continuous protection of a collective state from inhomogeneous dephasing. *Phys. Rev. X*, 11:011008, Jan 2021. 2, 16

[20] D. Main, T. M. Hird, S. Gao, E. Oguz, D. J. Saunders, I. A. Walmsley, and P. M. Ledingham. Preparing narrow velocity distributions for quantum memories in room-temperature alkali-metal vapors. *Phys. Rev. A*, 103:043105, Apr 2021. 2, 16

[21] P. Siddons, C. S. Adams, C. Ge, and I. G. Hughes. Absolute absorption on rubidium D lines: comparison between theory and experiment. *J. Phys. B At. Mol. Opt. Phys.*, 41(15):155004, Aug 2008. 2, 12, 15, 17, 66

[22] J. Keaveney, C. S. Adams, and I. G. Hughes. Elecsus: Extension to arbitrary geometry magneto-optics. *Comput. Phys. Commun.*, 224:311 – 324, Mar 2018. 2, 15, 62, 83

[23] D. Jaksch, J. I. Cirac, P. Zoller, S. L. Rolston, R. Côté, and M. D. Lukin. Fast quantum gates for neutral atoms. *Phys. Rev. Lett.*, 85:2208–2211, Sep 2000. 2

[24] T. Aoki, B. Dayan, E. Wilcut, W. P. Bowen, A. S. Parkins, T. J. Kippenberg, K. J. Vahala, and H. J. Kimble. Observation of strong coupling between one atom and a monolithic microresonator. *Nature*, 443(7112):671–674, Oct 2006. 2

[25] M. P. A. Jones, J. Beugnon, A. Gaëtan, J. Zhang, G. Messin, A. Browaeys, and P. Grangier. Fast quantum state control of a single trapped neutral atom. *Phys. Rev. A*, 75:040301, Apr 2007. 2

[26] R. Bourgain, J. Pellegrino, S. Jennewein, Y. R. P. Sortais, and A. Browaeys. Direct measurement of the Wigner time delay for the scattering of light by a single atom. *Opt. Lett.*, 38(11):1963–1965, Jun 2013. 2, 76

[27] A. Reiserer and G. Rempe. Cavity-based quantum networks with single atoms and optical photons. *Rev. Mod. Phys.*, 87(4):1379–1418, Dec 2015. 2

[28] H. J. Kimble, M. Dagenais, and L. Mandel. Photon antibunching in resonance fluorescence. *Phys. Rev. Lett.*, 39:691–695, Sep 1977. 3

[29] J. Keaveney, A. Sargsyan, U. Krohn, I. G. Hughes, D. Sarkisyan, and C. S. Adams. Cooperative Lamb shift in an atomic vapor layer of nanometer thickness. *Phys. Rev. Lett.*, 108(17):173601, Apr 2012. 3, 5, 21, 23, 29

[30] R. J. Bettles. *Cooperative Interactions in Lattices of Atomic Dipoles*. PhD thesis, Durham University, 2016. 3, 21, 28

[31] F. Christaller, M. Mäusezahl, F. Moumtsilis, A. Belz, H. Kübler, H. Alaeian, C. S. Adams, R. Löw, and T. Pfau. Transient density-induced dipolar interactions in a thin vapor cell. *Phys. Rev. Lett.*, 128:173401, Apr 2022. 3, 45

[32] L. A. Williamson, M. O. Borgh, and J. Ruostekoski. Superatom picture of collective nonclassical light emission and dipole blockade in atom arrays. *Phys. Rev. Lett.*, 125:073602, Aug 2020. 3

[33] M. D. Lukin, M. Fleischhauer, R. Cote, L. M. Duan, D. Jaksch, J. I. Cirac, and P. Zoller. Dipole blockade and quantum information processing in mesoscopic atomic ensembles. *Phys. Rev. Lett.*, 87:037901, Jun 2001. 3

[34] T. Peyrot, Y. R. P. Sortais, A. Browaeys, A. Sargsyan, D. Sarkisyan, J. Keaveney, I. G. Hughes, and C. S. Adams. Collective Lamb Shift of a Nanoscale Atomic Vapor Layer within a Sapphire Cavity. *Phys. Rev. Lett.*, 120(24):243401, Jun 2018. 3, 5, 21, 23

[35] V. O. Lorenz, X. Dai, H. Green, T. R. Asnicar, and S. T. Cundiff. High-density, high-temperature alkali vapor cell. *Rev. Sci. Instrum.*, 79(12):123104, Dec 2008. 3, 43

[36] H. Dobbertin, R. Löw, and S. Scheel. Collective dipole-dipole interactions in planar nanocavities. *Phys. Rev. A*, 102:031701, Sep 2020. 3, 5, 6, 29

[37] J. Keaveney. *Cooperative interactions in dense thermal Rb vapour confined in nm-scale cells*. PhD thesis, Durham University, 2013. 4, 19, 61, 75, 76, 80, 91, 122

[38] C. B. Alcock, V. P. Itkin, and M. K. Horrigan. Vapour pressure equations for the metallic elements: 298–2500K. *Can. Metall. Q.*, 23(3):309–313, 1984. 4, 43, 72

[39] M. Fichet, F. Schuller, D. Bloch, and M. Ducloy. Van der Waals interactions between excited-state atoms and dispersive dielectric surfaces. *Phys. Rev. A*, 51:1553–1564, Feb 1995. 5, 39

[40] C. Henkel and V. Sandoghdar. Single-molecule spectroscopy near structured dielectrics. *Opt. Commun.*, 158(1):250–262, Dec 1998. 5

[41] D. M. Harber, J. M. McGuirk, J. M. Obrecht, and E. A. Cornell. Thermally induced losses in ultra-cold atoms magnetically trapped near room-temperature surfaces. *J. Low Temp. Phys.*, 133(3):229–238, Nov 2003. 5

[42] D. Bloch and M. Ducloy. Atom-wall interaction. In *Adv. At. Mol. Opt. Phys.*, volume 50, pages 91–154. Academic Press, Jan 2005. 5

[43] T. A. Vartanyan, A. E. Logunov, A. S. Pazgalev, S. G. Przhibel'skii, Sarkisyan D., and V. V. Khromov. Change in the states of optically excited Rb atoms near sapphire surface. *Opt. Spectrosc.*, 115:60–67, Jul 2013. 5, 39

[44] A. S. Prasad, J. Hinney, S. Mahmoodian, K. Hammerer, S. Rind, P. Schneeweiss, A. S. Sørensen, J. Volz, and A. Rauschenbeutel. Correlating photons using the collective nonlinear response of atoms weakly coupled to an optical mode. *Nat. Photonics*, 14:719–722, Sep 2020. 5, 29

[45] M. Fichet, G. Dutier, A. Yarovitsky, P. Todorov, I. Hamdi, I. Maurin, S. Saltiel, D. Sarkisyan, M.-P Gorza, D. Bloch, and M. Ducloy. Exploring the van der Waals atom-surface attraction in the nanometric range. *Europhys. Lett.*, 77(5):54001, Mar 2007. 5, 23, 61

[46] K. A. Whittaker, J. Keaveney, I. G. Hughes, A. Sargsyan, D. Sarkisyan, and C. S. Adams. Optical Response of Gas-Phase Atoms at Less than $\lambda/80$ from a Dielectric Surface. *Phys. Rev. Lett.*, 112(25):253201, Jun 2014. 5, 16, 23, 61

[47] T. Peyrot, N. Šibalić, Y. R. P. Sortais, A. Browaeys, A. Sargsyan, D. Sarkisyan, I. G. Hughes, and C. S. Adams. Measurement of the atom-surface van der waals interaction by transmission spectroscopy in a wedged nanocell. *Phys. Rev. A*, 100:022503, Aug 2019. 5, 16, 22

[48] W. Yang, D. B. Conkey, B. Wu, D. Yin, A. R. Hawkins, and H. Schmidt. Atomic spectroscopy on a chip. *Nat. Photon.*, 1:331–335, Jun 2007. 5

[49] J.P. McGilligan, P.F. Griffin, R. Elvin, S. J. Ingleby, E. Riis, and A. S. Arnold. Grating chips for quantum technologies. *Sci. Rep.*, 7:384, Mar 2017. 5

[50] J. P. McGilligan, K. R. Moore, A. Dellis, G. D. Martinez, E. de Clercq, P. F. Griffin, A. S. Arnold, E. Riis, R. Boudot, and J. Kitching. Laser cooling in a chip-scale platform. *Appl. Phys. Lett.*, 117(5):054001, Aug 2020. 5

[51] A. Gusching, M. Petersen, N. Passilly, D. Brazhnikov, M. Abdel Hafiz, and R. Boudot. Short-term stability of Cs microcell-stabilized lasers using dual-frequency sub-Doppler spectroscopy. *J. Opt. Soc. Am. B*, 38(11):3254–3260, Nov 2021. 5

[52] A. Naiman, Y. Sebbag, E. Talker, Y. Barash, L. Stern, and U. Levy. Large cooperativity in strongly coupled chip-scale photonic-atomic integrated system, Nov 2021. 5

[53] E. Edrei, N. Cohen, E. Gerstel, S. Gamzu-Letova, N. Mazurski, and U. Levy. Chip-scale atomic wave-meter enabled by machine learning. *Sci. Adv.*, 8(15):eabn3391, Apr 2022. 5, 6

[54] P. Ruchka, S. Hammer, M. Rockenhäuser, R. Albrecht, J. Drozella, S. Thiele, H. Giessen, and T. Langen. Microscopic 3D printed optical tweezers for atomic quantum technology. *Quantum Sci. Technol.*, Jul 2022. 5

[55] K. Gallacher, P. F. Griffin, E. Riis, M. Sorel, and D. J. Paul. Silicon nitride waveguide polarization rotator and polarization beam splitter for chip-scale atomic systems. *APL Photonics*, 7(4):046101, Apr 2022. 5

[56] S. Karlen, J. Gobet, T. Overstolz, J. Haesler, and S. Lecomte. Lifetime assessment of RbN_3-filled MEMS atomic vapor cells with Al_2O_3 coating. *Opt. Express*, 25(3):2187–2194, Feb 2017. 6, 23, 120

[57] S. Knappe, P. Schwindt, V. Shah, L. Hollberg, J. Kitching, L. Liew, and J. Moreland. A chip-scale atomic clock based on 87Rb with improved frequency stability. *Opt. Express*, 13(4):1249–53, Feb 2005. 6

[58] M. V. Balabas, D. Budker, J. Kitching, P. D. D. Schwindt, and J. E. Stalnaker. Magnetometry with millimeter-scale antirelaxation-coated alkali-metal vapor cells. *J. Opt. Soc. Am. B*, 23(6):1001, Jun 2006. 6, 120

[59] S. Liron, D. G. Bopp, S. A. Schima, V. N. Maurice, and J. E. Kitching. Chip-scale atomic diffractive optical elements. *Nat. Commun.*, 10(1):3156, Dec 2019. 6, 119

[60] R. Zektzer, N. Mazurski, Y. Barash, and U. Levy. Nanoscale atomic suspended waveguides for improved vapour coherence times and optical frequency referencing. *Nat. Photon.*, 15:772–779, Aug 2021. 6

[61] A. Skljarow, H. Kübler, C. S. Adams, T. Pfau, R. Löw, and H. Alaeian. Purcell-enhanced dipolar interactions in nanostructures. *Phys. Rev. Research*, 4:023073, Apr 2022. 6, 119

[62] S. M. Spillane, G. S. Pati, K. Salit, M. Hall, P. Kumar, R. G. Beausoleil, and M. S. Shahriar. Observation of nonlinear optical interactions of ultralow levels of light in a tapered optical nanofiber embedded in a hot rubidium vapor. *Phys. Rev. Lett.*, 100:233602, Jun 2008. 6

[63] A. R. Bhagwat and A. L. Gaeta. Nonlinear optics in hollow-core photonic bandgap fibers. *Opt. Express*, 16(7):5035, Mar 2008. 6, 70

[64] J. Henningsen and J. Hald. Dynamics of gas flow in hollow core photonic bandgap fibers. *Appl. Opt.*, 47(15):2790–2797, May 2008. 6

[65] D. Budker and M. Romalis. Optical magnetometry. *Nat. Phys.*, 3(4):227–234, Apr 2007. 6

[66] V. K. Shah and R. T. Wakai. A compact, high performance atomic magnetometer for biomedical applications. *Phys. Med. Biol.*, 58(22):8153–8161, Nov 2013. 6

[67] G. Bison, N. Castagna, A. Hofer, P. Knowles, J. L. Schenker, M. Kasprzak, H. Saudan, and A. Weis. A room temperature 19-channel magnetic field mapping device for cardiac signals. *Appl. Phys. Lett.*, 95(17):173701, Oct 2009. 6

[68] T. H. Sander, J. Preusser, R. Mhaskar, J. Kitching, L. Trahms, and S. Knappe. Magnetoencephalography with a chip-scale atomic magnetometer. *Biomed. Opt. Express*, 3(5):981, May 2012. 6

[69] R. Wyllie, M. Kauer, R. T. Wakai, and T. G. Walker. Optical magnetometer array for fetal magnetocardiography. *Opt. Lett.*, 37(12):2247, Jun 2012. 6

[70] E. Boto, S. S. Meyer, V. Shah, O. Alem, S. Knappe, P. Kruger, T. M. Fromhold, M. Lim, P. M. Glover, P. G. Morris, R. Bowtell, G. R. Barnes, and M. J. Brookes. A new generation of magnetoencephalography: Room temperature measurements using optically-pumped magnetometers. *Neuroimage*, 149:404–414, Apr 2017. 6

[71] J. U. Sutter, O. Lewis, C. Robinson, A. McMahon, R. Boyce, R. Bragg, A. Macrae, J. Orton, V. Shah, S. J. Ingleby, P. F. Griffin, and E. Riis. Recording the heart beat of cattle using a gradiometer system of optically pumped magnetometers. *Comput. Electron. Agric.*, 177:105651, Oct 2020. 6

[72] E. Klinger, H. Azizbekyan, A. Sargsyan, C. Leroy, D. Sarkisyan, and A. Papoyan. Proof of the feasibility of a nanocell-based wide-range optical magnetometer. *Appl. Opt.*, 59(8):2231–2237, Mar 2020. 7, 61, 120

[73] M. Auzinsh, A. Sargsyan, A. Tonoyan, C. Leroy, R. Momier, D. Sarkisyan, and A. Papoyan. Wide range linear magnetometer based

on a sub-microsized K vapor cell. *Appl. Opt.*, 61(19):5749–5754, Jul 2022. 7

[74] F. Maucher, S. Skupin, S. A. Gardiner, and I. G. Hughes. Creating complex optical longitudinal polarization structures. *Phys. Rev. Lett.*, 120:163903, Apr 2018. 7

[75] M. S. Safronova, C. J. Williams, and C. W. Clark. Relativistic many-body calculations of electric-dipole matrix elements, lifetimes, and polarizabilities in rubidium. *Phys. Rev. A*, 69:022509, Feb 2004. 11, 12, 103, 104, 110

[76] G Lindblad. On the generators of quantum dynamical semigroups. *Commun. Math. Phys.*, 48:119–130, Jun 1976. 13

[77] J. R. Johansson, P. D. Nation, and F. Nori. Qutip: An open-source python framework for the dynamics of open quantum systems. *Comput. Phys. Commun.*, 183(8):1760–1772, Aug 2012. 13, 17, 77, 133

[78] H. B. G. Casimir and D. Polder. The influence of retardation on the london-van der waals forces. *Phys. Rev.*, 73:360–372, Feb 1948. 15

[79] A. Sargsyan, G. Pichler, and D. Sarkisyan. Study of the interaction of potassium atoms with the sapphire surface with the use of an ultrathin spectroscopic cell. *Jetp Lett.*, 115:312–317, May 2022. 16

[80] R. H. Dicke. The effect of collisions upon the Doppler width of spectral lines. *Phys. Rev.*, 89(2):472–473, Sep 1953. 16, 75

[81] S. Briaudeau, S. Saltiel, G. Nienhuis, D. Bloch, and M. Ducloy. Coherent doppler narrowing in a thin vapor cell: Observation of the Dicke regime in the optical domain. *Phys. Rev. A*, 57:R3169–R3172, May 1998. 17

[82] W. J. Hamlyn. *A new platform for atom-light interactions on the nanoscale*. PhD thesis, Durham University, 2020. 18, 25, 40, 45, 61, 63, 72, 98, 100, 101, 111, 118

[83] W. Demtröder. *Laser Spectroscopy*. Springer Berlin Heidelberg, 2008. 20

[84] A. D. Slepkov, A. R. Bhagwat, V. Venkataraman, P. Londero, and A. L. Gaeta. Spectroscopy of Rb atoms in hollow-core fibers. *Phys. Rev. A*, 81:053825, May 2010. 20, 21, 61

[85] D. E. Chang, Jun Ye, and M. D. Lukin. Controlling dipole-dipole frequency shifts in a lattice-based optical atomic clock. *Phys. Rev. A*, 69:023810, Feb 2004. 21

[86] R. J. Bettles, S. A. Gardiner, and C. S. Adams. Cooperative ordering in lattices of interacting two-level dipoles. *Phys. Rev. A*, 92:063822, Dec 2015. 21, 28

[87] R. J. Bettles, S. A. Gardiner, and C. S. Adams. Enhanced optical cross section via collective coupling of atomic dipoles in a 2D array. *Phys. Rev. Lett.*, 116:103602, Mar 2016. 21, 28

[88] E. Shahmoon, D. S. Wild, M. D. Lukin, and S. F. Yelin. Cooperative resonances in light scattering from two-dimensional atomic arrays. *Phys. Rev. Lett.*, 118:113601, Mar 2017. 21

[89] J. Marek. Observation of superradiance in Rb vapour. *J. Phys. B At. Mol. Phys.*, 12(7):L229–L234, Apr 1979. 21

[90] M. Gross and S. Haroche. Superradiance: An essay on the theory of collective spontaneous emission. *Phys. Rep.*, 93(5):301–396, Dec 1982. 21

[91] T. Bienaimé, N. Piovella, and R. Kaiser. Controlled Dicke Subradiance from a Large Cloud of Two-Level Systems. *Phys. Rev. Lett.*, 108:123602, Mar 2012. 21

[92] M. L. Citron, H. R. Gray, C. W. Gabel, and C. R. Stroud. Experimental study of power broadening in a two-level atom. *Phys. Rev. A*, 16:1507–1512, Oct 1977. 21, 83

[93] L. Weller, R. J. Bettles, P. Siddons, C. S. Adams, and I. G. Hughes. Absolute absorption on the rubidium D1 line including resonant dipole–dipole interactions. *J. Phys. B At. Mol. Opt. Phys.*, 44(19):195006, Sep 2011. 22

[94] A. V. Ermolaev and T. A. Vartanyan. Theory of thin-vapor-layer linear-optical properties: The case of quenching of atomic polarization upon collisions of atoms with dielectric walls. *Phys. Rev. A*, 105:013518, Jan 2022. 22

[95] F. Benabid, F. Couny, J. C. Knight, T. A. Birks, and P. St. J. Russell. Compact, stable and efficient all-fibre gas cells using hollow-core photonic crystal fibres. *Nature*, 434:488–491, Mar 2005. 23

[96] N. Sekiguchi, T. Sato, K. Ishikawa, and A. Hatakeyama. Spectroscopic study of a diffusion-bonded sapphire cell for hot metal vapors. *Appl. Opt.*, 57(1):52–56, Jan 2018. 23

[97] V. Maurice, C. Carlé, S. Keshavarzi, R. Chutani, S. Queste, L. Gauthier-Manuel, J.-M. Cote, R. Vicarini, M. A. Hafiz, R. Boudot, and N. Passilly. Laser-actuated hermetic seals for integrated atomic devices, May 2022. arXiv:2205.10440. 23

[98] S. Knappe, V. Velichansky, H. G. Robinson, J. Kitching, and L. Hollberg. Compact atomic vapor cells fabricated by laser-induced heating of hollow-core glass fibers. *Rev. Sci. Instrum.*, 74(6):3142–3145, May 2003. 23

[99] E. J. Eklund, A. M. Shkel, S. Knappe, D. Donley, and J. Kitching. Glass-blown spherical microcells for chip-scale atomic devices. *Sens. Actuator A Phys*, 143(1):175–180, May 2008. 23

[100] V. Maurice, J. Rutkowski, E. Kroemer, S. Bargiel, N. Passilly, R. Boudot, C. Gorecki, L. Mauri, and M. Moraja. Microfabricated vapor cells filled with a cesium dispensing paste for miniature atomic clocks. *Appl. Phys. Lett.*, 110(16):164103, Apr 2017. 23

[101] V. G. Lucivero, A. Zanoni, G. Corrielli, R. Osellame, and M. W. Mitchell. Laser-written vapor cells for chip-scale atomic sensing and spectroscopy. *Opt. Express*, 30(15):27149–27163, Jul 2022. 23, 120

[102] S. Dyer, P. F. Griffin, A. S. Arnold, F. Mirando, D. P. Burt, E. Riis, and J. P. McGilligan. Micro-machined deep silicon atomic vapor cells. *J. Appl. Phys.*, 132(13):134401, 2022. 23

[103] L.-A. Liew, S. Knappe, J. Moreland, H. Robinson, L. Hollberg, and J. Kitching. Microfabricated alkali atom vapor cells. *Appl. Phys. Lett.*, 84(14):2694–2696, Apr 2004. 23

[104] T. Baluktsian, C. Urban, T. Bublat, H. Giessen, R. Löw, and T. Pfau. Fabrication method for microscopic vapor cells for alkali atoms. *Opt. Lett.*, 35(12):1950, Jun 2010. 23

[105] D. Sarkisyan, D. Bloch, A. Papoyan, and M. Ducloy. Sub-Doppler spectroscopy by sub-micron thin Cs vapour layer. *Opt. Commun.*, 200(1):201–208, Dec 2001. 23, 75

[106] A. Sargsyan, A. Papoyan, I. G. Hughes, C. S. Adams, and D. Sarkisyan. Selective reflection from an Rb layer with a thickness below $\lambda/12$ and applications. *Opt. Lett.*, 42(8):1476–1479, Apr 2017. 23, 61

[107] G. Dutier, A. Yarovitski, S. Saltiel, A. Papoyan, D. Sarkisyan, D. Bloch, and M. Ducloy. Collapse and revival of a Dicke-type coherent narrowing in a sub-micron thick vapor cell transmission spectroscopy. *Europhys. Lett.*, 63(1):35–41, Jul 2003. 23, 75

[108] K. A. Whittaker. *Construction and characterisation of ultra-thin alkali-metal vapour cells*. PhD thesis, Durham University, 2017. 23, 25, 61, 122

[109] T. Peyrot, Ch. Beurthe, S. Coumar, M. Roulliay, K. Perronet, P. Bonnay, C. S. Adams, A. Browaeys, and Y. R. P. Sortais. Fabrication and characterization of super-polished wedged borosilicate nano-cells. *Opt. Lett.*, 44(8):1940–1943, Apr 2019. 24, 27

[110] E. Talker, R. Zektzer, Y. Barash, N. Mazurski, and U. Levy. Atomic spectroscopy and laser frequency stabilization with scalable micrometer and sub-micrometer vapor cells. *J. Vac. Sci. Technol. B*, 38(5):050601, Aug 2020. 24

[111] M. Alexe and U. Gösele. *Wafer Bonding: Applications and Technology*. Physics and astronomy online library. Springer, 2004. 24

[112] O. Kozlova, S. Guérandel, and E. de Clercq. Temperature and pressure shift of the Cs clock transition in the presence of buffer gases: Ne, N_2, Ar. *Phys. Rev. A*, 83:062714, Jun 2011. 26

[113] R. H. Dicke. Coherence in spontaneous radiation processes. *Phys. Rev.*, 93:99–110, Jan 1954. 28

[114] R. J. Bettles, S. A. Gardiner, and C. S. Adams. Cooperative eigenmodes and scattering in one-dimensional atomic arrays. *Phys. Rev. A*, 94:043844, Oct 2016. 28

[115] D. E. Chang, J. S. Douglas, A. González-Tudela, C.-L. Hung, and H. J. Kimble. Colloquium: Quantum matter built from nanoscopic lattices of atoms and photons. *Rev. Mod. Phys.*, 90:031002, Aug 2018. 29

[116] R. Alaee, A. Safari, and R. W. Boyd. Selective excitation of subwavelength atomic clouds. *Phys. Rev. Research*, 3:023217, Jun 2021. 29

[117] S. Ribeiro and S. A. Gardiner. Quantum emission of light with densely packed driven dipoles. *Phys. Rev. A*, 105:L021701, Feb 2022. 29, 98

[118] Z. Chen, W. Li, R. Li, Y. Zhang, G. Xu, and H. Cheng. Fabrication of highly transparent and conductive indium–tin oxide thin films with a high figure of merit via solution processing. *Langmuir*, 29(45):13836–13842, Oct 2013. 32

[119] P. F. Griffin, K. J. Weatherill, and C. S. Adams. Fast switching of alkali atom dispensers using laser-induced heating. *Rev. Sci. Instrum.*, 76(9):093102, Sep 2005. 34

[120] K. R. Rusimova, D. Slavov, F. Pradaux-Caggiano, J. T. Collins, S. N. Gordeev, D. R. Carbery, W. J. Wadsworth, P. J. Mosley, and V. K. Valev. Atomic dispensers for thermoplasmonic control of alkali vapor pressure in quantum optical applications. *Nat. Commun*, 10:2328, May 2019. 34, 37

[121] K. T. Kaczmarek, D. J. Saunders, M. R. Sprague, S. W. Kolthammer, A. Feizpour, P. M. Ledingham, B. Brecht, E. Poem, I. A. Walmsley, and J. Nunn. Ultrahigh and persistent optical depths of cesium in Kagomé-type hollow-core photonic crystal fibers. *Opt. Lett.*, 40(23):5582–5585, Dec 2015. 34, 44, 51

[122] E. Talker, P. Arora, R. Zektzer, Y. Sebbag, M. Dikopltsev, and U. Levy. Light-induced atomic desorption in microfabricated vapor cells for demonstrating quantum optical applications. *Phys. Rev. Applied*, 15:L051001, May 2021. 34, 44

[123] J. E. Lennard-Jones. Processes of adsorption and diffusion on solid surfaces. *Trans. Faraday Soc.*, 28:333–359, Jan 1932. 35

[124] D. Grischkowsky. Angular and velocity distribution of desorbed sodium atoms. *Appl. Phys. Lett.*, 36(8):711–713, Jul 1980. 35

[125] J. Ma, A. Kishinevski, Y.-Y. Jau, C. Reuter, and W. Happer. Modification of glass cell walls by rubidium vapor. *Phys. Rev. A*, 79:042905, Apr 2009. 35

[126] S. J. Seltzer and M. V. Romalis. High-temperature alkali vapor cells with antirelaxation surface coatings. *J. Appl. Phys.*, 106(11):114905, Dec 2009. 43, 120

[127] K. R. Rusimova, D. Slavov, F. Pradaux-Caggiano, J. T. Collins, S. N. Gordeev, D. R. Carbery, W. J. Wadsworth, P. J. Mosley, and V. K. Valev. Atomic dispensers for thermoplasmonic control of alkali vapor pressure in quantum optical applications. *Nat. Commun.*, 10:2328, May 2019. 44

[128] A. Gozzini, F. Mango, J. H. Xu, G. Alzetta, F. Maccarrone, and R. A. Bernheim. Light-induced ejection of alkali atoms in polysiloxane coated cells. *Il Nuovo Cimento D*, 15:709–722, May 1993. 44

[129] E. Mariotti, S. Atutov, M. Meucci, P. Bicchi, C. Marinelli, and L. Moi. Dynamics of rubidium light-induced atom desorption (LIAD). *Chem. Phys.*, 187(1):111–115, Sep 1994. 44

[130] B. P. Anderson and M. A. Kasevich. Loading a vapor-cell magneto-optic trap using light-induced atom desorption. *Phys. Rev. A*, 63:023404, Jan 2001. 44

[131] S. N. Atutov, R. Calabrese, V. Guidi, B. Mai, A. G. Rudavets, E. Scansani, L. Tomassetti, V. Biancalana, A. Burchianti, C. Marinelli, E. Mariotti, L. Moi, and S. Veronesi. Fast and efficient loading of a

Rb magneto-optical trap using light-induced atomic desorption. *Phys. Rev. A*, 67:053401, May 2003. 44

[132] S. Du, M. B. Squires, Y. Imai, L. Czaia, R. A. Saravanan, V. Bright, J. Reichel, T. W. Hänsch, and D. Z. Anderson. Atom-chip Bose-Einstein condensation in a portable vacuum cell. *Phys. Rev. A*, 70:053606, Nov 2004. 44

[133] S. Ghosh, A. R. Bhagwat, C. K. Renshaw, S. Goh, A. L. Gaeta, and B. J. Kirby. Low-light-level optical interactions with rubidium vapor in a photonic band-gap fiber. In *Slow and Fast Light*, page TuB5. Optical Society of America, Jul 2006. 44

[134] A. D. Slepkov, A. R. Bhagwat, V. Venkataraman, P. Londero, and A. L. Gaeta. Generation of large alkali vapor densities inside bare hollow-core photonic band-gap fibers. *Opt. Express*, 16(23):18976–18983, Nov 2008. 44

[135] E. B. Alexandrov, M. V. Balabas, D. Budker, D. English, D. F. Kimball, C.-H. Li, and V. V. Yashchuk. Light-induced desorption of alkali-metal atoms from paraffin coating. *Phys. Rev. A*, 66:042903, Oct 2002. 44

[136] K. Rebilas and M. J. Kasprowicz. Reexamination of the theory of light-induced atomic desorption. *Phys. Rev. A*, 79:042903, Apr 2009. 44

[137] L. Torralbo-Campo, G. D. Bruce, Giuseppe S., and D. Cassettari. Fast and efficient loading of a Rb magneto-optical trap using light-induced atomic desorption. *Sci. Rep.*, 5:14729, Oct 2015. 44

[138] K. Kitagami, K. Hosumi, K. Goto, and A. Hatakeyama. Quantitative measurements of light-induced desorption of rubidium atoms from quartz substrates. *Phys. Rev. A*, 85:062901, Jun 2012. 44, 49, 121

[139] P. A. Petrov, A. S. Pazgalev, M. A. Burkova, and T. A. Vartanyan. Photodesorption of rubidium atoms from a sapphire surface. *Opt. Spectrosc.*, 123:574–577, Oct 2017. 44

[140] M. Taslakov, S. Tsvetkov, and S. Gateva. Light-induced atomic desorption under different types of illumination. *J. Phys. Conf. Ser.*, 514:012028, May 2014. 44

[141] A. Burchianti, A. Bogi, C. Marinelli, E. Mariotti, and L. Moi. Light-induced atomic desorption and related phenomena. *Physica Scripta*, T135:014012, Jul 2009. 44, 46, 54, 56

[142] S. Villalba, H. Failache, and A. Lezama. Light-induced atomic desorption and diffusion of Rb from porous alumina. *Phys. Rev. A*, 81:032901, Mar 2010. 44

[143] R. Kumagai and A. Hatakeyama. Light-induced atom desorption from glass surfaces characterized by X-ray photoelectron spectroscopy. *Appl. Phys. B*, 122:186, Jun 2016. 44, 46

[144] T. Karaulanov, M. T. Graf, D. English, S. M. Rochester, Y. J. Rosen, K. Tsigutkin, D. Budker, E. B. Alexandrov, M. V. Balabas, D. F. Jackson Kimball, F. A. Narducci, S. Pustelny, and V. V. Yashchuk. Controlling atomic vapor density in paraffin-coated cells using light-induced atomic desorption. *Phys. Rev. A*, 79:012902, Jan 2009. 44

[145] S. Tsvetkov, M. Taslakov, and S. Gateva. Dynamics of the light-induced atomic desorption at homogeneous illumination. *Appl. Phys. B*, 123:92, Mar 2017. 44

[146] S. N. Atutov, F. A. Benimetskii, and A. O. Makarov. Influence of the bulk diffusion of rubidium and sodium atoms in glass on their surface dwell time. *Optoelectron. Instrument. Proc.*, 53:278–287, Aug 2017. 45

[147] V. V. Andreev, D. V. Ignat'ev, and G. G. Telegin. Collective migration of adsorbed atoms on a solid surface in the laser radiation field. *Quantum Electronics*, 34(2):125–128, Feb 2004. 46, 56

[148] A. Burchianti, A. Bogi, C. Marinelli, C. Maibohm, E. Mariotti, and L. Moi. Reversible light-controlled formation and evaporation of rubidium clusters in nanoporous silica. *Phys. Rev. Lett.*, 97:157404, Oct 2006. 46

[149] A. R. Bhagwat, A. D. Slepkov, V. Venkataraman, P. Londero, and A. L. Gaeta. On-demand all-optical generation of controlled Rb-vapor densities in photonic-band-gap fibers. *Phys. Rev. A*, 79:063809, Jun 2009. 51

[150] A. Burchianti, A. Bogi, C. Marinelli, E. Mariotti, and L. Moi. Optical recording in Rb loaded-porous glass by reversible photoinduced phase transformations. *Opt. Express*, 16(2):1377–1384, Jan 2008. 56

[151] J. P. Woerdman and M. F. H. Schuurmans. Spectral narrowing of selective reflection from sodium vapour. *Opt. Commun.*, 14(2):248 – 251, Jun 1975. 61

[152] D. Sarkisyan, T. Varzhapetyan, A. Sarkisyan, Yu. Malakyan, A. Papoyan, A. Lezama, D. Bloch, and M. Ducloy. Spectroscopy in an extremely thin vapor cell: Comparing the cell-length dependence in fluorescence and in absorption techniques. *Phys. Rev. A*, 69:065802, Jun 2004. 61

[153] T. Kawalec, L. Józefowski, J. Fiutowski, M. J. Kasprowicz, and T. Dohnalik. Spectroscopic measurements of the evanescent wave polarization state. *Opt. Commun.*, 274(2):341–346, Jun 2007. 62

[154] M. Mosleh, M. Ranjbaran, and S. M. Hamidi. Trace of evanescent wave polarization by atomic vapor spectroscopy. *Sci. Rep.*, 11:21668, Nov 2021. 62

[155] J. Marek and P. Munster. Radiative lifetimes of excited states of rubidium up to quantum number $n = 12$. *J. Phys. B: At. Mol. Opt. Phys.*, 13(9):1731–1741, May 1980. 63

[156] D. Sheng, A. Pérez Galván, and L. A. Orozco. Lifetime measurements of the $5d$ states of rubidium. *Phys. Rev. A*, 78:062506, Dec 2008. 63

[157] A. Vernier, S. Franke-Arnold, E. Riis, and A. S. Arnold. Enhanced frequency up-conversion in Rb vapor. *Opt. Express*, 18(16):17020–17026, Aug 2010. 63

[158] W. Raja, M. S. Ali, A. Chakrabarti, and A. Ray. The blue light indicator in rubidium 5S–5P–5D cascade excitation. *Appl. Phys. B*, 123:202, Jun 2017. 63

[159] W. Raja, P. K. Mandal, V. Naik, A. Chakrabarti, and A. Ray. The blue light in a ladder system: from double resonance optical pumping to Autler-Townes splitting. *Eur. Phys. J. D*, 72:123, Jul 2018. 63

[160] M. B. Kienlen, N. T. Holte, H. A. Dassonville, A. M. C. Dawes, K. D. Iversen, R. M. McLaughlin, and S. K. Mayer. Collimated blue light generation in rubidium vapor. *Am. J. Phys.*, 81(6):442–449, May 2013. 63

[161] C. Perrella, P. S. Light, J. D. Anstie, T. M. Stace, F. Benabid, and A. N. Luiten. High-resolution two-photon spectroscopy of rubidium within a confined geometry. *Phys. Rev. A*, 87:013818, Jan 2013. 63

[162] V. V. Khromov, A. E. Logunov, A. S. Pazgalev, S. G. Przhibel'skii, D. Sarkisyan, and T. A. Vartanyan. Spectroscopy of the atom-wall interactions in a nanocell. *J. Phys. Conf. Ser.*, 397:012063, Dec 2012. 64, 107

[163] D. R. Häupl, D. Weller, R. Löw, and N. Y. Joly. Spatially resolved spectroscopy of alkali metal vapour diffusing inside hollow-core photonic crystal fibres, May 2022. 64

[164] C. Carr, C. S. Adams, and K. J. Weatherill. Polarization spectroscopy of an excited state transition. *Opt. Lett.*, 37(1):118–120, Jan 2012. 65, 128

[165] A. K. Mohapatra, T. R. Jackson, and C. S. Adams. Coherent optical detection of highly excited Rydberg states using electromagnetically induced transparency. *Phys. Rev. Lett.*, 98:113003, Mar 2007. 68

[166] S. Briaudeau, D. Bloch, and M. Ducloy. Sub-Doppler spectroscopy in a thin film of resonant vapor. *Phys. Rev. A - At. Mol. Opt. Phys.*, 59(5):3723–3735, May 1999. 70

[167] I. G. Hughes and T. P. A. Hase. *Measurements and their uncertainties: a practical guide to modern error analysis.* Oxford University Press, 2010. 71, 88, 91

[168] P. Todorov and D. Bloch. Testing the limits of the Maxwell distribution of velocities for atoms flying nearly parallel to the walls of a thin cell. *J. Chem. Phys.*, 147(19):194202, Nov 2017. 75

[169] B. Huber, T. Baluktsian, M. Schlagmüller, A. Kölle, H. Kübler, R. Löw, and T. Pfau. GHz Rabi flopping to Rydberg states in hot atomic vapor cells. *Phys. Rev. Lett.*, 107:243001, Dec 2011. 76

[170] S. Haroche, J. A. Paisner, and A. L. Schawlow. Hyperfine quantum beats observed in Cs vapor under pulsed dye laser excitation. *Phys. Rev. Lett.*, 30:948–951, May 1973. 76

[171] C. G. Wade, N. Šibalić, J. Keaveney, C. S. Adams, and K. J. Weatherill. Probing an excited-state atomic transition using hyperfine quantum-beat spectroscopy. *Phys. Rev. A*, 90:033424, Sep 2014. 76

[172] M. Knudsen. *The Cosine Law in the Kinetic Theory of Gases*. NASA technical translation. National Aeronautics and Space Administration, 1967. 78

[173] I. G. Hughes. Velocity selection in a doppler-broadened ensemble of atoms interacting with a monochromatic laser beam. *J. Mod. Opt.*, 65(5-6):640–647, Feb 2018. 86

[174] R. Loudon. *The Quantum Theory of Light*. Clarendon Press, Oxford, second edition, 1983. 98

[175] J. Mika, L. Podhora, L. Lachman, P. Obšil, J. Hloušek, M. Ježek, R. Filip, and L. Slodička. Generation of ideal thermal light in warm atomic vapor. *New J. Phys.*, 20(9):093002, Sep 2018. 98

[176] A. Dussaux, T. Passerat de Silans, W. Guerin, O. Alibart, S. Tanzilli, F. Vakili, and R. Kaiser. Temporal intensity correlation of light scattered by a hot atomic vapor. *Phys. Rev. A*, 93:043826, Apr 2016. 98

[177] R. Hanbury Brown and R. Q. Twiss. A test of a new type of stellar interferometer on Sirius. *Nature*, 178:1046–1048, Nov 1956. 99

[178] L. Stern, B. Desiatov, I. Goykhman, and U. Levy. Nanoscale light-matter interactions in atomic cladding waveguides. *Nat. Commun.*, 4(1):1548, Jun 2013. 119

[179] L. Stern, R. Zektzer, N. Mazurski, and U. Levy. Enhanced light-vapor interactions and all optical switching in a chip scale micro-ring resonator coupled with atomic vapor. *Laser Photon. Rev.*, 10(6):1016–1022, Nov 2016. 119

[180] R. Ritter, N. Gruhler, W. H. P. Pernice, H. Kübler, T. Pfau, and R. Löw. Coupling thermal atomic vapor to an integrated ring resonator. *New J. Phys.*, 18(10):103031, Oct 2016. 119

[181] R. Ritter, N. Gruhler, H. Dobbertin, H. Kübler, S. Scheel, W. Pernice, T. Pfau, and R. Löw. Coupling thermal atomic vapor to slot waveguides. *Phys. Rev. X*, 8:021032, May 2018. 119

[182] L. Midolo, A. Schliesser, and A. Fiore. Nano-opto-electro-mechanical systems. *Nat. Nanotechnol.*, 13(1):11–18, Jan 2018. 119

[183] K. W. Martin, G. Phelps, N. D. Lemke, M. S. Bigelow, B. Stuhl, M. Wojcik, M. Holt, I. Coddington, M. W. Bishop, and J. H. Burke. Compact optical atomic clock based on a two-photon transition in rubidium. *Phys. Rev. Applied*, 9:014019, Jan 2018. 122

[184] D. J. Whiting, R. S. Mathew, J. Keaveney, C. S. Adams, and I. G. Hughes. Four-wave mixing in a non-degenerate four-level diamond configuration in the hyperfine Paschen-Back regime. *J. Mod. Opt.*, 65(5-6):713–722, Mar 2018. 122

[185] J. Park, T. Jeong, and H. S. Moon. Temporal intensity correlation of bunched light from a warm atomic vapor with a ladder-type two-photon transition. *Sci. Rep.*, 8:10981, Jul 2018. 123

[186] C. P. Pearman, C. S. Adams, S. G. Cox, P. F. Griffin, D. A. Smith, and I. G. Hughes. Polarization spectroscopy of a closed atomic transition: applications to laser frequency locking. *J. Phys. B: At. Mol. Opt. Phys.*, 35(24):5141–5151, Dec 2002. 125, 127

[187] M. L. Harris, C. S. Adams, S. L. Cornish, I. C. McLeod, E. Tarleton, and I. G. Hughes. Polarization spectroscopy in rubidium and cesium. *Phys. Rev. A*, 73:062509, Jun 2006. 125